NTNU

Norwegian University of
Science and Technology

Ionic liquids as thermoelectric converter materials

Didrik Lindberg Roest

Chemical Engineering and Biotechnology
Submission date: July 2016
Supervisor: Signe Kjelstrup, IKJ
Co-supervisor: Vincenzo Barone, Scuola Normale Superiore di Pisa
Pietro Ballone, IFY

Norwegian University of Science and Technology
Department of Chemistry

Acknowledgements

I would like to thank my main supervisor Professor Signe Kjelstrup, for many important and helpful discussions. I would also like to thank my co-supervisor Professor Pietro Ballone, for all his help in my thesis as well as help with every question I have asked.

A thank is also in its place to Dr. Thuat T. Trinh, for all the help I have gotten from him regarding molecular dynamics in LAMMPS.

As this thesis concludes a five year study at NTNU, I would like to thank all the lecturers and professors I have met throughout the years, for all that they have taught me that books alone cannot.

Last, but not least, I want to thank my friends and family, who never stopped believing in me.

Summary

The interplay of heat flow and electrification phenomena at solid/fluid interfaces gives origin to intriguing effects such as Peltier's and Seebeck's, which is of great interest for applications such as production of electricity from waste heat, and represents a source of fascinating problems in statistical mechanics of non-equilibrium systems.

My Master thesis is devoted to the computational investigation by molecular dynamic (MD) simulation of the Seebeck effect, consisting in the creation of an electrostatic potential difference between two electrodes kept at different temperature and immersed into a conducting (electrolyte solution or molten salt) fluid.

Preliminary results of simulations based on idealised models show that MD is (barely) able to capture the essential feature of this effect, and thus provides a microscopic view of this phenomenon that could ease its understanding. More realistic models are being developed and tested aiming at the investigation of the Seebeck effect in organic conducting compounds that are fluid at relatively low temperature.

Two different models for ionic liquids have been investigated in this thesis. The first model consist of rigid ion particles, generalised to fit a variety of systems. The dependence of temperature, size- and charge-assymetry on the interfacial dipole were investigated. The second model was designed to be more realistic, and focuses on alkali carbonates.

In this report we present computations of transport properties for the alkali carbonates Li_2CO_3, Na_2CO_3 and K_2CO_3 at temperatures between 1200 K and 1500 K. This includes thermal and electrical conductivity, in addition to the diffusion coefficient for cations and anions. For these same compounds in between planar walls, an investigation of the interfacial dipole were carried out. The results provide important information to interpret data acquired in real life experiments.

Sammendrag

Samspillet mellom varmestrøm og elektrifiseringsfenomener ved faststoff/fluid grensesnitt gir opphav til spennende effekter som Peltiers og Seebecks, som er av stor interesse for ulike bruksområder slik som produksjon av elektrisitet fra spillvarme, og gir opphav til fascinerende problemer i statistisk mekanikk for systemer ut av likevekt.

Min masteroppgave er viet til datasimuleringer med molekylærdynamikk (MD) av Seebeck effekten, som består av dannelsen av en elektrostatisk potensialforskjell mellom to elektroder holdt ved forskjellige temperaturer og nedsenket i et ledende (elektrolyttløsning eller smeltet salt) fluid.

Foreløpige resultater fra simuleringene basert på idealiserte modeller viser at MD er (så vidt) i stand til å fange de essensielle trekkene av denne effekten, og derfor gir et mikroskopisk syn på dette fenomenet som kan gjøre det lettere å forstå. Mer realistiske modeller er under utvikling og testes med mål om å undersøke Seebeck effekten i elektrisk ledende organiske forbindelser som er fluider ved relativt lave temperaturer.

To forskjellige modeller for ioniske væsker har blitt undersøkt i denne avhandlingen. Den første modellen består av harde ionepartikler, generalisert til å passe en mengde ulike systemer. Avhengigheten av temperatur, størrelse- og ladningsasymmetri på grensesnittsdipolen ble undersøkt. Den andre modellen var designet for å være mer realistisk, og fokuserer på alkalikarbonater.

I denne rapporten presenterer vi beregninger av transportegenskaper for alkalikarbonatene Li_2CO_3, Na_2CO_3 og K_2CO_3 ved temperaturer mellom 1200 K og 1500 K. Dette inkluderer termisk og elektrisk konduktivitet, i tillegg til diffusjonskoeffisienten for kationer og anioner. For de samme forbindelsene mellom plane vegger ble det utført en granskning av grensesnittsdipolen. Resultatene gir viktig informasjon for å tolke data anskaffet i virkelige eksperimenter.

List of symbols

Notation	Description
D	Interfacial dipole
D_x	Total dipole
E	Electric field
f_i	Forces derived from the potential energy
f_{SR}	Switch function
k_B	Boltzmann's constant
l_x	Separation between the walls
L_α	Periodicity in α-direction
m	Mass
N_i	Number of particles of type i
R_{ij}	Distance between particle i and j
$\mathbf{R}_i$	Position vector for particle i
t	Time
t_a	Autocorrelation time
t_1	Average temperature of neutral particles in the left wall
t_2	Average temperature of neutral particles in the right wall
T	Target temperature
T_0	Temperature of both walls
T_l, T_1	Target temperature of left wall
T_r, T_2	Target temperature of right wall
U	Lennard-Jones interaction potential
v_{ij}	Interaction between particle i and j
w_l	Parabolic potential of left wall
w_r	Parabolic potential of right wall
x, y, z	Cartesian coordinate
X_l	Limit for left wall potential
X_r	Limit for right wall potential
Z_i	Charge of particles of type i
β_i	Random forces
δ	Dirac delta function
δQ	Net charge
η	Friction coefficient
ρ	Density
$\rho \times \sigma_{++}^3$	Dimensionless density
ρ_{tot}	Total number density
ρ_Q	Charge density
σ_{ij}	Collision diameter between particle i and j
ϕ	Electrostatic potential

Notation	Description	Unit
A	Cross-sectional area	[Å^2]
b	Weight of the Born-Mayer-Huggins interaction	[kcal/mol]
d	Dimensionality of the system	
D	Interfacial dipole	[D/nm^2]
D_i	Diffusion coefficient of specie i	[cm^2/s]
E	Electric field	[V/Å]
F	Faraday's constant	[C/mol]
$\mathbf{F}_{spring}$	Force from the spring	[kcal mol^{-1} Å^{-1}]
g_{ij}	Radial distribution function between atom i and j	
$\mathbf{J}_q$	Heat flux	[J s^{-1} m^{-2}]
$\mathbf{j}$	Electric current density	[C s^{-1} m^{-2}]
k	Wavenumber	[Å^{-1}]
k_B	Boltzmann's constant	[kcal mol^{-1} K^{-1}]
k_e	Coulomb's constant	[V Å e^{-1}]
K_r	Force field constant for bond stretching	[kcal mol^{-1} Å^{-2}]
K_{spring}	Spring constant	[kcal mol^{-1} Å^{-2}]
K_θ	Force field constant for angle bending	[kcal mol^{-1} rad^{-2}]
K_ϕ	Force field constant for improper torsion	[kcal mol^{-1} rad^{-2}]
L_α	Length of simulation box/periodicity in α-direction	[Å]
M_w	Molar mass	[g/mol]
n_i	Number of electrons in the outer shell of atom i	
n_{ij}	Coordination number between atoms of type i and j	
N_i	Number of atoms of type i	
P	Pressure	[kbar]
r	Radius	[Å]
r_{ij}	Distance between atom i and j	[Å]
r_0	Equilibrium distance in the stretching potential	[Å]
$\mathbf{r}$	Position vector in mean square displacement	[Å]
$\mathbf{r}_d$	Diplacement vector	[Å]
R	Universal gas constant	[J K^{-1} mol^{-1}]
S_{NN}	Number-number structure factor	
S_{ZZ}	Charge-charge structure factor	
t	Time	[fs]
T	Temperature	[K]
T_m	Melting point	[K]
T_b	Boiling point	[K]
U_{pot}	Born-Oppenheimer potential energy surface	

Notation	Description	
v	Velocity	[m/s]
V	Volume	[Å^3]
$V_{bending}$	Potential energy due to angle bending	[kcal/mol]
V_{BMH}	Born-Mayer-Huggins potential	[kcal/mol]
V_{LJ}	Lennard-Jones potential	[kcal/mol]
$V_{improper}$	Potential energy due to improper torsion	[kcal/mol]
$V_{stretching}$	Potential energy due to bond stretching	[kcal/mol]
z_i	Valence of atom i	[e]
α	Steepness of Born-Mayer-Huggins interaction	[Å^{-1}]
ϵ	Depth of the potential well in the Lennard-Jones potential	[kcal/mol]
ϵ_0	Vacuum permittivity	[e Å^{-1} V^{-1}]
λ	Thermal conductivity	[W m^{-1} K^{-1}]
κ	Electrical conductivity	[S/cm]
κ_{NE}	Electrical conductivity from the Nernst-Einstein relation	[S/cm]
κ'_{NE}	Modified Nernst-Einstein electrical conductivity	[S/cm]
ρ	Density	[g/cm^3]
ρ_i	Number density of specie i	[Å^{-3}]
ρ_Q	Charge density	[e/Å^3]
ν_+	Number of cations per formula unit of electrolyte	
ν_-	Number of anions per formula unit of electrolyte	
ν_i	Vibrational frequency of mode i	[cm^{-1}]
σ_i	Ionic radius of atom i	[Å]
σ_w	Surface charge density of the wall	[e/Å^2]
$\phi(z)$	Electrostatic potential in z-direction	[V]
ϕ	Improper torsion angle	[°]
ϕ_0	Equilibrium improper torsion angle	[°]
θ	Bending angle	[°]
θ_0	Equilibrium bending angle	[°]
χ_T	Isothermal compressibility	

Subscripts

Notation	Description
Coul, Hartree	Coulombic
$+$, 1	Cations
$-$, 2	Anions
n	Neutral particles
i, j	Atom type
Li	Lithium
Na	Sodium
K	Potassium
O	Oxygen
C	Carbon
CO_3	Carbonate
Q, Z	Charge
w	Wall
w, i	Wall, inside
w, o	Wall, outside
x, y, z	Cartesian coordinate
ν, μ	Component

Contents

Chapter 1

Introduction

1.1 History

Thermoelectricity was first discovered by Alessandro Volta around 1794-1795 [1, 2] while frying a frog [3]. A sketch of his experiment can be seen in Figure 1.1, which is taken from Ref. [1].

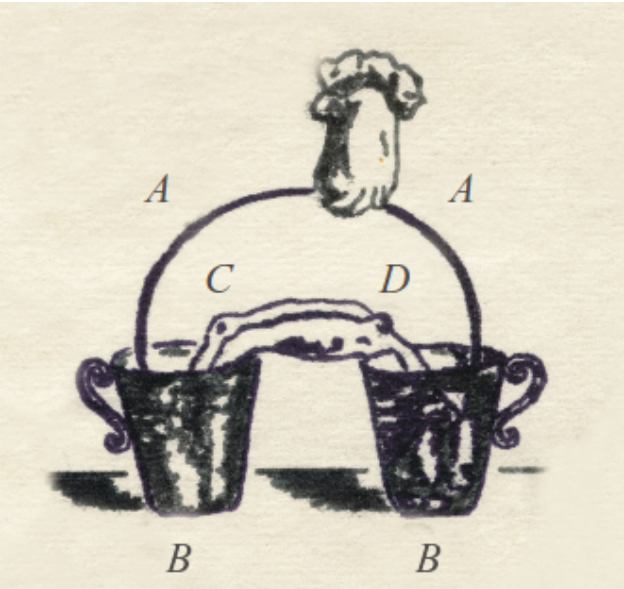

Figure 1.1: Sketch of Volta's experiment. A metal wire (A) is submerged in glasses of water (B), in which the hind legs is placed in one (C) and the back/spine in the other (D). The figure is taken from Ref. [1].

Volta observed in his experiment that if he heated one end of the iron wire before putting it into the water, the frog would convulse, giving reason to believe a current is passing through. This happened many years before the experiments by Seebeck in 1821. It is

therefore a science that is over 200 year old, but our knowledge about it is still lacking.

1.2 Motivation and outline of the thesis

The direct conversion of heat into electric power is a subject of obvious interest, but is poorly understood. It might become practically and economically relevant if we could tap into the vast amount of waste heat released by industrial processes at temperatures below around 200 °C, where power production from steam is unlikely. A promising way to implement the direct conversion of heat into electric power is through the Seebeck effect, that corresponds to the generation of an electrostatic potential drop whenever a conductor is subjected to a temperature gradient.

To achieve this goal requires the development of new materials, able to turn temperature differences into an electrostatic potential difference, at a rate and efficiency sufficient to make the process competitive with other means to produce electric power. The most common materials used so far are semiconductors, having small energy conversion efficiencies.

Thermodynamic and statistical mechanics considerations show that the most important quantity underlying the Seebeck effect is entropy, and transported entropy in particular [4]. Any theoretical analysis, therefore has to cover this crucial aspect, making computer simulation particularly suitable for the task.

The idea of this thesis is to explore the potential of a new class of materials in this context, namely ionic liquids, and room temperature ionic liquids in particular [5, 6]. Like their counterparts, semiconductors, they are equally well conducting, and can be used at relatively low temperatures, but they have larger Seebeck coefficients. But the origin of their Seebeck coefficient, more particularly the transported entropy of the ions is poorly understood.

The development stage could be cut and optimised, provided we understand the many microscopic mechanisms that underlie this complex energy transformation. This thesis is

devoted to the investigation of an important portion of these microscopic aspects, namely the role of the electrolyte in the generation of an electrostatic potential energy difference between two electrodes kept at different temperature (Seebeck effect).

The systems were studied using molecular dynamics simulations, which were divided into two main stages. In the first stage (chapter 3), the system was made of rigid ion particles interacting with isotropic pair potentials confined between walls made of neutral particles. The system as a whole is electroneutral. In this stage two distinct series of simulations were done. The first series consisted of equilibrium simulations covering a wide temperature range. The second series consisted of stationary but non-equilibrium conditions with a thermal gradient across the fluid phase.

In both simulations series, the surface dipole were enhanced by looking at asymmetric ions, asymmetric wall-particle interactions and different valence of cations and anions.

In the second stage (chapter 4) the model is made more realistic by using a parametrised force field for alkali carbonates, considering both homogeneous and inhomogeneous systems made of a liquid confined in between neutral walls that represents electrodes.

Results from the microscopic simulations can later be interpreted in terms of thermodynamic functions , and possibly analysed by the Small System Method (SSM) [7], in which fluctuations from small systems and appropriate scaling can be used to find the values at the thermodynamic limit [8].

This will set a basis for extensions which studies more complex ions, both flexible and polarisable, in order to be able to compare with experimental results obtained by Dr. M. T. Børset in the group of non-equilibrium thermodynamics at NTNU.

1.3 Background

Thermoelectric energy converters are already considered for use in cars, see review of Zebarjadi et al. [9] or in the Norwegian silicon industry [10]. Consider the simple converter in Figure 1.2 made by n- and p-type semiconductors. The unit is kept between a heat source at temperature T_H and a heat sink at temperature T_L, and produces an electric potential difference, $\Delta\phi$, proportional to the temperature difference

$$\Delta\phi = \alpha_S(T_H - T_L) - R_\Omega j \tag{1.3.1}$$

The last term in this equation is the ohmic potential drop, where R_Ω is the electric resistance and j is the electric current density. The electric resistance is related the electrical conductivity κ as $R_\Omega = 1/\kappa$. The Seebeck coefficient, α_S, gives the thermoelectric potential and the maximum power output

$$P_{max} = (\Delta\phi)j = \frac{\alpha_S(T_H - T_L)^2\kappa}{4} \tag{1.3.2}$$

The power variation is illustrated in Figure 1.2. The efficiency of the converter is often expressed in terms of the figure of merit

$$ZT = \frac{\kappa(\alpha_S)^2 T}{\lambda} \tag{1.3.3}$$

where λ is the thermal conductivity.

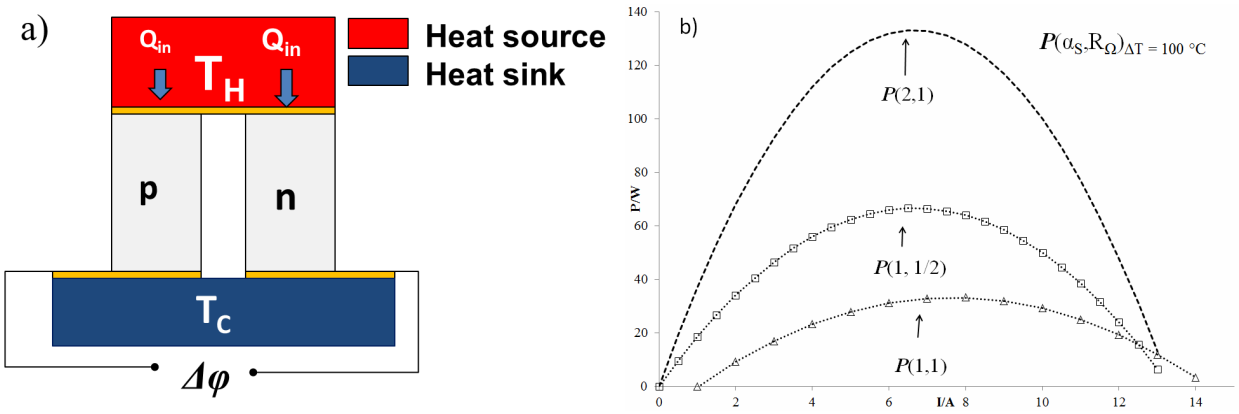

Figure 1.2: a) A connected pair of n- and p-type semiconductors in a basic unit of a common thermoelectric energy converter. An electric potential arises when the unit is placed between a heat source and a sink. b) The maximum power depend on Seebeck coefficient, α_S, and resistance, R_Ω.

In general, the coefficient α_S is a function of thermodynamic entropies as well as transported entropies in the system:

$$\alpha_S = \left(\frac{d\phi}{dT}\right)_{j=0} = f(S_i, S_i^*) \tag{1.3.4}$$

For semiconductors, α_S contains only the transported entropy of the n- and p-conductors. The exact relation (1.3.4) can be derived from non-equilibrium thermodynamics theory. Solid state semiconductor devices are attractive because they are maintenance-free, reliable, silent, dynamic and adaptable to a variety of temperature ranges. Their drawback is their low efficiency with values around 5 %. The Seebeck coefficients of these materials are typically in the order of a few hundred microvolts per Kelvin, e.g. around $240 \cdot 10^{-6}$ V/K for a BiTe-based device. The effort to increase the conversion efficiency of thermoelectric converters was recently reviewed [9].

The low efficiency of the thermoelectric devices based on semiconductors is the main reason for the investigation of new materials to be used in this context. As ionic liquids has much higher Seebeck coefficients, it is desirable to understand why this is the case and to find which factors are important in this matter.

Chapter 2

Theoretical and computational background

2.1 Basic definitions

2.1.1 Born-Oppenheimer approximation and potential energy surface

Condensed matter consists of atomic nuclei and electrons, forming atoms and molecules. This gives origin to a variety of structures and phases. The ratio between the electron and the nuclei masses is $m_e/m_H \sim 1/1800$ at most. At the conditions prevalent in our environment, that we characterise as being of moderate temperature and pressure, this low ratio implies that electrons relax to their ground state much faster than typical time scales of nuclear motion. As a result, the relevant dynamical variables are primarily the nuclear coordinates $\{\mathbf{R}_I, I = 1, ..., N\}$, while the electron ground state energy as a function of these coordinates provides the Born-Oppenheimer potential energy surface $U_{pot}[\{\mathbf{R}_I, I = 1, ..., N\}]$ that determines the atomic dynamics.

2.1.2 Pair potentials

The meaningful simulation of systems made of many atoms and molecules requires a good description of the interaction potential between the particles, as this will be used to calculate the forces acting between them. As a first approximation, we can assume that atoms interact

in pairs giving origin to the so-called pair potential approximation:

$$U_{pot}[\{\mathbf{R}_I, I = 1, ..., N\}] = \frac{1}{2}\sum_{i \neq j}^{N} V(|\mathbf{R}_I - \mathbf{R}_J|) \tag{2.1.1}$$

where it has been assumed that the function $V(r)$ is isotropic, and therefore depends only on the inter-atomic distance.

The most important feature of such a potential is the short-range repulsion, which originates from the overlap of outer electron shells. Such a potential should also include long-range attractive forces, which vary more smoothly with distance between the atoms and molecules and the short-range interaction.

A paradigmatic pair potential is the Lennard-Jones (LJ) 12-6 potential:

$$V_{LJ}(r) = 4\epsilon \left[\left(\frac{\sigma}{r}\right)^{12} - \left(\frac{\sigma}{r}\right)^{6} \right] \tag{2.1.2}$$

Where σ is the collision diameter and ϵ is the potential well depth. The r^{-12} term is the repulsive term, and describes Pauli repulsion at short range. The r^{-6} term is the long-range attraction, which models the van der Waals or dispersion force. Another important interaction is represented by Coulomb forces, whose corresponding potential energy is:

$$U_{Hartree} = \frac{1}{2}\sum_{i \neq j} k_e \frac{q_i q_j}{r_{ij}} \tag{2.1.3}$$

In compounds bound by covalent bonds, and in most covalent molecules in particular, atoms interact with each other through directional forces. In such a case, we attribute a conventional energy E_0 to the ground state structure of each molecule, and approximate the energy change in deforming the molecular geometry as the sum of the energy required to stretch, bend and twist bonds:

$$V_{covalent} = V_{stretching} + V_{bending} + V_{improper} \tag{2.1.4}$$

More details will be given in the following chapters.

2.1.3 Radial distribution functions

The radial distribution function (RDF), $g(r)$, gives valuable information about the local structure of a fluid, for example how packed the system is. It gives the conditional probability of finding an atom a distance r away from another atom compared to the ideal gas distribution [11]. Therefore, $g(r)$ is dimensionless, and, for homogeneous liquid samples should reach unity for larger values of r.

From the RDF, the running coordination numbers n_{ij} can be found, see e.g. [12]. The coordination number of interest is usually found from the first coordination shell. This gives information about how many atoms of type j surrounds each atom of type i on average. Coordination numbers often suggests the type of (approximate) symmetry for the local coordination of atoms. More detail on this in section 4.2.4.

2.1.4 Structure factor

While the radial distribution functions are the usual simulation output concerning structure, comparison with experiments requires the computation of structure factors, since this is what is given from X-ray and neutron scattering experiments.

In a multicomponent system made of n species, we defined $n(n-1)/2$ partial structure functions, each computed as

$$S_{\mu\nu}(k) = \frac{1}{N}\langle\widetilde{\rho^*_\mu}(k)\widetilde{\rho_\nu}(k)\rangle \tag{2.1.5}$$

where $\widetilde{\rho_\alpha}(k) = \sum_{i\in\alpha} e^{i\mathbf{R}_i\mathbf{k}}$. $\mathbf{R}_i$ are the ion coordinates.

Partial structure factors, however, are not very informative when there are more than two components. The structural information usually is coded into a number-number structure factor:

$$S_{NN}(k) = \sum_\nu \sum_\mu S_{\nu\mu}(k) \tag{2.1.6}$$

and into a charge-charge structure factor:

$$S_{ZZ}(k) = \sum_{\nu} \sum_{\mu} z_\nu z_\mu S_{\nu\mu}(k) \tag{2.1.7}$$

The first function ($S_{NN}(k)$) describes the correlations in the fluctuations of the ion density irrespective of the ion type. The second function ($S_{ZZ}(k)$) instead describes correlations in the charge fluctuations.

2.2 Ionic liquids

The theory of ionic liquids is gathered from the book by Hansen and McDonald [13].

Ionic liquids, i.e. a liquid where the particles carry an electric charge, have several features which is not found in fluids of neutral particles. Many of these properties are due to the longe-range Coulomb interactions.

A tendency towards electrical charge neutrality is an crucial feature. Not only can this be seen at a macroscopic level, but it is important at the microscopic level as well in terms of screening. If an external charge is introduced into an ionic liquid, it will cause a rearrangement, or polarisation, of the surrounding charge density. This will be done in such a way that electrostatic potential due to the external charge decays much faster than the Coulomb potential. Any ion in the fluid an be regarded as having an external charge, which makes this such an important feature. Due to the competition between packing and screening, a charge ordering of the ions occur at high density. Molten salts are examples of ionic liquids at high density and with high correlation.

The long-range Coulomb interaction heavily influences the static properties of ionic liquids. A thorough description of long-range correlations in molecular fluids can be seen in Ref. [14]

The simplest class of ionic liquids is molten salts, which is also the main focus of this thesis. Molten salts are characterised by having large cohesive energies. Due to the relatively high melting point, molten salts are usually associated with high temperatures. The

electrical conductivities of such liquids are usually in the order of 1 S/cm.

Historically, Coulombic fluids are some of the first liquids to be studied by simulation. Moreover, the hypernetted-chain equation [13] acts as a good approximation for these kind of liquids.

The total potential for a idealised ionic liquid can be written as:

$$V_N(\mathbf{r}^N) = V_N^S(\mathbf{r}^N) + V_N^C(\mathbf{r}^N) = \sum_{i=1}^{N}\sum_{j>i}^{N} A_{ij}\exp\left(r_{ij}/\rho_{ij}\right) + \frac{z_i z_j e^2}{\epsilon|\mathbf{r}_j - \mathbf{r}_i|} \tag{2.2.1}$$

The first term is the pair potential by Tosi and Fumi, and the second term is the Coulomb interaction.

The Coulomb term is often replaced with the Fourier transform of it. Because of its simple analytical form, the Coulomb energy is easily computed also in reciprocal space. The charge density in Fourier space can be represented as:

$$\rho_{\mathbf{k}}^Z = \sum_{\nu} z_\nu \rho_{\mathbf{k}}^\nu \tag{2.2.2}$$

which is a complex function.

The Fourier transform of the Coulomb potential between two elementary charges is given as

$$\hat{v}(k) = 4\pi\frac{e^2}{k^2} \tag{2.2.3}$$

The limit $k \to 0$ gives an important characteristic of Coulomb systems, namely the k^{-2} singularity. The Coulomb energy is given as:

$$U_{Hartree} = \sum_{\mathbf{k}} 4\pi e^2 \frac{\rho_{\mathbf{k}}\rho_{\mathbf{k}}^*}{k^2} \tag{2.2.4}$$

2.2.1 Electrical double layer

In an ionic liquid, a layering of the ions occur if a planar electrode is introduced. The ions with the opposite charge of the electrode will be closest to the electrode, followed by a layer of ions with a charge of same sign as the electrode. This constitutes an electrical double layer. The reason why this layering does not continue is because of the tendency for the ions to spread out in the bulk, in order to maximise the entropy. This layering can also be seen if the the electrode is replaced with a neutral wall, if the ions are of different size. Then the smaller ions (typically cations) will be closest to the wall, while the outer layer will consist of the larger ions (typically anions).

2.3 Molecular dynamics

The following theory is gathered from Hansen and McDonald [13]. In a system with N particles, the dynamical state is described by $3N$ coordinates $\mathbf{r}$ and $3N$ momenta $\mathbf{p}$. These $6N$ variables defines a *phase point* in a $6N$-dimensional *phase space*. Properties like pressure and internal energy can be written as averages of functions of $\mathbf{r}$ and $\mathbf{p}$ of the particles. These properties should be independent of time when equilibrium is achieved, but they will fluctuate around a mean value. Given the coordinates and momenta of the particles at one instance of time, their values at subsequent times can be found by the method of Molecular Dynamics.

In a Molecular Dynamics (MD) simulation, the idea is to try to mimic the movement of atoms and molecules by solving Newton's equation of motion $m\ddot{\mathbf{r}}_i = \mathbf{F}_i$, where m is the particle mass, $\ddot{\mathbf{r}}_i$ is the second time derivative of the atom coordinates and $\mathbf{F}_i$ is the force acting on particle i.

2.3.1 Periodic boundary conditions

Usually, it is the bulk properties of the system that is of interest, meaning we are not interested in surface effects. Therefore, it is usual to use periodic boundary conditions (PBC),

meaning that if a particle were to exit the simulation box on one side, it would reappear on the other side. This also has the benefit of requering less particles in the simulation in order to get good statistics, speeding up the simulation.

2.3.2 Velocity Verlet

In a molecular dynamics simulation, it is crucial that the equations of motion are integrated with a stable integrator. Otherwise, problems like energy drift can occur. An algorithm for a good integration scheme should be both time reversible and area preserving [15]. It should also be sufficiently efficient, as the equations of motions needs to be integrated millions of times in a simulation. The velocity Verlet integrator scheme is an example of such an algorithm, and will be used in this thesis.

This can be written as the combination of a predicator step:

$$\mathbf{r}_i(t+\Delta t) = \mathbf{r}_i(t) + \dot{\mathbf{r}}_i(t)\Delta t + \frac{1}{2}\ddot{\mathbf{r}}_i(t)\Delta t^2 \tag{2.3.1}$$

$$\dot{\mathbf{r}}_i(t+\Delta t) = \dot{\mathbf{r}}_i(t) + \ddot{\mathbf{r}}_i(t)\Delta t \tag{2.3.2}$$

followed by the computation of $\ddot{\mathbf{r}}_i(t+\Delta t)$ at position $\mathbf{r}_i(t+\Delta t)$, and by the corrector step

$$\dot{\mathbf{r}}_i(t+\Delta t) = \dot{\mathbf{r}}_i(t+\Delta t) + \frac{1}{2}\Delta t\left[\ddot{\mathbf{r}}_i(t+\Delta t) - \ddot{\mathbf{r}}_i(t)\right] \tag{2.3.3}$$

2.3.3 Ewald summation

Techniques for computing the Coulombic interactions of an extended, periodic system at a low cost are important in molecular dynamics, due to the long-range nature of such interactions. One such method is the Ewald summation.

Using Ewald sums, the Coulombic potential V_{Coul} can be written as [15]:

$$V_{Coul} = \frac{1}{2}\sum_{i\neq j}^{N}\frac{q_i q_j \mathrm{erfc}(r_{ij}\sqrt{\alpha})}{r_{ij}} + \frac{1}{2V}\sum_{\mathbf{k}\neq 0}\frac{4\pi}{k^2}|\rho(\mathbf{k})|^2 \exp\left(\frac{-k^2}{4\alpha}\right) - \sqrt{(\alpha/\pi)}\sum_{i=1}^{N} q_i^2 \tag{2.3.4}$$

where $\mathbf{k}$ are reciprocal lattice vectors, included up to a cufoff $k^2 \leq k^2_{cutoff}$. This equation contains both a part in real space and a part in Fourier space. The reason for this is because some terms converges fast in real space, while other terms converges fast in Fourier space.

Chapter 3

A simple, idealised model: Rigid ion particles

3.0 Introduction

Charge separation and the presence of sizeable electric fields in close proximity of interfaces are ubiquitous phenomena that greatly affect the stability and rheology of inhomogeneous systems [16]. Such electrification phenomena are particularly important at solid/liquid interfaces, since the charge separation is eased by the mobility of ions or by the reorientation of polar molecules. At thermal equilibrium, electrification phenomena at planar or nearly planar interfaces take the form of localised electrostatic double layers [17], leading to an electrostatic potential difference and interface capacitance, without long wavelength electric fields beyond a microscopic distance from the interface. This harmonious picture may be drastically perturbed under non-equilibrium conditions, even when restricted to time invariant stationary states [14].

Electrification phenomena and electrostatic double layers at solid/fluid interfaces have been and still are extensively investigated by experimental means, including cyclic voltammetry, a variety of spectroscopies, as well as recent near field approaches. The theoretical community took an early interest in these systems and phenomena, as documented in the seminal papers by Gouy [18] and Chapman [19], anticipating the Debye and Hückel theory for screening of individual ions in homogeneous electrolyte solutions [20]. The pioneering stage ended with the systematic analysis by integral equations and classical density functional theory [21].

Computer simulation has progressively taken over as the standard method to investigate electrified interfaces [22, 23]. Most of the simulations concerned low density systems, of interest for electrolyte solutions, often represented in the implicit solvent picture. Until recently, only a few studies concerned packing and coupling regimes typical of molten salts. This area of investigation is being revived by the current interest in room temperature ionic liquids [5], that bring strong coupling to the ambient conditions range. In the case of simple liquids, the results of simulation and integral equation theories agree fairly well. The comparison of results from either approaches with experimental data is far less clear, partly because crucial ingredients of real systems such as the atomistic structure of the solid side of the interface, or the polar or apolar solvent are neglected or severely approximated. Perhaps more importantly, almost without exceptions the computational and theoretical analysis concerns systems in thermal equilibrium. Both electrochemistry experiments, and especially applications concern primarily systems in stationary (i.e., time independent) but out of equilibrium conditions, in which energy and charge flow throughout the system.

All these studies concern systems at equilibrium.

As extensively discussed in Ref. [16], a separation of charge will take place at the solid/liquid interface whenever cations and anions are not perfectly equivalent, and/or whenever their interaction with the solid boundaries is not the same. Upon formation of the double layer, each interface is like a planar capacitor, and, apart a numerical factor 4π, the electrostatic potential drop at each interface is measured by the dipole per unit surface of the charge density distribution.

Let us assume that cations and anions are not symmetric, but interact in the same way with the left and right boundary. At equilibrium ($T_1 = T_2$), the potential drop on the right interface will cancel the potential drop at the left interface by symmetry. Any chemical difference between the two solid boundaries, or a different temperature at the two sides ($T_1 \neq T_2$) will break the specular symmetry in the simulation cell, giving origin to a net electrostatic potential drop across the simulation cell. If the asymmetry is due to a temperature imbalance, the electrostatic potential energy difference can be maintained even

is the two electrodes are joined by an electron conductor, provided the temperature difference is kept constant by thermal contact with two different reservoirs at temperatures T_1 and T_2.

Since the target parameter to be optimised is $\Delta\phi$ across the interface, the first approach could be to search for interfaces having a large surface dipole, with a strong dependence on temperature. As a side question, we could ask ourselves what is the largest surface dipole that could be sustained by a given fluid.

We address these questions by two distinct series of simulations, the first series considering stationary but non-equilibrium conditions with a thermal gradient across the fluid phase; the second series instead consists of equilibrium simulations covering a wide temperature range. In both series of simulations, we enhanced the surface dipole by considering: (i) asymmetric ions, with $1.2 \leq \sigma_{22}/\sigma_{11} \leq 2$; (ii) asymmetric wall particle interactions; (iii) different valence of cations and anions, with $1 \leq |Z_1/Z_2| \leq 3$.

Both series of simulations have been carried out for relatively small systems, but test computations have been performed on significantly larger samples.

A subtle question that we cannot overlook: under non-equilibrium conditions, the surface dipole cannot be the only source of $\Delta\phi$, there must be also a net surface charge, that in turn implies long-range correlations in the system.

To enhance our understanding of electrostatic double layers, we carry out computer simulations for rigid ion model fluids confined between planar surfaces. We explore in particular the effect of size and charge asymmetry. The investigation of the temperature dependence of the electrostatic potential drop at each interface suggests a simple model for the Seebeck coefficient of electrolyte/electrode interfaces.

Following the standard practice in computations and in theory (as opposed to experiments), in presenting my results I will introduce dimensionless quantities, dividing the quantities that is computed by a natural scale of the same physical dimensions. This will make the results suitable to fit a wide variety of different systems. The conversion to standard units can be carried out afterwards, multiplying each quantity again by a scale of the same

dimensionality, this time measured in fixed units.

3.1 Models and methods

We investigate systems made of neutral and rigid ion particles, interacting with pair potentials. Each simulation sample, in particular, consists of a number of cations N_+ of charge Z_+, a number of anions N_- of charge Z_-, and a number of neutral particles N_n confined in between two planar walls perpendicular to the x direction. Their mutual interaction v_{ij} is given by:

$$v_{ij}(\mid \mathbf{R}_i - \mathbf{R}_j \mid) = \frac{Z_i Z_j}{\mid \mathbf{R}_i - \mathbf{R}_j \mid} + \left(\frac{\sigma_{ij}}{\mid \mathbf{R}_i - \mathbf{R}_j \mid} \right)^{12} f_{SR}(\mid \mathbf{R}_i - \mathbf{R}_j \mid) \tag{3.1.1}$$

where $R_{ij} = \mid \mathbf{R}_i - \mathbf{R}_j \mid$ is the distance between particle i and j, σ_{ij} is the collision diameter between particle i and j and $f_{SR}(R)$ is a switch function that over the $R_c \leq R \leq R_c + \Delta$ smoothly extinguishes the inverse power potential together with its first derivative:

$$f_{SR}(R) = \begin{cases} 1 & R \leq R_c \\ \cos\left[\pi \frac{(R-R_c)}{\Delta}\right] & R_c \leq R \leq R_c + \Delta \\ 0 & R \geq R_c + \Delta \end{cases} \tag{3.1.2}$$

where R_c is a distance that depends on the species of particles i, j and Δ is a parameter that decides the length of the smoothing.

The confining walls are represented by parabolic potentials, w, given, on the right, by:

$$w_r(x) = \begin{cases} 0 & x \leq X_r \\ \frac{1}{2}(x - X_r)^2 & x > X_r \end{cases} \tag{3.1.3}$$

and on the left:

$$w_l(x) = \begin{cases} \frac{1}{2}(X_l - x)^2 & x < X_l \\ 0 & x \geq X_l \end{cases} \tag{3.1.4}$$

where X_r, X_l are limits to how far the potential last in the x-direction for the right and left wall, respectively. The system is periodic along the y and z directions, with periodicity L_y and L_z, respectively. To account for Coulomb forces by the $3D$ version of the Ewald method, we make our system periodic also along the x direction, with a periodicity L_z longer than the separation ΔX of the confining potentials.

Neutral particles that are used to make a wall for the system are included primarily to thermalise the ions at temperature T_l, T_r in proximity of the left and right confining walls, respectively. To this aim, part (or the whole) of the neutral population is confined by a one body potential, linking particles to fixed positions on a regular lattice. Moreover, all particles follow Newton's equations of motion, while neutral particles evolve according to Langevin dynamics:

$$m\ddot{\mathbf{R}}_i = \mathbf{f}_i \tag{3.1.5}$$

$$m\ddot{\mathbf{R}}_i = \mathbf{f}_i - \eta\dot{\mathbf{R}}_i + \beta_i(t) \tag{3.1.6}$$

where the dots represents time derivatives, f_i are the forces derived from the potential energy, η is the friction coefficient, while β_i are random forces, satisfying the relations:

$$\langle\beta_i(t)\rangle = 0 \tag{3.1.7}$$

$$\langle\beta_i(t)\cdot\beta_j(t')\rangle = 6\eta k_B T\delta_{i,j}\delta(t-t') \tag{3.1.8}$$

In these last relations, k_B is the Boltzmann constant, δ is the Dirac delta function and T is the target temperature of the simulation. In our code, we faithfully implemented Eq. (18), and Eq. (21) to Eq. (23) of Ref. [24], slightly modifying the velocity Verlet algorithm used in the $\eta = 0$ case. The equations from the reference is also given here:

$$r^{n+1} = r^n + bdtv^n + \frac{bdt^2}{2m}f^n + \frac{bdt}{2m}\beta^{n+1} \tag{3.1.9}$$

$$v^{n+1} = av^n + \frac{dt}{2m}(af^n + f^{n+1}) + \frac{b}{m}\beta^{n+1} \tag{3.1.10}$$

with a and b defined as

$$a = \frac{1 - \frac{\eta dt}{2m}}{1 + \frac{\eta dt}{2m}} \tag{3.1.11}$$

$$b = \frac{1}{1 + \frac{\eta dt}{2m}} \tag{3.1.12}$$

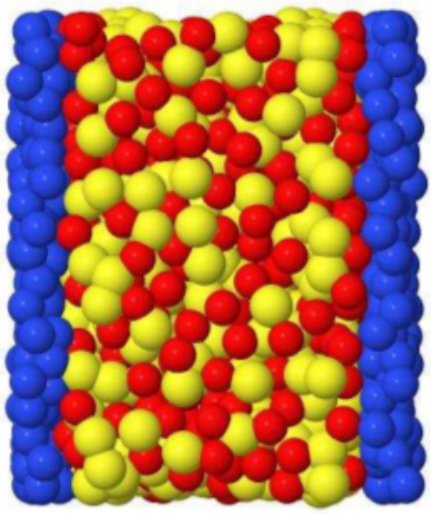

Figure 3.1: Simulation snapshot of system consisting of 600 cations (red particles) and 600 anions (yellow particles) of charge ± 1, confined by soft walls (not shown) and in contact with two thin layers of neutral particles (dark blue particles) providing thermal contact with reservoirs at T_l, T_r.

Table 3.1: List of systems extensively simulated in the present study. Limited computations have been carried out also for other systems. In all cases, $\sigma_{++} = 1$, the number of neutral particle in the system (two walls) is $N_n = 468$, $\sigma_{nn} = 1.2$, the separation of the two walls (see text) is $l_x = 13.732$, while the periodicity of the simulation box is $L_x \times L_y \times L_z = 19.617 \times 15.600 \times 18.706$. The number of MD steps refers to the non-equilibrium simulations discussed in the text.

Sample #	σ_{+-}	σ_{--}	σ_{+n}	σ_{-n}	MD steps/10^6
$Z_+ = 1 \quad Z_- = -1 \quad N_+ = N_- = 600$					
1	1.1	1.2	1.5	1.5	39
2	1.2	1.4	1.5	1.5	45
3	1.3	1.6	1.5	1.5	45
4	1.4	1.8	1.5	1.5	45
5	1.5	2.0	1.5	1.5	48
6	1.3	1.6	1.4	1.6	30
7	1.3	1.6	1.45	1.55	30
8	1.3	1.6	1.55	1.45	30
9	1.3	1.6	1.6	1.4	30
$Z_+ = 2 \quad Z_- = -1 \quad N_+ = 400 \quad N_- = 800$					
10	1.1	1.2	1.5	1.5	30
$Z_+ = 3 \quad Z_- = -1 \quad N_+ = 300 \quad N_- = 900$					
11	1.1	1.2	1.5	1.5	30
$Z_+ = 1.4 \quad Z_- = -1 \quad N_+ = 500 \quad N_- = 700$					
12	1.1	1.2	1.5	1.5	30
$Z_+ = 1.5 \quad Z_- = -1 \quad N_+ = 480 \quad N_- = 720$					
13	1.1	1.2	1.5	1.5	30

3.2 Results and discussion

3.2.1 Equilibrium simulation results

Equilibrium molecular dynamics simulations have been carried out for the systems listed in Table 3.1. This stage of simulations has been performed in the canonical (NVT) ensemble upon disconnecting the system from the Langevin thermostats after equilibration at the target temperature. The micro-canonical ensemble (NVE) was used in the production run after equilibration. In all cases, the runs to obtain equilibrium exceeded 3×10^3 time units to ensure that equilibrium was reached, while production simulations covered at least 18×10^3 time units. The determination of the mean square displacement of cation and anions as a function of time, as well as visual analysis of simulation snapshots show that our samples are liquid-like at all temperatures $0.8 \leq T \leq 3.0$.

A representative example of the dimensionless density profile $\rho(x) \times \sigma_{++}^3$ of cations, anions and neutral particles is shown in Figure 3.2.

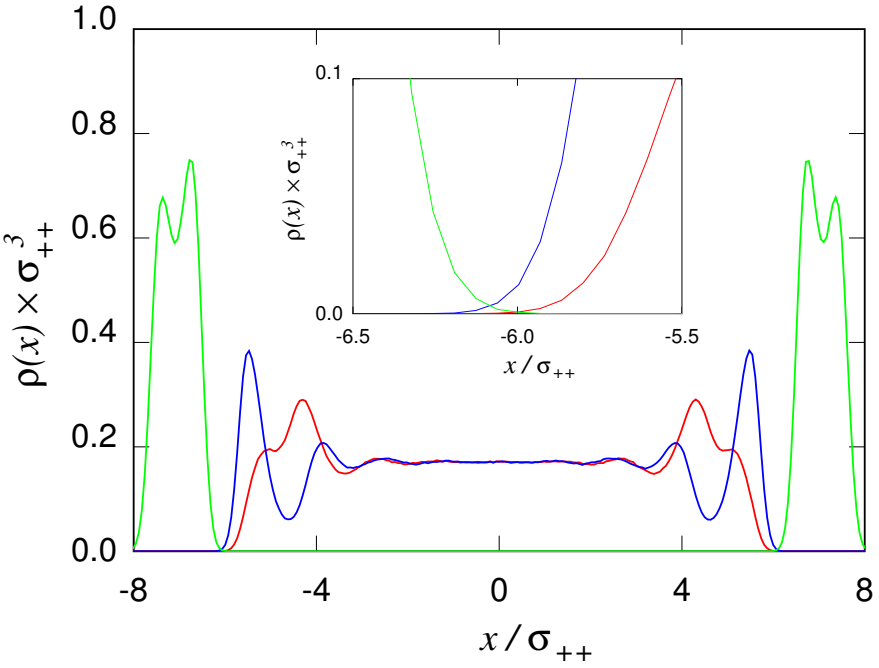

Figure 3.2: Dimensionless density profile of ions across the simulation box and of neutral particles that the walls are made of. $\sigma_{+-} = 1.3$, $\sigma_{--} = 1.6$, $\sigma_{+n} = \sigma_{-n} = 1.5$, at $T = 1$. Red line: cations; blue line: anions; green line: neutral particles. Neutral particles are confined by an harmonic potential to fixed positions distributed on a regular 2D lattice. The inset provides a magnified view of the contact region between the Coulombic fluid and the wall.

The two peaks that can be seen for the neutral wall is due to the vibration of the spring. The particles will be displaced from their lattice position according to the harmonic potential, and the particles will have more space if they move opposite to each in x-direction rather than staying in the lattice or moving in the same direction.

The repulsive interaction of ions and neutral particles is reflected by a gap between the wall and the fluid densities, as shown by the dimensionless total (number) density distribution, $\rho_{tot} \times \sigma_{++}^3$, displayed in Figure 3.3.

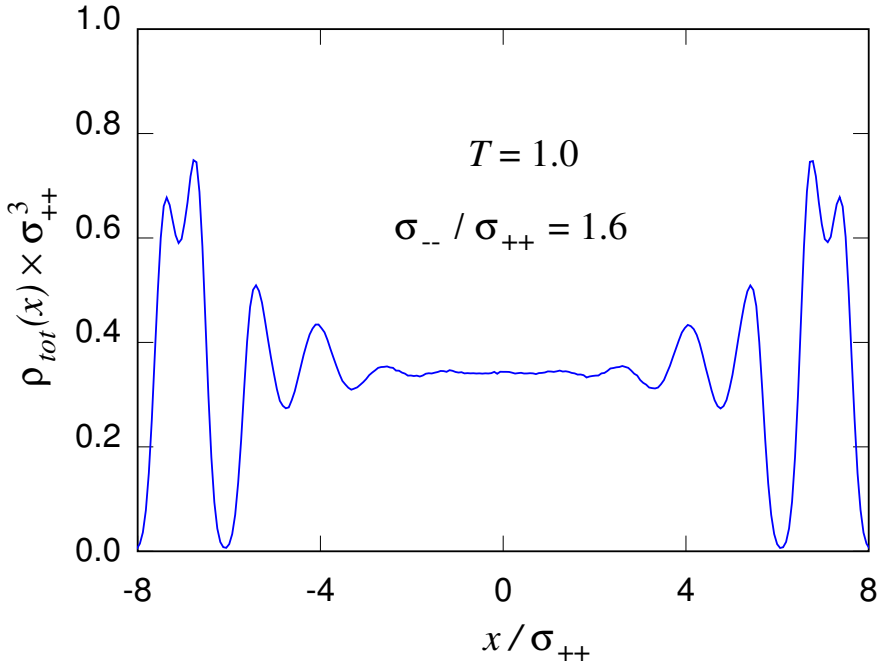

Figure 3.3: Number density profile of all particles, irrespective of their charge. Sample with $\sigma_{--}/\sigma_{++} = 1.6$, $T = 1.0$.

This observation will become relevant in discussing the temperature gradient across the system when the temperatures on the two neutral walls differ (see next section).

From Figure 3.3, the peak to the right of the gap is dominated by anions, the next by cations. This constitutes the origin of a double layer.

The aim of the equilibrium simulations is to analyse the electrostatic double layer in our samples, and to determine its dependence on model parameters such as the ion size and valence, and on thermodynamic conditions such as temperature. The electrostatic double layer is defined from the dimensionless charge density profile, $\rho_Q \times \sigma_{++}^3$.

A limited exploration of different ion/neutral walls interaction has been carried out as well. In these investigations, the primary role is played by the dimensionless charge density distribution, $\rho_Q \times \sigma_{++}^3$, across the interfaces and its temperature dependence for a system of asymmetric ions of the same valence ($Z_1 = -Z_2$), see Figure 3.4.

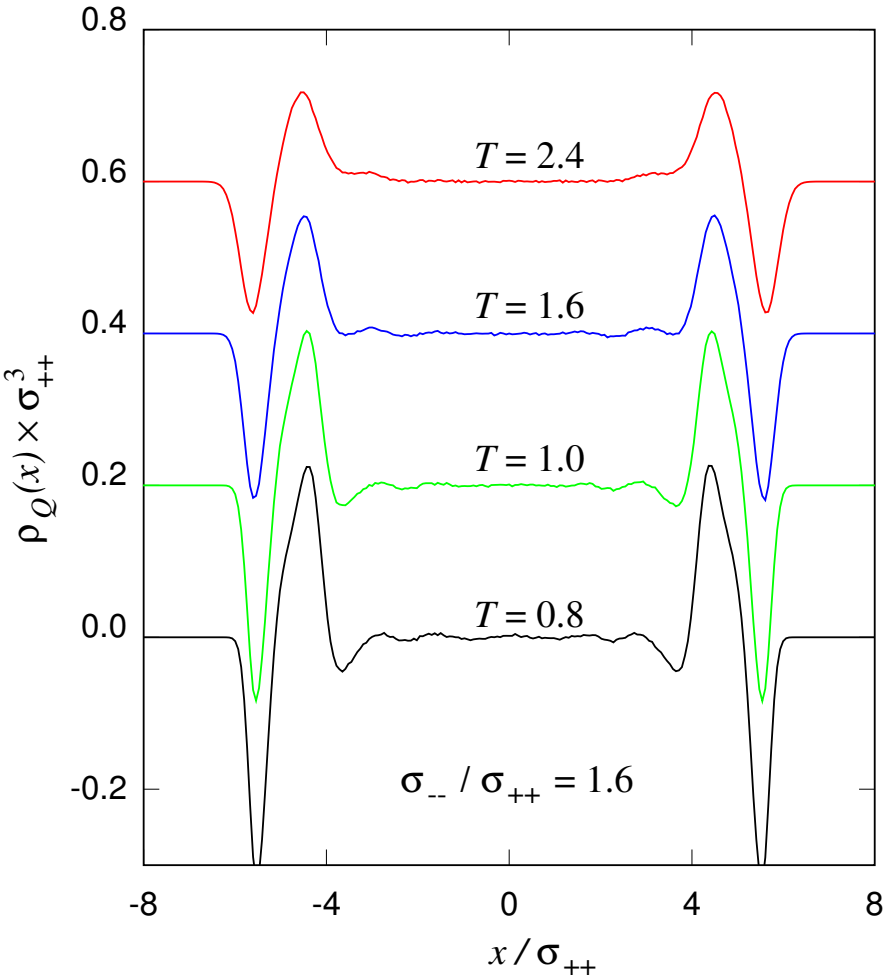

Figure 3.4: Temperature dependence of the charge density profile. $\sigma_{--}/\sigma_{++} = 1.6$. All the curves, except the bottom one, have been shifted for readability.

As can be seen, the charge density ρ_Q almost vanishes in the central portion of the simulation box ($-2.5 \leq x \leq 2.5$), that we identify with the bulk phase in our samples. This is expected due to the homogeneity in this region. Moreover, ρ_Q oscillates close to each interface, and the amplitude of the oscillations increases with decreasing temperature. This can be explained in that decreasing T increases exponentially the importance of correlation among particles. Nevertheless, the dipole of each interface, defined as:

$$D = \int_0^{L_x/2} x \rho_Q(x) dx \tag{3.2.1}$$

increases with increasing T. As seen from Figure 3.4, ρ_Q reaches zero earlier in the low temperature case compared to the higher. Since the dipole is found by integrating $x\rho_Q(x)$, this means that the higher temperature case has a contribution with high magnitude of x that the low temperature do not. This would explain that even though the amplitude of the oscillations are smaller in the high temperature case, the dipole is larger due to the contribution at large values of x. The fact that the dipole increases with T reflects the decreasing ability of the fluid phase to screen the effect of the two walls. This effect is documented in Figure 3.5, which also provides the basis for our discussion of the non-equilibrium results.

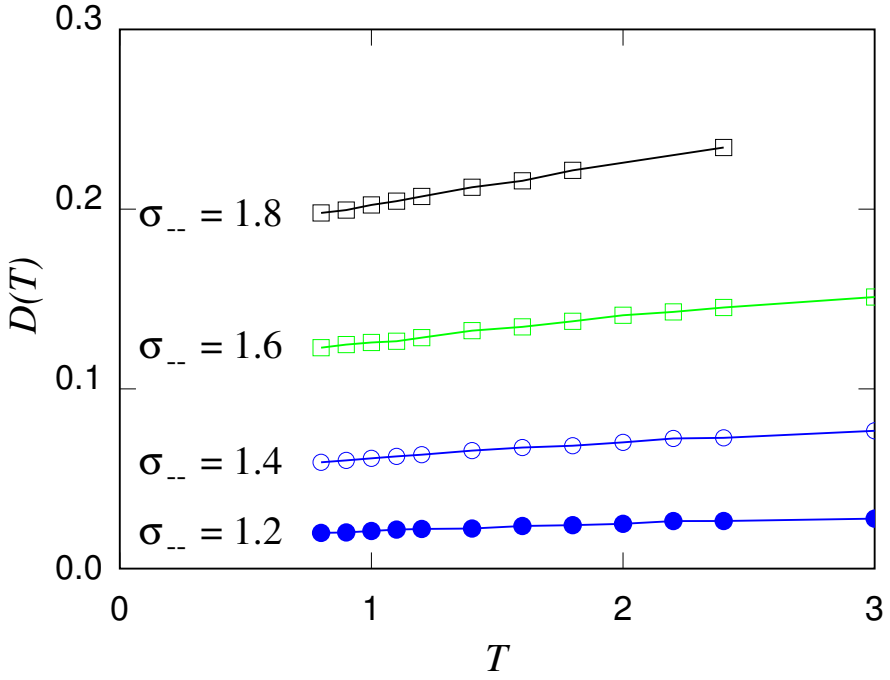

Figure 3.5: Temperature dependence of the interfacial dipole.

The temperature variation of D is apparently larger for systems of larger asymmetry between anions and cations, but it might be worth to point out that the relative temperature variation $(1/D)dD/dT$ is nearly the same, around 0.1, for all systems over the entire $0.8 \leq T \leq 3$ temperature range explored by our simulations.

The charge density profile depends sensitively on the cation/anion asymmetry, as shown in Figure 3.6.

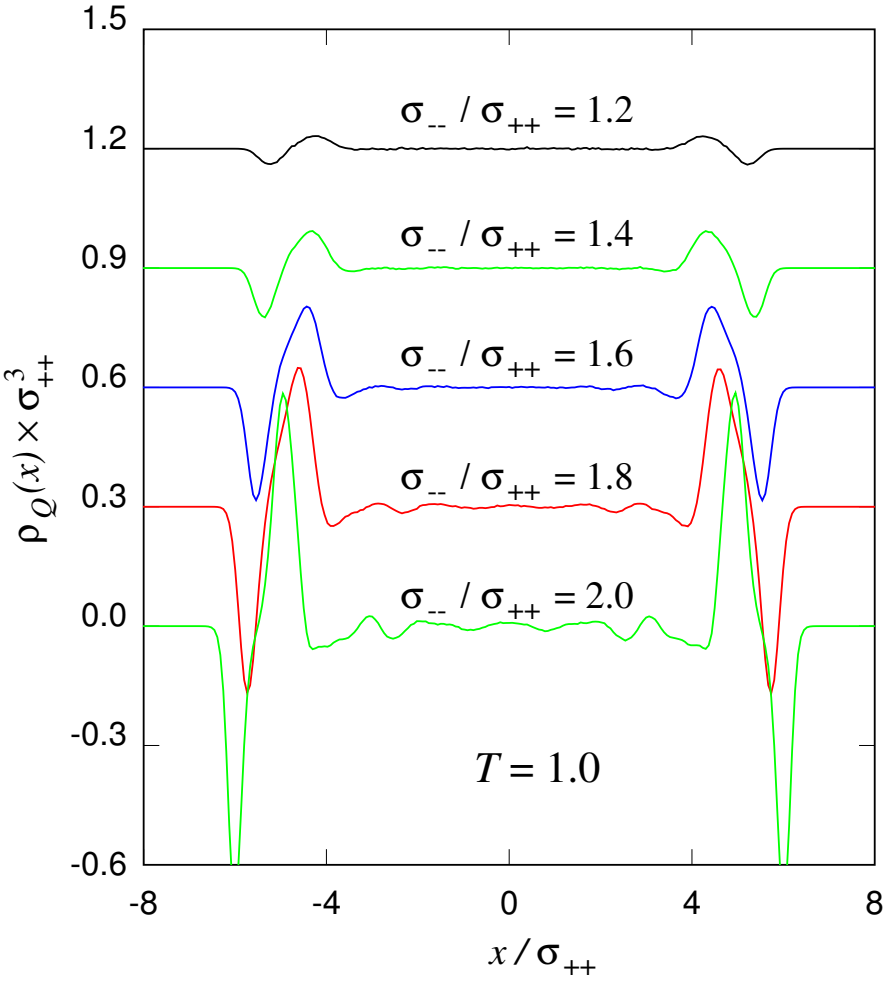

Figure 3.6: Dependence of the charge density profile on the size asymmetry of cations and anions. Equilibrium simulations at $T = 1.0$. All the curves, except the bottom one, have been shifted for readability.

Not surprisingly, the amplitude of the ρ_Q oscillations close to the wall, in particular, increases with increasing asymmetry. We remind, however, that because of the NVE conditions of our simulations, samples of different σ_{--}/σ_{++} are subject to different pressure, and increases with increasing σ_{--}. The pressure in each box is constant, but this constant pressure is different for dissimilar samples

As a further piece of information, we show in Figure 3.7 the charge density profile for three choices of the cation valence. It is apparent that with increasing valence difference, the amplitude of the charge density oscillations at the interface tends to increase.

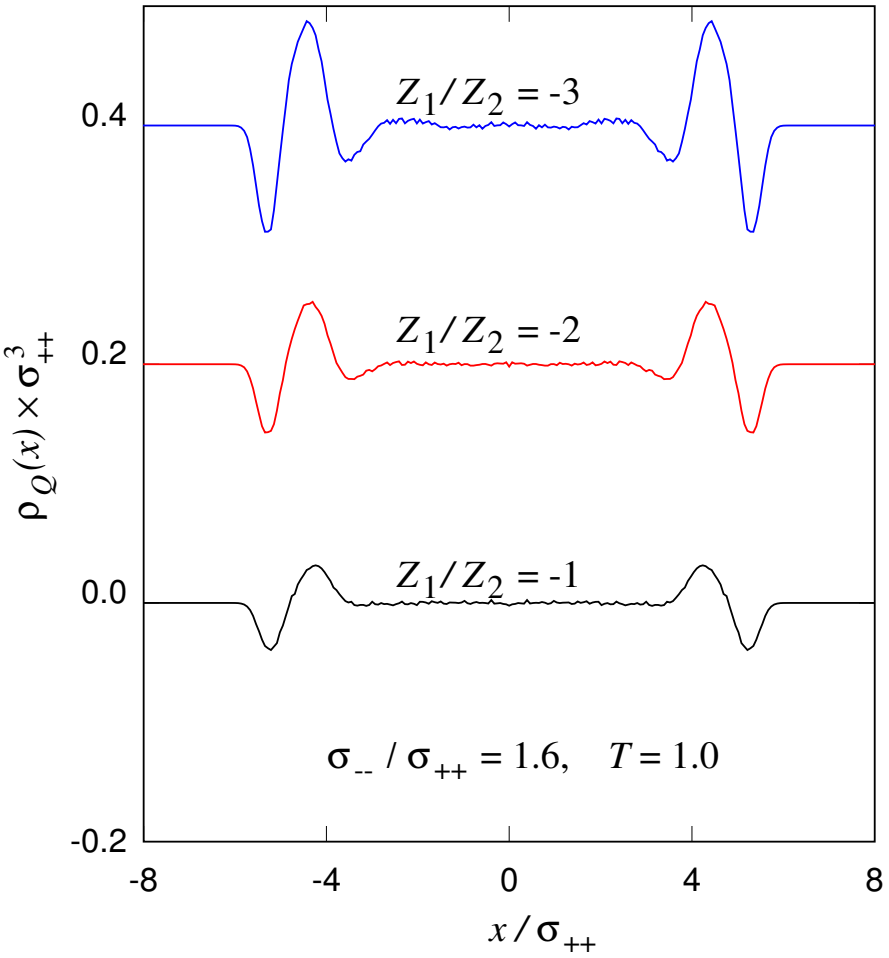

Figure 3.7: Charge density profile for samples of different cation valence. Each sample contained the same number of ions ($N_+ + N_- = 1200$), subdivided between cations and anions in such a way to ensure charge neutrality. Hence, $N_+ = N_- = 600$ for $Z_1 = -Z_2$ case, $N_+ = 400$, $N_- = 800$ for $Z_1 = -2Z_2$, and $N_+ = 300$, $N_- = 900$ in the $Z_1 = -3Z_2$. All the curves, except the bottom one, have been shifted for readability.

The charge density distribution allows us to compute the electrostatic potential $\phi(x)$. By

using using Gauss' theorem, the electric field E can be related to the charge density by

$$E(x) = 4\pi \int_0^x \rho_Q(x')dx' \tag{3.2.2}$$

using that $E(x) = -d\phi(x)/dx$, and an interchange of integration ordering, one can write:

$$\phi(x) = \phi(0) - 4\pi \int_0^x \rho_Q(x')(x - x')dx' \tag{3.2.3}$$

The charge density distribution also allows us to explore the temperature dependence of $\phi(x)$ (see Figure 3.8), its sensitivity on the cation-anion asymmetry (see Figure 3.9) and dependence on cation valence (see Figure 3.10).

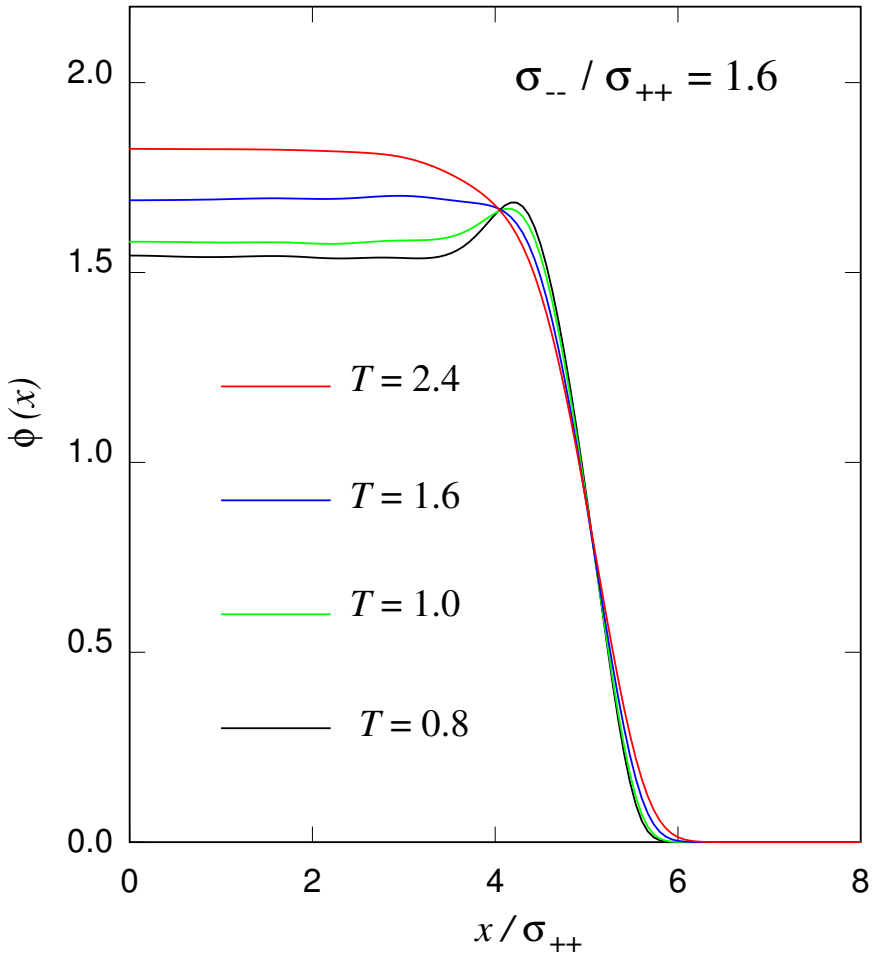

Figure 3.8: Electrostatic potential across the interface. Sample with $\sigma_{--}/\sigma_{++} = 1.6$ at four different temperatures. With increasing T, the change from non-monotonic to monotonic electrostatic potential profile takes place at $T = 1.4$.

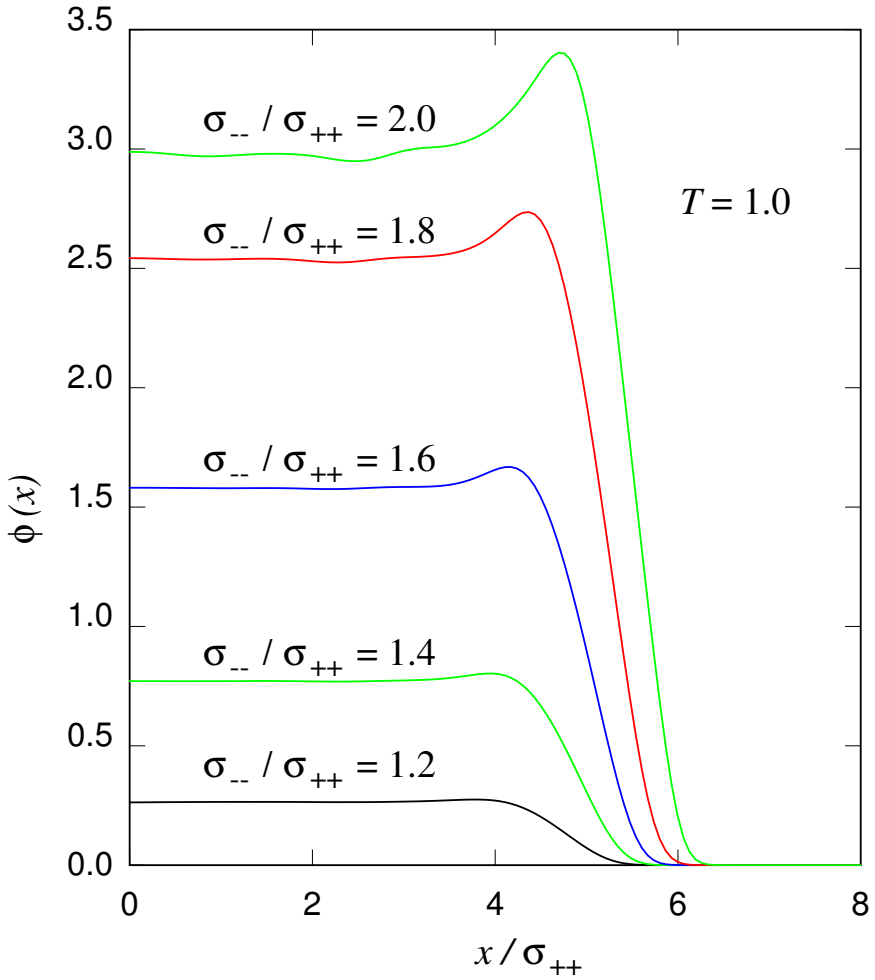

Figure 3.9: Dependence of the electrostatic potential profile on the asymmetry of cations and anions. Equilibrium simulations at $T = 1.0$.

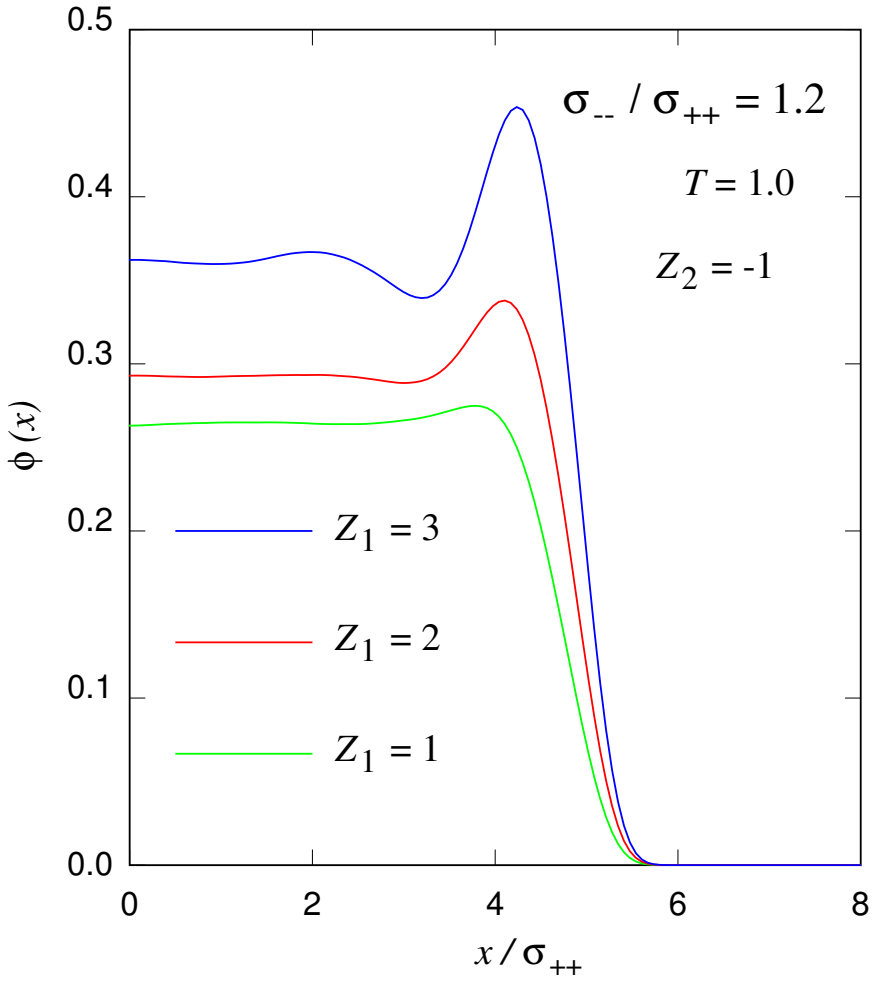

Figure 3.10: Dependence of the electrostatic potential profile on charge asymmetry. Equilibrium simulations at $T = 1.0$.

Elementary electrostatic considerations show that the interface dipole D and the electrostatic potential drop are related. This relation can be found from Eq. (3.2.3), where zero of the electrostatic potential $\phi(x)$ is chosen in such a way that $\phi(L_x/2) = 0$. We then get, using the definition of the dipole from Eq. (4.2.21):

$$\phi(L_x/2) = 0 = \phi(0) + 4\pi \int_0^{L_x/2} x\rho_Q(x)dx = \phi(0) + 4\pi D \tag{3.2.4}$$

This gives $\phi(0) = -4\pi D \implies |D| = |-\phi(0)/4\pi|$.

The reason for the choice of integration limits 0 and $L_x/2$ is because half of the box is a good place to set $\phi(L_x/2) = 0$, due to symmetry. As the charge density is essentially zero in the bulk, is does not really matter where one set the end of the integration limit, as long as it is a sufficient distance from the interface. $L_x/2$ is therefore a convenient choice.

We did not analyse in detail the role of the ion/neutral particle pair potential. A limited exploration has been performed by changing the σ_{+n} and σ_{-n} lengths, retaining, however, the repulsive form (inverse power) of the pair potentials. The results (see Figure 3.11) confirm that tuning the ion/wall interparticle potential as a direct, predictable and sizeable effect on the dipole and electrostatic potential drop at the solid/fluid interface.

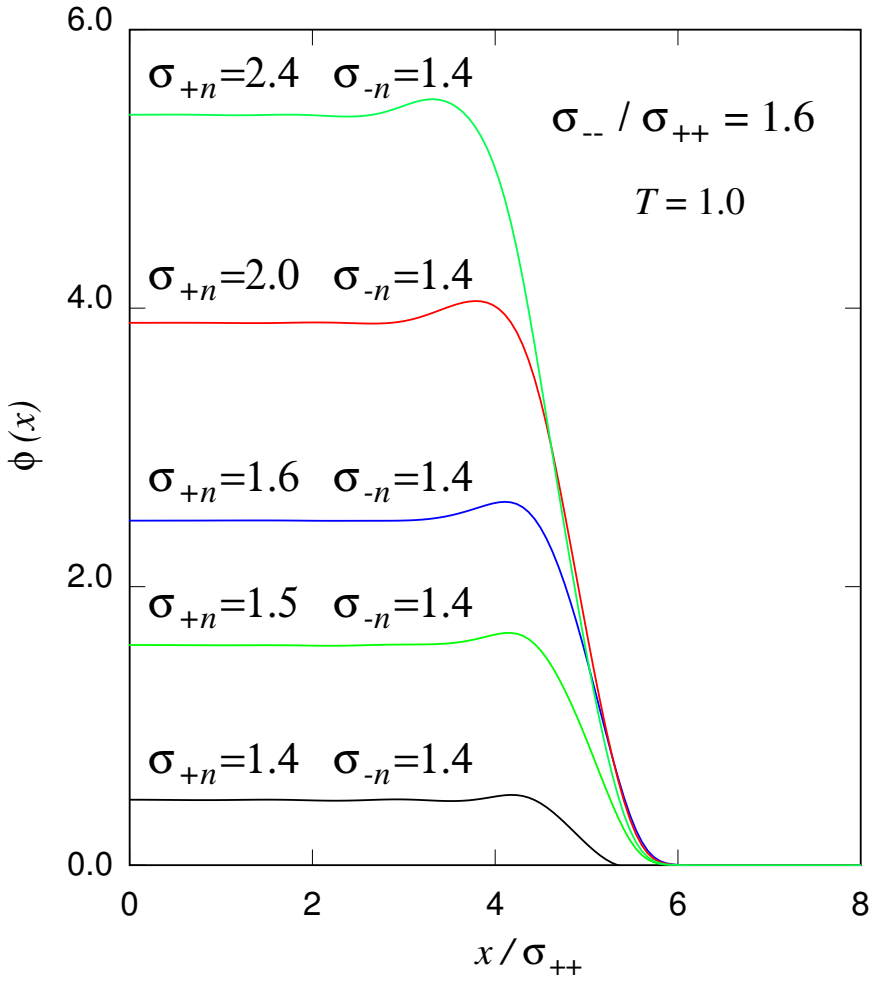

Figure 3.11: Dependence of the electrostatic potential on the interaction between ions and neutral particles on the walls.

3.2.2 Non-equilibrium simulation results

The simulation of the systems listed in Table 3.1 has been extended to non-equilibrium, steady state conditions by imposing two different temperatures T_1 and T_2 to the Langevin thermostats coupled to the left and to the right wall, respectively. More precisely, we carried out simulations for all systems upon setting $T_1 = 1.12$ and $T_2 = 0.88$. The reason for this choice is because the temperature difference cannot be too low due to the errorbar of the

computed dipoles. Neither can it be too large since it would require temperature correction due to the average temperature being too different from the temperature of each wall. Ions in the fluid phase are not directly coupled to a thermostat. The contact of the two walls with the ionic fluid, and the resulting flow of heat from left to right, cause a deviation of the average wall temperature from the target temperature of the thermostat, as apparent from the results listed in Table 3.2.

Table 3.2: Average temperature of the left- ($\langle t_1 \rangle$) and right- ($\langle t_2 \rangle$) wall during non-equilibrium simulations. The two walls are connected to a Langevin thermostat at $T_1 = 1.12$ (left) and $T_2 = 0.88$ (right), respectively. The gradient $\nabla T(x)$ of the local temperature has been estimated by linear interpolation of the simulation data for $-4 \leq x \leq 4$.

Sample #	1	2	3	4	5	6	7
$\langle t_1 \rangle$	1.065	1.055	1.046	1.036	1.031	1.045	1.045
$\langle t_2 \rangle$	0.929	0.937	0.948	0.955	0.960	0.948	0.948
$-10^3 \times \nabla T(x)$	9.168	6.959	5.843	4.918	4.395	5.983	5.751
Sample #	8	9	10	11	12	13	
$\langle t_1 \rangle$	1.046	1.047	1.063	1.062	1.064	1.064	
$\langle t_2 \rangle$	0.947	0.947	0.931	0.932	0.931	0.931	
$-10^3 \times \nabla T(x)$	5.933	6.100	10.266	2.429	9.023	7.972	

The contact with the two walls at different temperatures gives origin to a dependence on position x of the local temperature $T(x)$ in the ionic fluid phase (see Figure 3.12).

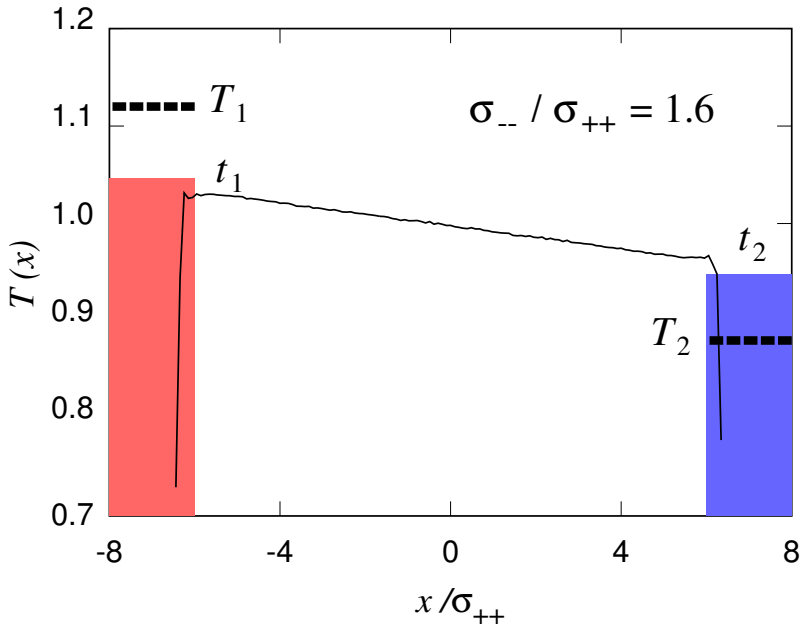

Figure 3.12: Local temperature distribution $T(x)$ in the non-equilibrium, steady state simulations. T_1 and T_2 are the target temperature of the Langevin thermostat on the left and on the right wall, respectively. t_1 and t_2 are the average temperature of neutral particles, again on the left and on the right wall, respectively.

Here the *local temperature* $T(x)$ is defined simply in terms of the average kinetic energy of particles whose x' coordinate satisfies $x - \frac{L_x/201}{2} \leq x' \leq x + \frac{L_x/201}{2}$. As shown in Figure 3.12, the dependence of T on x is linear over most of the ionic liquid range. A remarkable anomaly (a drop) from T_1, T_2 to t_1, t_2, reminiscent of the Kapitza resistance of quantum fluids (see Ref. [25] for a discussion of the Kapitza resistance in the context of classical fluids), is apparent at the two fluid/wall interfaces. These spikes correspond to the narrow layers over which ions feel the repulsive potential of the neutral particles, raising their average potential energy, and decreasing their kinetic energy. This observation emphasises the drawbacks of interpreting the average kinetic energy in terms of temperature in a inhomogeneous system. On the other hand, outside the range of the neutral/ion repulsion, average kinetic energy can be used to measure temperature. The linear interpolation of the simulation results for $-4 \leq x \leq 4$ allows us to assign a temperature gradient to each samples, whose value is listed in Table 3.2. The values estimated for different samples are very close to each other, but still

differ by more than their error bar, reflecting the different thermal resistance of the ionic fluid subject to different external pressure.

The aim of this stage of computation is the identification of the asymmetry in the electrostatic potential due to a different temperature of the two neutral, planar and parallel electrodes that confine the fluid phase (see Figure 3.1). The primary result of these simulations, therefore, is the total dipole across the simulation box, whose average value $\langle D_x \rangle$ is reported in Table 3.3. This quantity results from the near compensation of the interfacial dipoles at the two opposite interfaces, and, for this reason, its computational estimate is affected by a large statistical error bar. To allow for an independent assessment of the accuracy of the dipole computation, we report in Table 3.3 also the (large) standard deviation, and the autocorrelation time t_a of the fluctuating dipole, the total simulation time being listed in Table 3.1.

Table 3.3: Average dipole $\langle D_x \rangle$ of samples simulated under the non-equilibrium, steady state conditions described in the text. The standard deviation and the autocorrelation time of the fluctuations $D(t)$ are reported as well.

Sample #	1	2	3	4	5	6	7
$\langle D_x \rangle$	0.30 ± 0.07	0.39 ± 0.08	0.34 ± 0.10	0.10 ± 0.15	3.2 ± 0.2	0.28 ± 0.14	0.80 ± 0.13
st. dev.	23	23	23	23	23	24	24
$\langle t_a \rangle$	4	6	9	22	62	11	9
$10^4 \times \delta Q$			2.40				
Sample #	8	9	10	11	12	13	
$\langle D_x \rangle$	0.37 ± 0.13	0.27 ± 0.13	0.12 ± 0.06	0.04 ± 0.05	0.06 ± 0.07	0.24 ± 0.06	
st. dev.	23	23	24	24	23	23	
$\langle t_a \rangle$	10	11	2	1	2	2	
$10^4 \times \delta Q$							

Admittedly, the error bar is still large with respect to the estimated values, but several internal consistency checks confirm the global reliability of the picture provided by simulation. First of all the sign of $\langle D_x \rangle$ is consistent with the observation that $D(T)$ grows with increasing T. Moreover, the size of $\langle D_x \rangle$ is consistent with a rough estimate based on $\langle D_x \rangle \sim [D(T_1) - D(T_2)]$. To support this view, we computed the temperature derivative $dD(T)/dT$ from the results displayed in Figure 3.5. Then, we compared the total dipole of each simulated sample with the linear estimate $(T_1 - T_2)dD(T)/dT$. The comparison,

reported in Table 3.4, shows an agreement of computed and predicted dipoles that, although far from quantitative, is at least qualitatively correct.

Table 3.4: Comparison of the total dipole D_x measured in the non-equilibrium simulations with the linearised estimate $(T_1 - T_2)dD(T)/dT$, where the derivative is computed at $T = [T_1 - T_2]/2$.

Sample #	1	2	3	4	5
$\langle D_x \rangle$	0.30 ± 0.07	0.39 ± 0.08	0.34 ± 0.10	0.10 ± 0.15	3.2 ± 0.2
$(T_1 - T_2)dD(T)/dT$	0.38	0.47	0.32	0.62	2.3

The major deviation, observed for sample #4, is likely to be due to an anomaly of $dD(T)/dT$ that could be seen in our data at $T \sim 1$. The qualitative prediction of such a complex behaviour by a simple relation is a remarkable result, that opens the way to a deeper understanding of the Seebeck effect.

Finally, the average dipole is also consistent with the average distribution of charge across the interfaces that is illustrated in the following figures.

The net dipole $\langle D_x \rangle$ has to result from an asymmetry of charge distribution with respect to the centre of the simulation box. This is confirmed by the plot of the skew-symmetric component of $\rho_Q(x)$, whose average over time is shown in Figure 3.13. It is apparent from the figure that each interface is not strictly neutral. In other word, we observe that:

$$\delta Q = \int_{-\infty}^{0} \rho_Q(x)dx = -\int_{0}^{\infty} \rho_Q(x)dx \neq 0 \tag{3.2.5}$$

while at equilibrium the vanishing of δQ is strictly imposed by exact conditions [17]. The δQ charges are listed in Table 3.3. The build-up of a net charge at each interface, that has to be compensated at the opposite interface, could be seen as a remarkable example of long-range correlation due to non-equilibrium conditions [14]. The net charges give origin to a weak electric field across the *bulk* fluid phase that is needed to prevent the ionic conduction that, according to Onsager relations, should complement the flow of heat.

The argument pointing to $(T_1 - T_2)dD(T)/dT$ as a simple approximation for the dipole moment of samples simulated under non-equilibrium conditions has a counterpart in terms

of the charge density distribution. In this case, the skew-symmetric component of the charge density has to be approximated by $(T_1 - T_2)d\rho_Q(x)/dT$. The comparison of this prediction with the results of non-equilibrium simulations is shown in Figure 3.13. Also in this case, the agreement is not quantitative, but nevertheless remarkable for such a simple approximation.

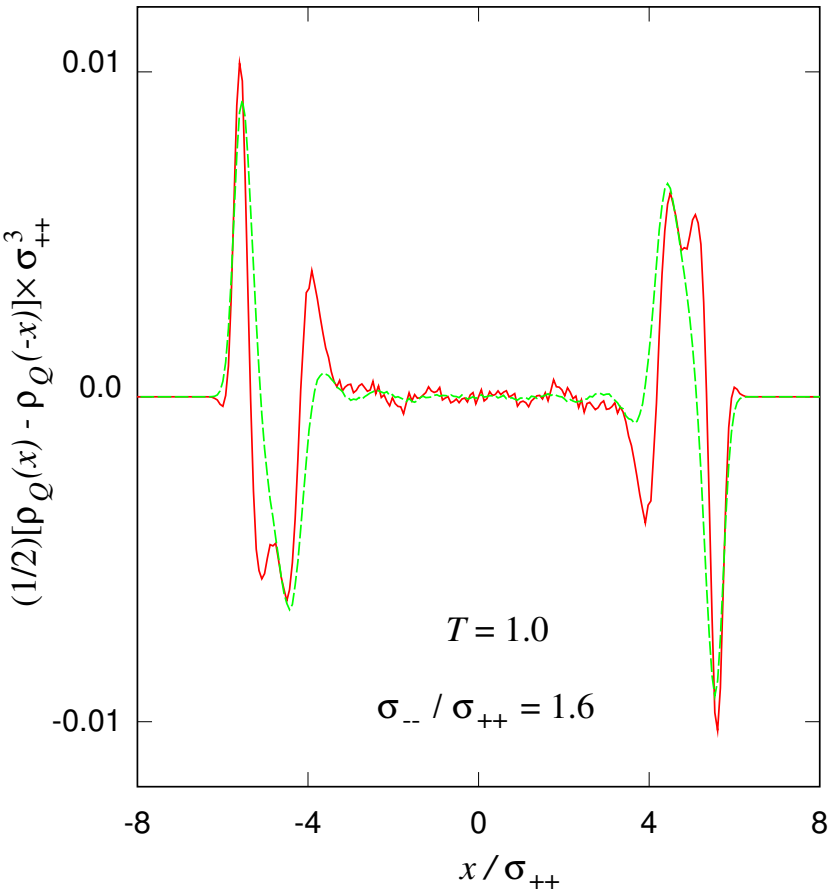

Figure 3.13: Full line, red: skew-symmetric component of the charge density distribution in a sample simulated under non-equilibrium, steady state conditions. Dash line, green: prediction of the skew-symmetric component of the charge density by $(T_2 - T_1)d\rho_Q/dT$. The temperature derivative $d\rho_Q/dT$ has been computed from the results of equilibrium simulations.

Properties at the surface

Excess properties at the surface are of great interest with respect to thermodynamics, see e.g. Kjelstrup and Bedeaux [4]. In order to investigate these properties, a Gibbs dividing surface has to be defined.

Instead of intergrating throughout half of the box, the integration limits are changed. The starting limit is defined as the point to the left where the density is 5% of the bulk value. This is chosen as the Gibbs dividing surface. The point where the integration ends is defined from the first point the density deviates 5% from the bulk value, starting from the middle of the box and going to the left. This will constitute the interfacial region, and this represents the integration limits to get the excess values.

The temperature in this interfacial region was found by by averaging the kinetic energy of the particles in the surface layer. The surface temperatures can be seen in Table 3.5.

Table 3.5: Average temperature of the left- (T_1^s) and right- (T_2^s) interfacial region during non-equilibrium simulations. The surface layer is next to a wall which is connected to a Langevin thermostat at $T_1 = 1.12$ (left) and $T_2 = 0.88$ (right), respectively.

Sample #	1	2	3	4
T_1^s	1.036	1.031	1.024	1.019
T_2^s	0.962	0.966	0.971	0.973

Not surprisingly, the temperature in the surface layer is lower for the left layer and higher for the right layer, compared to the average temperature of the walls given in Table 3.2. This temperature drop is due to the Kapitza resistance.

With the assumption of local equilibrium, these surface temperatures can be used to find the surface dipole, D^s, from the plot of the interfacial dipole as a function of temperature computed at equilibrium, which is shown in Figure 3.5. The surface dipole found at each interface, $D^s(T_1^s)$ and $D^s(T_2^s)$, as well as the total dipole D_x^s can be seen in Table 3.6.

The values for the total surface dipole are the same order of magnitude as the ones for the average total dipole shown in Table 3.3. However, the values in Table 3.6 has an errorbar that causes the errorbar of D_x^s to comparable than the signal, due to the small temperature difference between T_1^s and T_2^s.

Table 3.6: Surface dipole of the left- ($D^s(T_1^s)$) and right- ($D^s(T_2^s)$) interfacial region. The surface temperature is computed from non-equilibrium simulations, while the interfacial dipole was found from equilibrium simulations with the assumption of local equilibrium.

Sample #	1	2	3	4
$\lvert D^s(T_1^s)\rvert$	6.17	18.07	36.91	59.17
$\lvert D^s(T_2^s)\rvert$	6.09	17.91	36.70	58.87
D_x^s	0.08	0.15	0.21	0.31

3.2.3 Doubling the system size

The scaling of thermodynamic properties as a function of the separation between the walls is a crucial aspect whose analysis will clarify many of the microscopic mechanisms of the Seebeck effect.

For this reason, computations have been carried out for systems whose size L_x has been doubled, consisting of twice as many ion pair ($N_+, N_- = 1200$ instead of 600). The visual comparison of the two simulated systems is shown in Figure 3.14

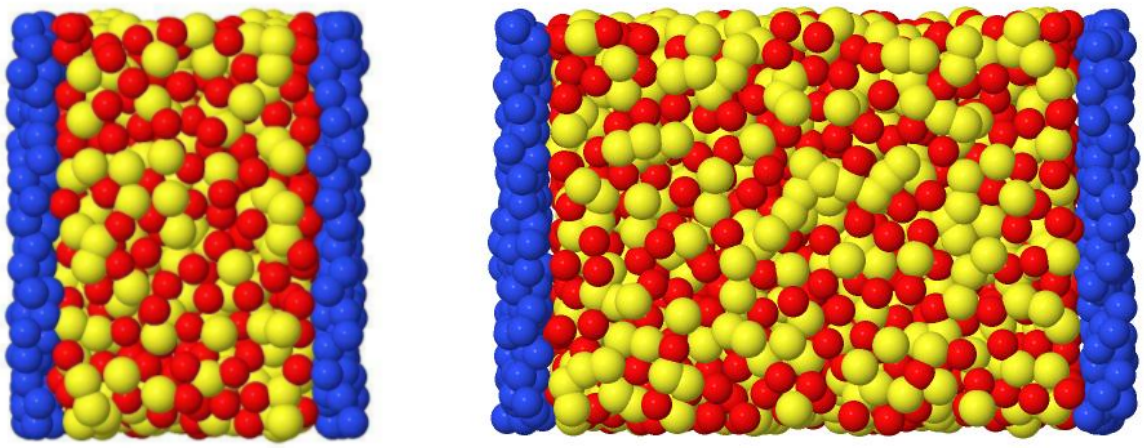

Figure 3.14: Comparison of the simulation snapshots for the regular system with $N_+, N_- = 600$ (to the left) and the larger system with $N_+, N_- = 1200$ (to the right).

The temperature difference (nominal temperature at the walls: $T_1 = 1.12$, $T_2 = 0.88$) has been kept constant, implying that the gradient has been decreased by a factor of 1/2 in going from the regular system to the enlarged system.

The temperature dependence of the dimensionless charge density profile for the enlarged system can be seen in Figure 3.15

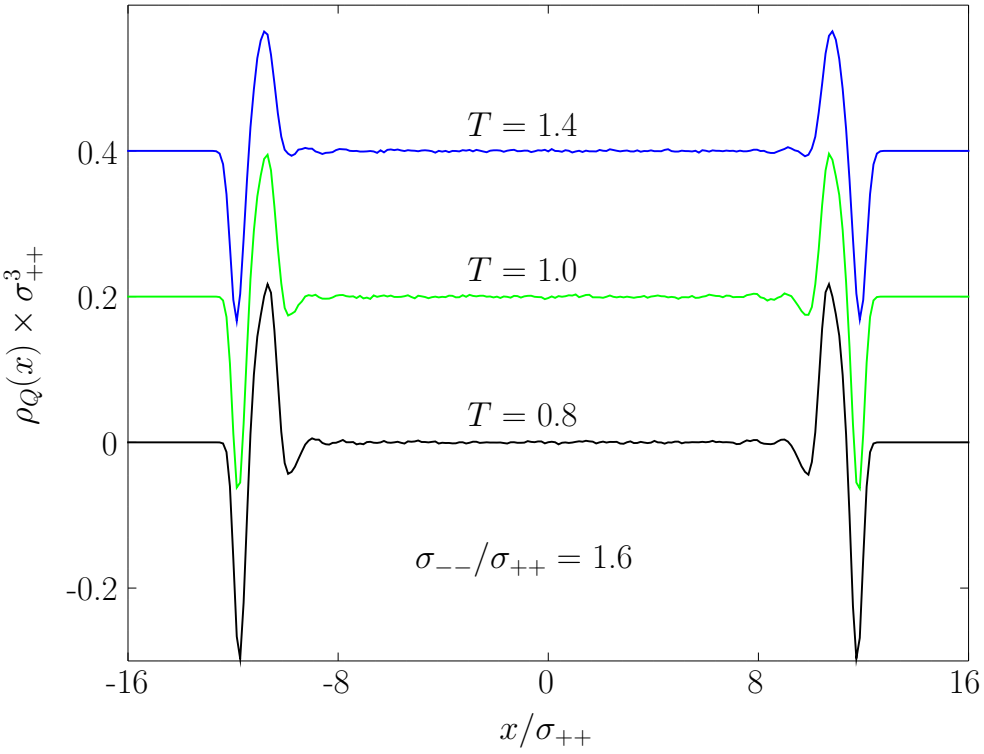

Figure 3.15: Temperature dependence of the charge density profile. $\sigma_{--}/\sigma_{++} = 1.6$. All the curves, except the bottom one, have been shifted for readability. Double-size system.

Note the extended bulk region compared to Figure 3.4. The comparison between the dipoles for the regular and enlarged system can be seen in Figure 3.16

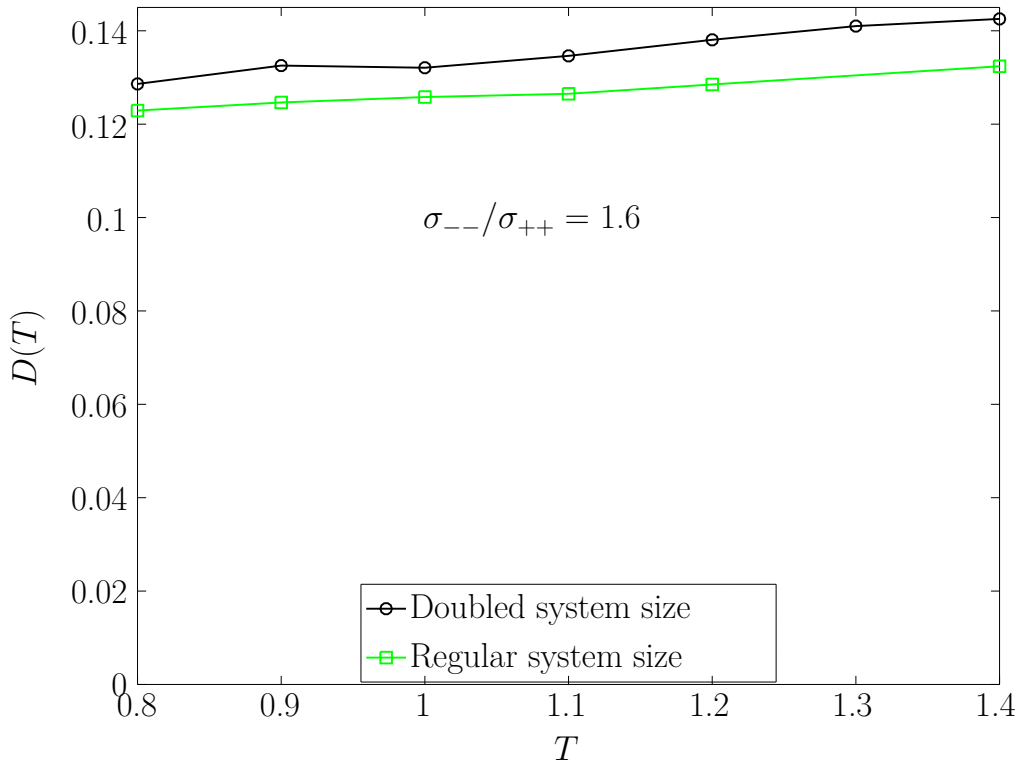

Figure 3.16: Temperature dependence for the interfacial dipole. $\sigma_{--}/\sigma_{++} = 1.6$.

As can be seen, there is a systematic difference between the dipoles. However, one has to note that the pressure is not strictly conserved upon doubling the box, which could explain some of the deviation.

The electrostatic potential profile can be seen for different temepratures in Figure 3.17.

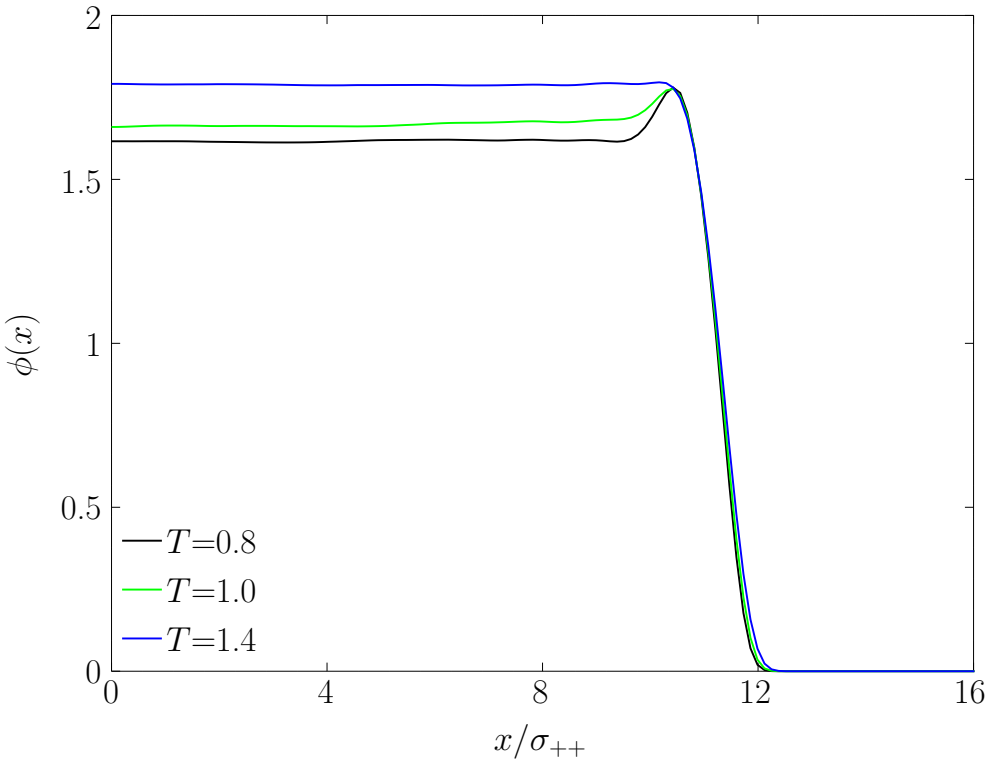

Figure 3.17: Electrostatic potential across the interface. Sample with $\sigma_{--}/\sigma_{++} = 1.6$ at three different temperatures. With increasing T, the change from non-monotonic to monotonic electrostatic potential profile takes place at $T = 1.4$. Double-size system.

A plot of the skew-symmetric component of $\rho_Q(x)$ for the double-size system can be seen in Figure 3.18.

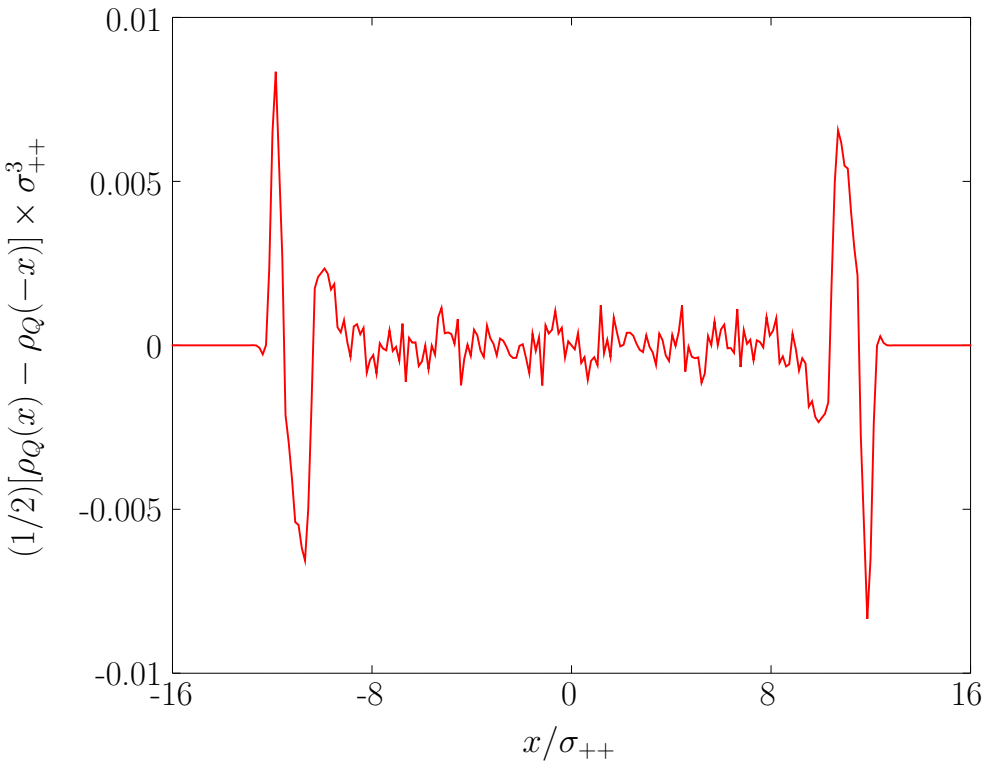

Figure 3.18: Full line, red: skew-symmetric component of the charge density distribution in a sample simulated under non-equilibrium, steady state conditions. Double-size system.

Also in this case, there is a net charge δQ on each interface which are equal in magnitude, but of opposite sign. This net charge gives rise to the Seebeck effect.

The results from this stage of our simulations ($N_+, N_- = 1200$) are consistent with those of the previous stage ($N_+, N_- = 600$). The analysis of scaling, however, is still underway.

3.3 Conclusion and summary

Extensive molecular dynamics simulations have been carried out for an idealised model of a Coulombic fluid confined in between two parallel walls made of neutral particles, whose interaction with the fluid ions is the same for the two walls. All particles follow Newton's

equations of motion, while wall particles obey a Langevin dynamics at a target temperature T, that can be different for the two confining walls.

Two sets of simulations have been performed: The first at equilibrium conditions, with the Langevin thermostats of the two walls set at the same temperature T_0. The second at non-equilibrium conditions, with the two walls kept at different temperatures $T_1 \neq T_2$, thus giving origin to a steady flow of heat. Both sets were analyzed in this report.

The first set of simulation provides a microscopic view of electrification at solid/liquid interfaces, complementing the picture offered by previous simulation studies [21, 22, 23]. We explore, in particular, the dependence of the dipole at each interface on the size and/or charge asymmetry of cation and anions, and also on the interparticle potential between wall and the ions in the fluid phase. The temperature dependence $D(T)$ of the interfacial dipole was computed, and the dipole was found to be increasing with increasing temperature. The electrostatic potential, which is related to the dipole by a factor 4π, was found to be increasing with increasing anion/cation asymmetry, and well as with increasing interaction between the cations and the neutral particles in the wall. It was also found to be increasing with larger cation valence compared to anion valence. These variations are expected.

The results from the non-equilibrium simulations show that the asymmetry between the two walls is reflected in the imbalance of the surface dipole at the two interfaces, resulting in a net dipole moment of the whole simulated sample.

With the chosen boundary conditions, the difference $D(T_1) - D(T_2)$ provides a qualitatively correct prediction of the total dipole in the simulation cell, pointing to a *local* description of thermo-electric phenomena at each interface, at least for systems under steady state non-equilibrium conditions, and provided the temperature gradient is not exceedingly large.

An interesting feature emerging from the simulation is that under non-equilibrium conditions the electrification of the two opposite interfaces is not limited to a dipole, but includes a net charge δQ. The global neutrality of the system is ensured by the fact that the charges at the two interfaces exactly compensate each other, but the non-vanishing average value of δQ represents a major novelty with respect to the equilibrium conditions, in which the

exponential screening of charge is established by exact statistical mechanics results.

Admittedly, the net charge $\pm\delta Q$ at each interface is tiny (see Table 3.3), but it provides the electric field across the entire system that is required to prevent flow of charge that, according to Onsager relations, should accompany the heat flow. In addition, the pair of $\pm\delta Q$ represents an example of correlation across macroscopic distances (from one interface to the opposite one) whose relevance in non-equilibrium systems under steady state conditions is discussed [14].

This is a very interesting problem, worthy of deeper understanding and more analysis. The size dependency of the dipole moment is one of the things worthy of more investigation, as well as more analysis on the thermodynamics related to excess properties and entropy production, using the methods described in [4]. Further work related to this problem involves using more chemically detailed and more quantitative models of molten salts in contact with metal electrodes for the exploration of electrification and transport in heterogeneous (solid/fluid) systems.

Chapter 4

More realistic models: Alkali carbonates

4.0 Motivation

4.0.1 Recent experiments

The idealised model has been useful as a general prototype of Coulomb fluids in a steady state thermal gradient. To compare with experiments, however, we need more realistic models that in our case aim at reproducing primarily the properties of Li_2CO_3, but also Na_2CO_3 and K_2CO_3, all belonging to the alkali carbonate family.

The motivation for this choice is the recent experiments done by Børset et al. [26] in the non-equilibrium thermodynamics group of Prof. S. Kjelstrup, in which they report the Seebeck coefficient for molten lithium carbonate. They found it to be around 0.88 mV/K. This is higher than the usual values from the traditional thermoelectric devices based on semiconductors, which is typically 0.2 mV/K. More complex compounds of ionic liquids have also been investigated by other authors. The room temperature organic ionic liquids [5] studied by Abraham et al. [6] gives even larger Seebeck coefficients of 1.5-2.2 mV/K. Because of the well recognized relation of the Seebeck effect and entropy, the apparent good performance of molecular ionic liquids might be attributed to the enhanced role of entropy in molecular species of increasing size and complexity. Being liquid at room temperature is crucial, as it enables them to be used for energy harvest at low temperature.

Focusing on a molecular ionic system of intermediate complexity, the computational in-

vestigation of lithium carbonate could give better insight on why ionic liquids, and molten salts in particular, gives such large Seebeck coefficients. This could lead to novel design of thermoelectric devices with better efficiency, which can be used to generate more electricity from e.g. waste heat in the metallurgy industry and consequently increase the global efficiency these energy-intensive industrial processes.

4.0.2 Properties and applications of carbonates

In its simplest meaning the term "carbonate" identifies salts of the carbonic acid, H_2CO_3. Carbonate salts consist of inorganic and organic ions, giving origin to a large family of compounds. Our discussion concerns primarily the simplest case of these molecules, arguably presented by alkali carbonates, M_2CO_3 for short.

Thermoelectric devices are not the only applications of interest for alkali carbonates. It is also interesting to look at the properties of molten carbonates due to their application in fuel cells, see e.g. Dicks [27]. As he discusses, a combination of lithium and sodium carbonates seems to be preferred as electrolyte compared to either pure components. Studies have previously addressed the performance of Li_2CO_3/Na_2CO_3 electrolyte compared to the older Li/K carbonate mixture [28]. Not only have there been done experiments regarding the properties of these carbonates, but also simulations [29] have been carried out in order to try to give valuable insight on the molecular structure and on dynamical properties like diffusion and electric conductivity.

The formation of Li_2CO_3 is also important for battery technology based on lithium [30].

Lithium carbonate not only has applications related to energy technologies. It has also been used successfully as a medication in treating bipolar disorder [31], reducing in particular the high suicide risk. This is a benefit currently not seen with other medications [32]. However, the biochemical mechanism on how the compound stabilises the mood is still unknown [33].

A study of the properties of lithium carbonate can apparently not only be useful for designing electrochemical and fuel cells, but also for drug design with the objective to treat

mental illness. Na_2CO_3 and K_2CO_3 have also other uses than electrochemistry. Na_2CO_3, commonly known as soda ash, is used to make glass and in washing powder to soften the water (i.e. precipitate calcium and magnesium ions) [34]. K_2CO_3, also known as potash, is used as a fertiliser [35].

Carbonates of monovalent metals are not the only carbonates worthy of attention; carbonates of divalent metals, like $MgCO_3$ and $CaCO_3$, are important minerals in geochemistry [36].

Uncovering more knowledge about these compounds is therefore of great interest.

4.1 Previous simulations of molten alkali carbonates

The main empirical model for studying alkali carbonates with molecular dynamics simulations has arguably been the force field made by Janssen and Tissen [37, 12], which is based on a Coulomb term with a Born-type repulsive part. As noted by Janssen and Tissen: "This form of potential was originally developed for the alkali halides with the rock salt structure [38] and is widely used for simulations of molten salts [39, 40]". The model was made by parameterisation of *ab-initio* computations based on the Hartree-Fock (HF) method. The Janssen-Tissen (JT) model has been used by several authors, e.g. by Koishi et al. [41] and quite recently by Ottochian et al. [29]. The functional form belongs to the OPLS force field [42], which is implemented in most major molecular dynamics packages.

Investigation of molten carbonates, especially the structure of Na_2CO_3, has been done by Wilding et al. [43] As they note: "...molten carbonates are important in development of molten carbonate fuel cells and as battery electrolytes [27]. Despite their recognized importance the structure of these liquids is not well-known." In their study they used "high energy X-ray diffraction, containerless techniques and computer simulation to provide insight into the liquid structure." Their computer simulation is based on the JT model, where they use a harmonic spring for the C−O bond rather than a rigid CO_3^{2-} ion.

The structure of pure molten Li_2CO_3 and K_2CO_3 has already been studied by X-ray diffraction, Raman spectroscopy, infrared spectroscopy and molecular dynamics simulation

by Koura et al. [44] However, Kohara et al. [45] mentions that the detailed structures of these melts are not yet fully known. Due to the inaccuracy of using X-ray techniques when dealing with light atoms such as lithium, they motivate the need for neutron diffraction measurements which they perform in their study. They found the average C−O distance to be approximately 1.31 Å, which is larger than the one found by X-ray of around 1.27 Å. However, it is worth noting that neutron diffraction is not easy to do with molecular species, especially with elements other than hydrogen[1], which means that these results should be taken with a pinch of salt. Still, the distance of 1.31 Å between carbon and oxygen corresponds very well to the bond lengths obtained from DFT computations in this work, shown in Table 4.3. In addition, using X-rays to find the structure requires a form factor to describe the shape of the electron cloud of the atom. This is not needed for neutron diffraction [46].

Another force field for molten Li_2CO_3 and Na_2CO_3 has been developed by Habasaki [47], where a different form of the potential is used. However, this model is not as widely used as the JT model, and is therefore not as thoroughly tested.

Studies has also been done for carbonates of divalent metals, e.g. the development of a force field for $CaCO_3$ by Jackson and Price [48] and more recently by Raiteri et al. [36] for the application of studying growth of calcium carbonate from aqueous solution.

An important factor that most of these models does not take into account is that the carbonate structure changes based on the proximity of cations. In Figure 4.1, the ground state geometry for a carbonate ion and a single Li_2CO_3 unit computed by *ab-initio* with the PBE functional can be seen[2].

[1]Hydrogen plays a crucial role in neutron scattering measurements, because of its large cross-section, especially for incoherent scattering. However, the large difference in cross-section between hydrogen and deuterium makes it possible to exploit isotopic systems.

[2]Geomtry optimisation and computation of harmonic vibrational frequencies by CPMD, see section 4.2

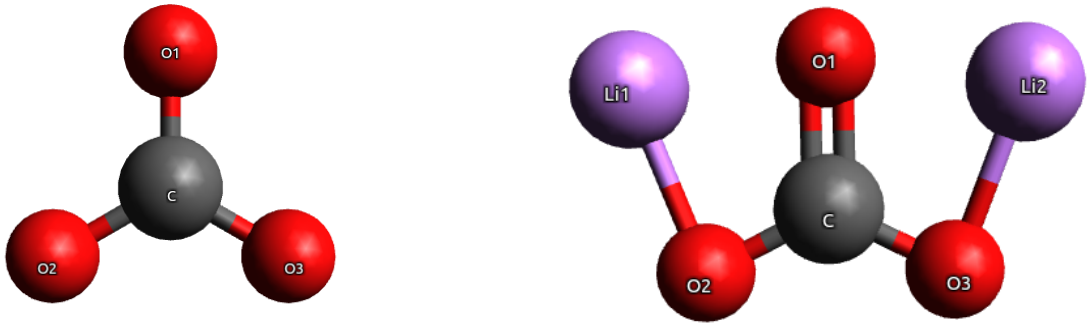

(a) CO_3^{2-} (PBE) (b) Li_2CO_3 (PBE)

Figure 4.1: Ground state geometry computed for CO_3^{2-} (a) and Li_2CO_3 (b) using the PBE functional.

In the carbonate ion, seen in Figure 4.1a, there is an equal distance between the carbon and the three oxygen atoms. The structure is also planar, and a rotation 180° around each C−O axis will leave it unchanged. We say that the carbonate ion has a D_{3h} symmetry, meaning it fulfills all the symmetry operations of the D_{3h} point group.

Lithium carbonate, however, belongs to the point group C_{2v}. With the placement of the lithium ions as shown in Figure 4.1b, the bond length between C and O1 will lengthen and the C−O2 and C−O3 bond will become shorter, compared to the carbonate ion. The fact that the symmetry of CO_3^{2-} is different from Li_2CO_3 has usually been ignored in the previous simulations, where the bond length between carbon and oxygen is the same regardless of the position of the lithium ions. This feature, conceptually important, fortunately has little influence on the properties computed by MD of large samples at liquid-like conditions.

Research has been done regarding intra-molecular potentials for carbonate in other structures. In a study by Masia et al. [49], a new intra-molecular force field was developed for the electrolyte system ethylene carbonate−Li^+. In their research, geometry optimazation and vibrational analysis of a single ethylene carbonate molecule and the ethylene carbonate−Li^+ complex was performed with Møller-Plesset pertubation of second order (MP2). MP2 is an *ab-initio* method that is believed to be more accurate than Hartree-Fock. Their new force

field were successful in describing the low frequency modes, which is relevant for liquid dynamics, more accurately than the existing AMBER force field. They also investigate how the coordination of lithium ions induces shift in these frequencies. The force field by Masia et al. has been applied by Jorn et al. [50] to investigate Li-carbonate/electrode interface relevant for Li-ion energy storage systems.

There is another aspect worth noting regarding the previous simulation. Due to computational cost, the polarisation has usually been ignored although polarisation is expected to play an important role because of the oxygen anions. This could also lead to inaccuracies in the model. An example of polarisable force field used to simulate molten carbonates is given in the paper by Borodin et al. [51]

As far as we know, there has not yet been done any *ab-initio* simulations of alkali carbonates, only computations for a few molecules. It is feasible with today's technology to simulate a system of several thousand particles, but it is quite costly in terms of computational time[3]. The reason why it might not yet have been done could be because the possible gain from such a large simulation does not seem to justify the cost.

4.1.1 A few remarks on force fields

One might ask why the JT model is still being used in 2015/2016 [29, 43], although it was developed over 25 year ago based on Hartree-Fock (HF) computations. Since then, the *ab-initio* methods available on the market has greatly improved. Especially the density functional theory (DFT) has been shown to give accurate results at low cost. It is also worth noting that the computers are much faster now than 25 years ago, giving the possibility of using even more precise quantum chemistry calculations. One would think that it should be fairly easy to develop a new, improved force field with today's technology that surpasses the JT model from the previous century. Still, the JT model or a modification of it seems to be mainly used in the majority of communities doing molecular dynamics on alkali carbonates.

There are several explanations that could be the reason for this. One of them is the

[3]See the paper by Jorn et al. [50] for an example of *ab-initio* simulations for relatively simple organic carbonates.

robustness of the model, illustrated by the relative insensitivity of the results even on the choice of atomic charge. Most simulations uses a charge of 1.54 e for carbon and -1.18 e for oxygen [12], resulting in -2 e in total for the carbonate ion. However, other distribution of charges has also been used which gives fairly similar results, as long as the total charge of the ion is -2 e and the M_2CO_3 molecule is neutral. A model that is not too sensitive to this is beneficial, as the charge distribution in the carbonate ion could be different depending on the location of lithium with respect to the carbonate ion.

A restriction that may also have hindered the development of a new force field concerns the functional form. In standard molecular dynamics packages, a collection of functional forms are implemented that one can choose between. One of them is the Born-Mayer-Huggins (BMH) potential that is used in the JT model. One could instead write one's own MD code, but to parallelise it efficiently would require much work and profound knowledge on the communication of nodes in the parallel machine it is going to be used on. The standard packages, however, has already been optimized for use on parallel computers, giving fast codes with little or no knowledge about parallel computations.

4.2 Models and methods

4.2.1 Models: Homogeneous vs. non-homogeneous, equilibrium vs. steady state

All our simulations for carbonate systems were carried out at thermodynamic equilibrium, meaning there is no net macroscopic flow of matter or energy. The simulations were deemed to have been run long enough for equilibration to occur, meaning that there is no time evolution of the physical properties.

"A homogeneous thermodynamic system is defined as the one whose chemical composition and physical properties are the same in all parts of the system, or change continuously from one point to another." [52] Our motivation to simulate a homogeneous system is to determine structure and transport properties. In the homogeneous case, the system was made up

consisting solely of Li_2CO_3, Na_2CO_3 or K_2CO_3 molecules. The initial configuration was made using Packmol [53]. This is a program which can be used to place molecules randomly in a confined space, while avoiding close contacts between atoms. This confined space is defined by our simulation box. Periodic boundary conditions were enforced, meaning that is a particle were to leave the box at one end, it would reappear in the other end. This was done in order to better mimic bulk properties without the need for many thousands of molecules, since each particle sees an infinite number of periodic images of itself and the other particles. Computing all the pair interactions becomes very expensive, so a truncation can be used. This means that beyond a specific distance (typically 10 Å), the contribution is ignored. However, as discussed by Frenkel and Smit [15], for long-range interactions such as the Coulomb interaction a truncation could lead to large errors. Let us assume one chooses to truncate the potential at a distance r_c. The contribution of the tail in the potential $V(r)$ is

$$V^{tail} \propto \int_{r_c}^{\infty} V(r) r^2 dr \tag{4.2.1}$$

which will diverge unless $V(r)$ decays faster than r^{-3}, which is not the case for Coulomb interactions. One therefore has to employ techniques that can calculate long-range interactions at low cost. Ewald summation is one of those. The idea behind this method is to divide the interaction into a short-range contribution and a long-range contribution. The short-range contribution converges fast in real-space, while Fourier analysis is used on the long-range contribution, since this will converge fast in Fourier space. Even though Ewald summation can correctly describe the long-range interaction, it scales as $N^{3/2}$ where N is the number of particles in the system [15]. For large systems, it is therefore desirable to use a more efficient method. By using the particle-particle particle-mesh method (pppm) [54], the atom charges are mapped to a $3D$ mesh. The $3D$ fast Fourier transform (FFT) is used to solve Poisson's equation on the mesh, and then the electric field is interpolated back to the atoms. This method scales as $N \log(N)$, and is therefore almost always a faster choice [55].

The model for alkali carbonate employs a force field due to Janssen and Tissen, which is

described in section 4.1.1.

A heterogeneous system, on the other hand, is defined as one consisting of two or more homogeneous bodies [52]. Heterogeneous is the same as saying non-homogeneous or inhomogeneous, and these words are being used interchangeably in the literature.

In our non-homogeneous case, the system was made up of Li_2CO_3, Na_2CO_3 or K_2CO_3 molecules (or an equimolar mixture of Li_2CO_3 and Na_2CO_3) confined between two layers of neutral atoms oriented along the x- and y-directions, giving a simple model of the ionic liquid between two electrodes. The system consists for that reason of two homogeneous subsystem; the neutral wall and the alkali carbonate in the bulk. An interface, or boundary, perpendicular to z separates these two systems, in which the chemical properties are not like those in the bulk and neither those in the wall.

The hexagonal structure of the (111) surface of gold was used to make the layers of neutral atoms. These atoms were fixed to the lattice positions with a harmonic spring, so that the force on each atom would be $\mathbf{F}_{spring} = -K_{spring}\mathbf{r}_d$, where K_{spring} is the spring constant and $\mathbf{r}_d$ is the displacement from the equilibrium position given by the lattice positions.

The use of periodic boundary conditions along x- and y-direction ensured that the wall would be continuous in terms of the hexagonal structure. This boundary condition was not only enforced in the direction parallel to the wall, but also in the direction perpendicular to the wall (z-direction). The reasoning for this is the same as in the idealised system; to be able to use the $3D$ version of the Ewald summation. To be precise, approaches enforcing periodicity along one plane and even along a single direction are known [56, 57, 58]. but computationally inefficient.

In our computations the periodicity was longer than the separation between the wall, to give a volume of empty space outside the walls. The first obvious reason for this is because the neutral particles on the wall are able to move with the attachment of the spring, and without the empty space the particles from one wall would collide with the ones from the other. The most important reason for the empty space, however, is to avoid spurious interactions and

correlations in the motion of ions across the walls. This behaviour is something we want to avoid, thus the motive for having the extra empty space.

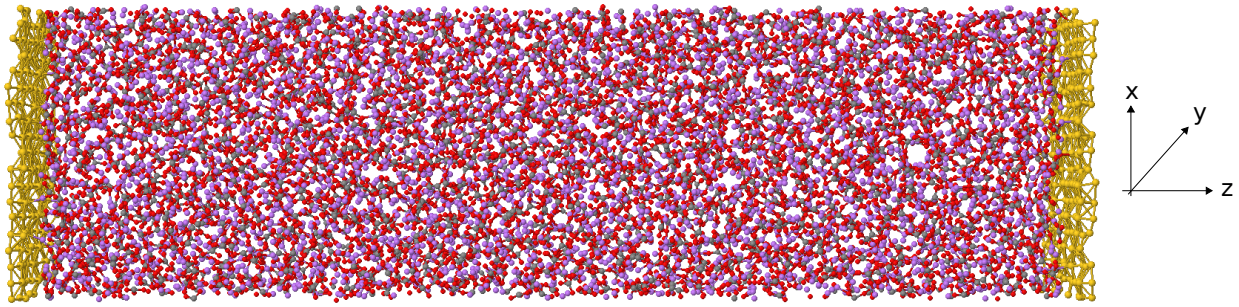

Figure 4.2: Snapshot of the system with 2048 Li_2CO_3 molecules between neutral walls, visualised in Jmol [59]. The black, red and purple spheres represents carbon, oxygen and lithium, respectively. The golden spheres represents the wall.

In the case of neutral walls, an empty layer of a few nanometers is sufficient to ensure the decoupling of opposite interfaces. The picture is different and more challenging in the case of charged walls.

Charged wall

A case was also studied in which a charge was put on the atoms constituting the walls. Both walls had the same magnitude of charge, but of opposite sign compared to each other. In this way the simulation box is globally neutral.

The inhomogeneity due to the confining walls, and the electrostatic forces due to a charge on the walls can, in principle, cause a local separation of the positive and negative charge on the fluid side, giving origin to the so-called double layer that accompanies the formation of every surface and interface [16], even those nominally neutral and insulating.

Basic statistical mechanics theories [17] however, state that at equilibrium the amplitude of the charge separation decays exponentially moving away from each wall, and in a conducting fluid each interface is strictly neutral. In the ideal case, since the wall/fluid/wall composite layer sits in an otherwise empty space, the computation of electrostatic forces is simple. By symmetry the particle and charge distribution depend only on the coordinate

z perpendicular to the wall, and the problem reduces to solving Poisson's equation in $1D$, with boundary conditions:

$$\lim_{z\to\pm\infty} \phi(z) = 0 \tag{4.2.2}$$

$$\lim_{z\to\pm\infty} E_z(z) = 0 \tag{4.2.3}$$

Let us assume that we have a wall of surface charge $\sigma_w A$ at $z = z_{lw}$ and another one of surface charge $-\sigma_w A$ at $z = z_{rw}$, z_{lw} being as far from the left end of the simulation box as z_{rw} from the right end. In order to find the electrostatic potential ϕ resulting from having charges of opposite sign on each wall, the electric field E is found from the charge density distribution by the use of Gauss's law. This law can be written in differential form as:

$$\nabla \cdot \mathbf{E} = \frac{\rho_Q}{\epsilon_0} = 4\pi k_e \rho_Q \tag{4.2.4}$$

where $\mathbf{E}$ is the electric field vector, ρ_Q is the charge density, ϵ_0 is the vacuum permittivity and k_e is Coulomb's constant. In cartesian coordinates, $\nabla \cdot \mathbf{E} = dE_x/dx + dE_y/dy + dE_z/dz$. Looking along the z-direction (and letting E denote E_z), we get:

$$E(z) = \begin{cases} 0 & \text{if } z < z_{lw} \\ 4\pi k_e \int_{z_{lw}}^{z} \rho_Q(z')dz' & \text{if } z_{lw} \le z \le z_{rw} \\ 0 & \text{if } z > z_{rw} \end{cases} \tag{4.2.5}$$

since $E(z) = -d\phi(z)/dz$, one can get the electrostatic potential by integration:

$$\phi(z) = \begin{cases} 0 & \text{if } z < z_{lw} \\ -\int_{z_{lw}}^{z} E(z')dz' & \text{if } z_{lw} \le z \le z_{rw} \\ 0 & \text{if } z > z_{rw} \end{cases} \tag{4.2.6}$$

We emphasize that these results hold for a single isolated slab. The picture is different if we use periodic boundary conditions also along the z-direction, which is perpendicular to the

interface. In this way, the wall($\sigma_w A$)/fluid(0)/wall(-$\sigma_w A$) sandwitch is periodically repeated in space. This changes the boundary contitions for Poisson's equation ($\nabla^2\phi = -4\pi k_e \rho_Q$), and this effect has to be considered to compare our computations to the results of experiments on isolated macroscopic interfaces.

A plot of the charge density, electric field and electrostatic potential across the interface computed during one of our simulations with periodic boundary condictions is shown in Figure 4.3.

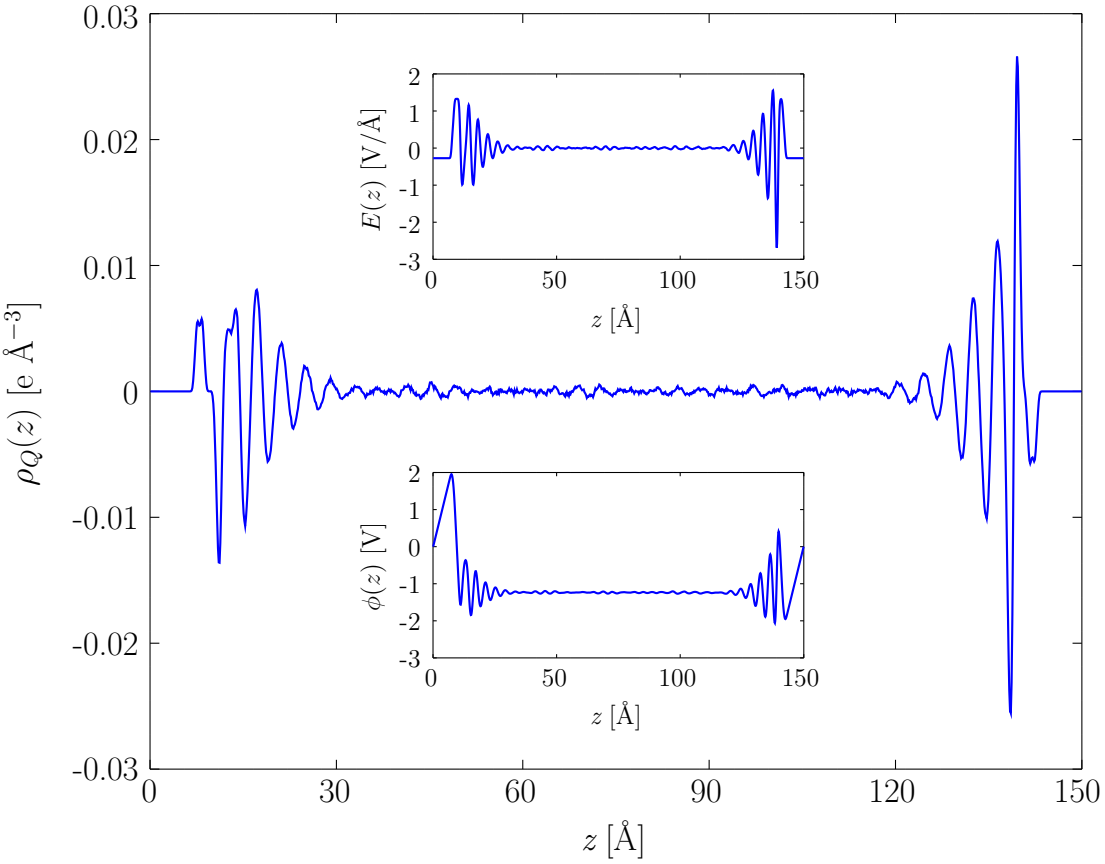

Figure 4.3: Charge density profile for Li_2CO_3 between planar walls in the case of having a charge on each wall. The upper and lower insets are the profiles for the electric field and electrostatic potential, respectively, across the simulation box.

The influence of periodic boundary conditions on the solution of Poisson's equation is apparent if one checks the validity of the perfect screening theorem. A naive point of view

is that the net charge on each interface should be equal to zero, since the ions are free to move [17]. However, using PBC we find that there is a net positive and negative charge on the left and right interface, respectively. In other words, the charge on the walls are larger in magnitude that the one in the fluid. The net charge was observed to decrease in magnitude when the empty space outside the walls increased. This is because periodicity and symmetry impose a non-vanishing electric field in the empty region between two periodic repetitions. Since the molten salt is an electrical conductor, the electric field has to be zero in the bulk.

More on detail due to the system being periodic, $\phi(L_z)$ has to be equal to $\phi(0)$ in order for $\phi(z)$ to be a continuous function throughout all the periodic images. Thus $E(0)$ is not necessarily equal to 0 outside the walls, as it would have been in an ordinary capacitor. $E(0)$ is therefore set to a value such that $\phi(L_z) = \phi(0)$, and this is required to make the electric field between the walls vanish in the periodic arrangement. The field on the exterior region of the slab depends on the system periodicity.

The value of the exterior field (see Figure 4.3) is computed as follows: Let us assume that the periodicity is L_z. A simple sketch of the system can be seen in Figure 4.4.

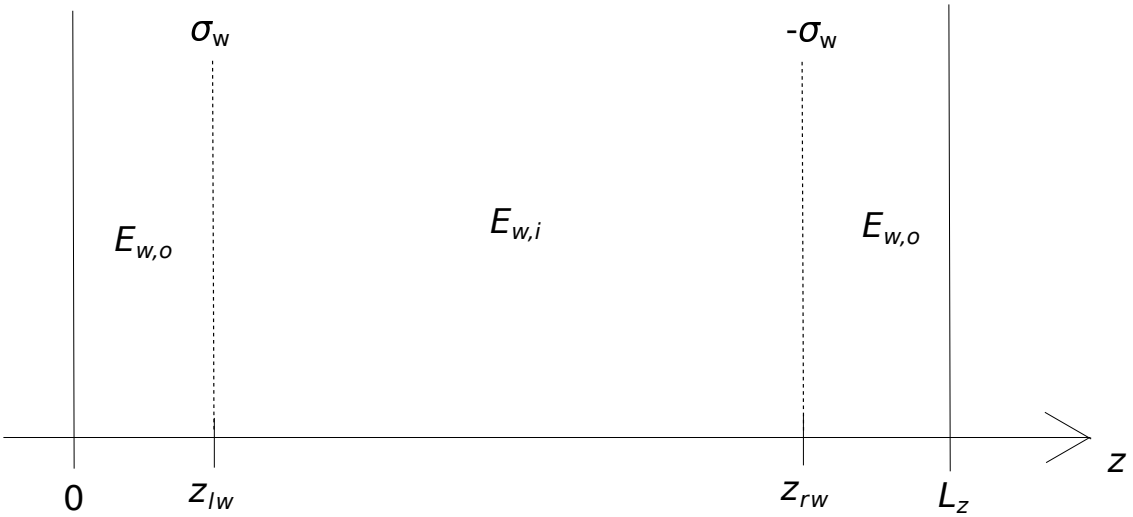

Figure 4.4: A simple sketch of the simulation box with two walls.

$E_{w,o}$ denotes the electric field outside and $E_{w,i}$ denotes the field inside (between the walls). In z-direction, the electrostatic potential $\phi(z)$ can be found for different regions. If the walls

were to have zero width, one will get (setting $\phi(0) = 0$):

$$\phi(z) = \begin{cases} -E_{w,o}z & \text{if } 0 \leq z < z_{lw} \\ -E_{w,o}z - E_{w,i}(z - z_{lw}) & \text{if } z_{lw} \leq z < z_{rw} \\ -E_{w,o}z - E_{w,i}(z_{rw} - z_{lw}) - E_{w,o}(z - z_{rw}) & \text{if } z_{rw} \leq z < L_z \end{cases} \tag{4.2.7}$$

where z_{lw} and z_{rw} is the anchor points of the particles that constitues the left and right wall, respectively. The periodicity in z-direction, L_z, is such that it is equal to $z_{rw} + z_{lw}$.

From Gauss' law and (4.2.7), we get:

$$E_{w,i} = E_{w,o} + 4\pi k_e \sigma_w \tag{4.2.8}$$

$$E_{w,o} = -\frac{4\pi k_e \sigma_w L_i}{L_z} \tag{4.2.9}$$

where $L_i = z_{rw} - z_{lw}$. Inserting eq. (4.2.9) into eq. (4.2.8), we get

$$E_{w,i} = 4\pi k_e \sigma_w \left(1 - \frac{L_i}{L_z}\right) \tag{4.2.10}$$

If the periodicity $L_z \to \infty$, we are back to the $E_{w,i} = 4\pi k_e \sigma_w$ relation of elementary (non-periodic) capacitors. If the system is periodic, the solution violates now this simple prediction, but the deviation is early predictable using eq. (4.2.10). Ions in the fluid react to the electric field on the wall, and accumulate at the interface in order to screen $E_{w,i}$. Therefore, if we impose boundary conditions, or if we change the periodicity of boundary conditions, we need to compare systems of equal $E_{w,i}$ and different σ_w. As a test of this statement, we simulated two systems. In the first system, $\sigma_w A = 11.7$ e and $L_z = 150$ Å. In the second system, $L_z = 166$ Å. σ_w thus had to be decreased according to eq. (4.2.10) in order for the electric field between the walls to remain constant. The charge density profile for both cases can be seen for a 0.2 ns (2×10^5 steps) simulation in Figure 4.5.

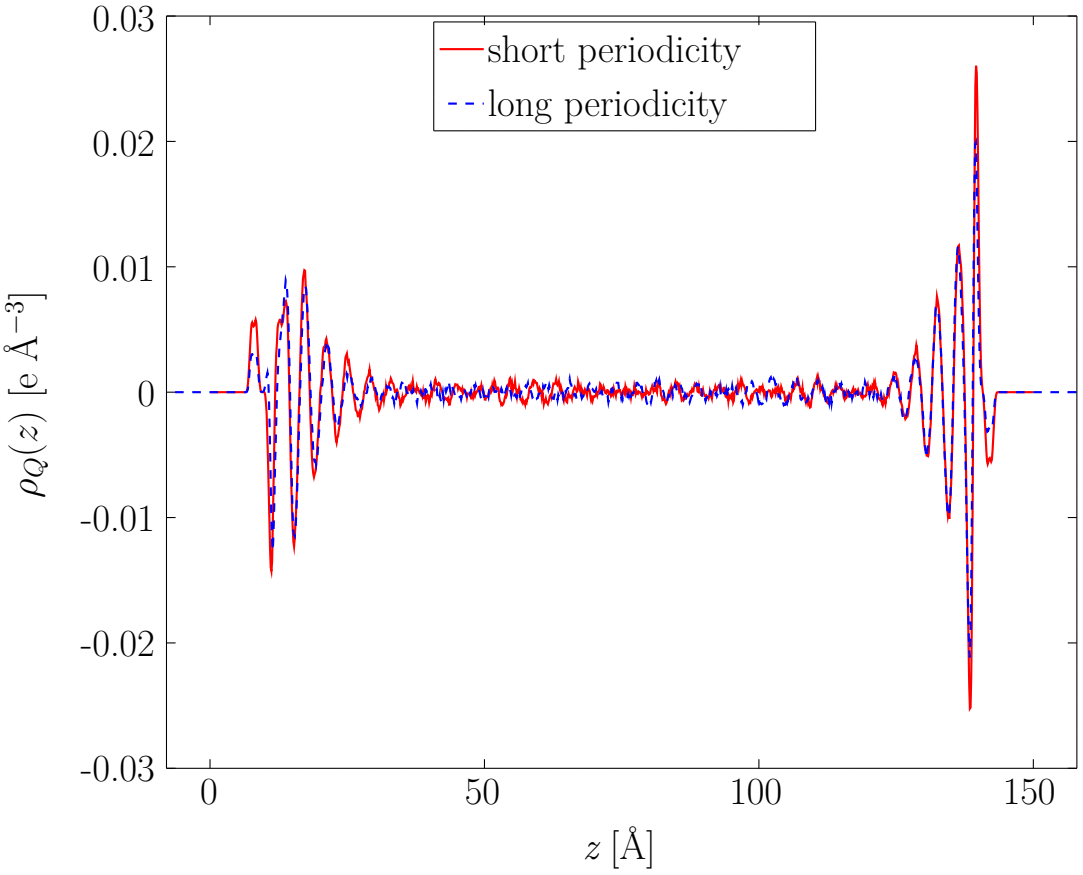

Figure 4.5: Charge density profile for Li_2CO_3 confined between two planar neutral walls for two different periodicities.

As can be seen, the two plots are more or less superimposed. The deviation is most likely due to noise, or the fact that eq. (4.2.10) is not precisely correct, since the walls do have a width in our simulations.

Improvement of the model for the wall; adding image charges

In our model, each wall is treated as having a homogeneous distribution of surface charge. More precisely, each particle on the wall have the same charge, that in most of our simulations corresponds to zero charge. However, even in the case of a neutral wall, the assumption of uniform charge distribution is generally not valid for metal electrodes, since polarisation and the equalisation of the electrostatic potential on the metal side imply the formation of the

so-called *image charges*, that, in the ideal metal case, fully compensate the net charge of the ions on the fluid side.

This aspect has been neglected in most of the few simulations of metal/electrolyte interfaces that are available in the literature. Valuable exceptions are listed and commented upon by Shelley et al. [60]. Because of this scarcity of explicit modelling, the role of image charges in real interfaces is still under debate.

Since image charges arise from the divergence of the dielectric response function of metals in the limit of zero frequency and long wavelengths ($\epsilon \to \infty$), Iori et al. [61] proposed to associate a Drude oscillator (in the original point-charge or in a new rod-like representation) to each particle on the metal side. The dielectric constant of this system does not diverge, but it might be made large by a suitable choice of the model parameters. This model has been parametrised and used to simulate gold electrodes, and is known as the GolP force field. Although intriguing, the model has many limitations, the most important being represented by the fact that metal atoms (Au atoms, in this case) cannot move, but are constrained to a fixed crystal structure.

To overcome the GolP limitations, we: (i) introduced an explicit many-body force field for the metal particles; (ii) improved on the "high ϵ" approximation of Iori et al., introducing explicit charges instead of dipolar Drude oscillators.

For the many body potential, we resorted to the so-called embedded-atom method (EAM) [62, 63], that provide a widely accepted, thoroughly tested and easy to use approach. To improve on the high dielectric constant approximation, we attributed a discrete charge variable to each metal atom. This discrete variable assumes the values $\{-1, 0, 1\}$ meaning that the corresponding atom has charge $-\delta$, 0 or $+\delta$. Atoms change their state of charge in a discontinuous way, and for this reason we replaced molecular dynamics with Monte Carlo. Changing the charge of atom requires a finite amount of energy, that depends on the local coordination of atoms. This energy is low for well coordinated metal atoms, and high for isolated metal atoms. Charge is neither created nor destroyed, but simply moved from one atom to its nearest neighbour, implying that each metal aggregate conserves its charge, that

in most cases is globally zero.

The development of the model requires the delicate tuning of the charging energy, and the precise definition of the rules to displace charge. Preliminary versions of the model provided encouraging results, since they show that metals screen any external field, while maintaining global neutrality, and confining charge at their surface. Work is in progress to produce a quantitative model able to successfully compete with GolP.

4.2.2 Definition of our force field

In the atomistic simulation of a molecular system, we need an accurate and reliable approximation for the system potential energy as a function of coordinates of the individual atoms.

This can be done most accurately using *ab-initio* method, but this is computationally demanding. Therefore, empirical force fields are used instead. Here, the zero level of the energy is represented by the molecular ground state energy. In a system with multiple molecules, this molecular ground state energy will be multiplied with the number of molecules. A change in the atom coordinates away from equilibrium results in a change in the energy that can be represented with bonded (intra-molecular) and non-bonded (inter-molecular) contributions, each usually modelled with fairly simple, analytical expressions.

The bonded contributions can consist of bond stretching, angle bending and improper torsion. The latter to reproduce the planarity of π-bonded groups. Non-bonded interactions can consist of short-range repulsion, medium-range dispersion and Coulomb interactions.

The force field is represented by a functional form in which the parameters can be found e.g. from *ab-initio* methods. Using the ground state geometry and vibrational frequencies from quantum chemistry, one can use this to specify the parameters used in the simple, analytical expressions for the intra- and inter-molecular interactions.

In this thesis, a somewhat reverse procedure has been followed; validating a force field model selected from the literature. The force field being used is adopted from the one by Tissen and Janssen [12], so instead we compare this force fields performance by comparing

it to results from *ab-initio* computations. These computations have been carried out using density functional theory (DFT), with the exchange-correlation functional by Perdew, Burke and Ernzerhof (PBE) [64], giving a semi-local approximation. Some computations were done using the B3LYP functional, as a comparison. Two different computer packages were used to compute the molecular properties with quantum chemistry; CPMD [65] and Gaussian 09 [66]. CPMD expands Kohn-Sham orbitals on a plane wave basis set, while Gaussian 09 is based on localised basis functions of the Cartesian Gaussian type.

Computations were carried out for an isolated Li_2CO_3 molecule. These computations were repeated for a single Na_2CO_3 molecule and a single K_2CO_3 molecule. For completeness, we included H_2CO_3, i.e., carbonic acid, in our computations. Once these were done, new computations were conducted where one cation was removed, resulting in MCO_3^{-1}, M being Li, Na, K or H. The energy of the single cation was also calculated, giving the dissociation energy. After that, the other cation was removed, resulting in a carbonate ion.

The results for the ground state geometry can be seen in Tables 4.3 and 4.4, while vibrational frequencies can be seen in Table 4.9. We define atomic charges following the electrostatic potential fitting (ESP) approach [67], i.e., determining the charge on each atom of a molecule or molecular ion in such a way to reproduce the electric field around the molecule. This was computed by *ab-initio* computations. In our case, *ab-initio* correspond to DFT-PBE. Computations have been carried out using CPMD and the result for the charges of Li_2CO_3 can be seen in Table 4.6.

Finding suitable force field parameters for this molecule poses some challenges, mainly due to the delocalisation of electrons in a carbonate ion. Since the bond length between carbon and oxygen will change dynamically, a force field dependent on the local coordination should be used in order to model this correctly.

As a first attempt, the carbonate ion is treated as a rigid unit with D_{3h} geometry where all the bonds and angles were kept constant. This caused a lot of problems, both in terms of a centre of mass drift and non-uniform heatfluxes in the homogeneous system.

Instead, we used flexible molecular units, where a harmonic potential is used for the

angles and improper torsions of carbonate, described by the following equations

$$V_{bending} = K_\theta(\theta - \theta_0)^2 \tag{4.2.11}$$

$$V_{improper} = K_\phi(\phi - \phi_0)^2 \tag{4.2.12}$$

where θ are bending angles and ϕ are torsional angles. The K_θ and K_ϕ parameters can be seen in Table 4.1. The parameters for the improper torsion is taken from Masia et al. [49], and the parameter for the angle bending is loosely based on the same source. The simulation results are not dependent upon these parameters, provided they are significantly large to keep CO_3^{2-} rigid-like.

Table 4.1: Force field parameters used to model the harmonic bonds, angles and improper torsions in CO_3^{2-}.

Parameter	value
K_θ [kcal mol^{-1} rad^{-2}]	100.0
K_ϕ [kcal mol^{-1} rad^{-2}]	45.0
θ_0 [degrees]	120.0
ϕ_0 [degrees]	180.0

The C−O bond length was constrained to 1.27 Å by use of the SHAKE algorithm [68], as proposed by Tissen and Janssen [12]. The accuracy tolerance of the SHAKE solution was set to 10^{-7}, as suggested by Ottochian et al. [29], as they experienced energy drift with the use of greater tolerances. For the interaction between atoms, a Born-Mayer-Huggins (BMH) were used together with a Coulomb term:

$$V_{BMH}(r_{ij}) = \frac{z_i z_j e^2}{r_{ij}} + b\left(1 + \frac{z_i}{n_i} + \frac{z_j}{n_j}\right)\exp[\alpha(\sigma_i + \sigma_j - r_{ij})] \tag{4.2.13}$$

where r_{ij} is the distance between atoms i and j, e is the electric unit of charge, z_i is the valence of atom i, σ_i can be interpreted as the ionic radius and n_i is the number of electrons in the outer shell of atom i. These parameters can be found in Table 4.2. The constant $b = 4.865$ kcal/mol determines the weight of the BMH interaction and $\alpha = 3.45$ Å^{-1} determines the

steepness.

Table 4.2: Force field parameters used to model Li_2CO_3, Na_2CO_3 and K_2CO_3 using eq. (4.2.13) [29].

Atom type	z [e]	n	σ [Å]
C	1.54	2.46	1.10
O	-1.18	7.18	1.33
Li	1.0	2.00	0.77
Na	1.0	8.00	1.07
K	1.0	8.00	1.39

In order to describe the long-range interactions, the Ewald method, see e.g. [15], was used with a relative error in forces of 10^{-4}. The cutoff for inter-molecular interactions was set to 10 Å, applied both to dispersion and to the real-space part of Ewald.

The reasoning for using this potential with these parameters, is because it has been studied by several persons, e.g. (from newest to oldest) Ottochian et al. [29], Koishi et al. [41] and Tissen and Janssen [12]. The study by Ottochian et al. was conducted no more than a year ago, giving a clear indication that there is currently no better model available on the market. Since the model has been thoroughly studied, most of its strengths and weaknesses have been documented, making it more suitable for new applications than a completely new model that has never been tested.

For the comparison between the force field and the *ab-initio* computation, a slight modification of the model had to be carried out. As the C−O bond lengths in our simulations are constrained, it is not able to give us the frequencies for these modes. Therefore a harmonic spring was used to model the C−O bonds, described by the following equation:

$$V_{stretching} = K_r(r - r_0)^2 \tag{4.2.14}$$

where $K_r = 500$ kcal mol^{-1} Å^{-2}, which is based on the values from the AMBER force field given in the paper by Masia et al. [49]

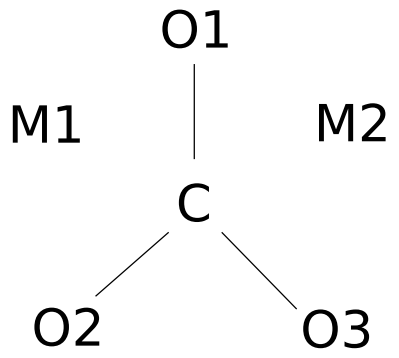

Figure 4.6: Schematic of M_2CO_3, where M is either Li, Na, K or H.

Since the model we used is based on Hartree-Fock, we carried out computations to see how well Hartree-Fock performs compared to density functional theory. We determined the ground state geometry for M_2CO_3, MCO_3^- and CO_3^{2-}, where M is either Li, Na, K or H. Two different functionals were used for the DFT computations, namely PBE and B3LYP, both of which are quite popular in literature. The ground state geometry for Li_2CO_3 found from the force field (FF) is also included. The bond lengths can be seen in Table 4.3, while the angles can be seen in Table 4.4. Some bond lengths and angles are left out of the tables due to symmetry, e.g. bond length C-O2 is equal to C-O3 and angle O1-C-O2 is equal to O1-C-O3. Therefore, bond length C-O3 and angle O1-C-O3 are not shown. The naming of the bonds and angles follows the schematic shown in Figure 4.6.

Table 4.3: Bond lengths in Å. M=Li,Na,K,H

Type	C-O1	C-O2	M1-O2	M1-O1
Li_2CO_3 (PBE)	1.38	1.28	1.82	1.82
Li_2CO_3 (B3LYP)	1.37	1.27	1.81	1.82
Li_2CO_3 (HF)	1.33	1.25	1.79	1.82
Li_2CO_3 (FF)	1.25	1.24	1.74	2.02
Na_2CO_3 (PBE)	1.37	1.29	2.15	2.18
Na_2CO_3 (B3LYP)	1.36	1.28	2.14	2.17
Na_2CO_3 (HF)	1.32	1.25	2.13	2.17
K_2CO_3 (PBE)	1.36	1.29	2.41	2.47
K_2CO_3 (B3LYP)	1.35	1.28	2.42	2.48
K_2CO_3 (HF)	1.31	1.26	2.44	2.51
H_2CO_3 (PBE)	1.21	1.35	0.97	2.32
H_2CO_3 (B3LYP)	1.20	1.34	0.97	2.32
H_2CO_3 (HF)	1.18	1.31	0.94	2.29
CO_3^{2-} (PBE)	1.32	1.32	-	-
CO_3^{2-} (B3LYP)	1.31	1.31	-	-
CO_3^{2-} (HF)	1.28	1.28	-	-

The bond lengths from the geometry optimization with PBE and B3LYP functional are close to each other, while HF deviates somewhat more from these values. In general, the bond lengths from B3LYP are shorter than PBE, and the ones from HF are even shorter. Unfortunately, to the best of our knowledge, no detailed experimental information with small enough errorbar is available to check the accuracy of these results. On the basis of experience, we expect the DFT-PBE results to be rather accurate.

Table 4.4: Angles in degrees. M=Li,Na,K,H

Type	O1-C-O2	O2-C-O3	M1-O2-C
Li_2CO_3 (PBE)	117	127	85
Li_2CO_3 (B3LYP)	116	127	85
Li_2CO_3 (HF)	116	127	86
Li_2CO_3 (FF)	114	132	96
Na_2CO_3 (PBE)	118	124	91
Na_2CO_3 (B3LYP)	118	124	91
Na_2CO_3 (HF)	118	124	92
K_2CO_3 (PBE)	118	123	95
K_2CO_3 (B3LYP)	118	124	96
K_2CO_3 (HF)	118	123	97
H_2CO_3 (PBE)	126	108	105
H_2CO_3 (B3LYP)	126	109	107
H_2CO_3 (HF)	125	110	108
CO_3^{2-} (PBE)	120	120	-
CO_3^{2-} (B3LYP)	120	120	-
CO_3^{2-} (HF)	120	120	-

It is worth noting that the average C-O bond length and average O-C-O angle does not differ much between M_2CO_3 and CO_3^{2-}, as shown in Table 4.5

Table 4.5: Average bond length in Å and average angles in degrees.

Type	C-O	O-C-O
Li_2CO_3 (PBE)	1.31	120
Li_2CO_3 (B3LYP)	1.30	120
Li_2CO_3 (HF)	1.27	120
CO_3^{2-} (PBE)	1.32	120
CO_3^{2-} (B3LYP)	1.31	120
CO_3^{2-} (HF)	1.28	120

It can be seen that the average bond lengths of C-O for Li_2CO_3 are only slightly shorter than for CO_3^{2-} within the same *ab-initio* method, and that the average bond angles of O-C-O are practically equal. This would mean it is not such a bad approximation to use the structure of the carbonate ion in simulation of alkali carbonate, in regards of average bond lengths and angles. It would also mean that treating C-O bond lengths as being independent

on the proximity of the cation should not give too large errors. Depending on the position of the cations, the C-O1, C-O2 or C-O3 will elongate and the other two will shorten. However, one can assume that the simulation is run long enough so that on average the cations spend an equal amount of time between each oxygen atom. This would mean that even if we enabled the possibility for the bond length to change according to the distance between the anion and the cation, the bond length between carbon and oxygen would be approximately equal on average.

The improper torsion angle between O1-C-O2-O3 was 180.0° and was 0.0° between O1-C-O2-M1 for all cases. This means that having a cation close to carbonate does not change the ground state geometry with respect to out-of-planarity; a fact that further strengthens the credibility of our model.

A comparison of the atomic charges for Li_2CO_3 computed from DFT-PBE and the ones used in our force field can be seen in Table 4.6

Table 4.6: Comparison of atomic charges from the force field and *ab-initio* for Li_2CO_3.

Type	z_C [e]	z_{O1} [e]	z_{O2} [e]	z_{Li} [e]
Li_2CO_3 (PBE)	1.343	-0.681	-1.149	0.818
Li_2CO_3 (FF)	1.54	-1.18	-1.18	1.0

Note the difference between the atomic charges on oxygen with a single bond and oxygen with a double bond for the DFT-PBE computation. This is not seen for the force field, as the carbonate ion is treated as an average with respect to the C−O bonds.

A comparison of the energy required to remove a cation in order to create an ion (here termed dissociation energy) is given for the different molecules and *ab-initio* methods in Table 4.7.

Table 4.7: Comparison of dissociation energies for different molecules and *ab-initio* methods.

Type	First dissociation energy [eV]	Second dissociation energy [eV]
Li_2CO_3 (PBE)	7.85	12.66
Li_2CO_3 (B3LYP)	7.91	12.73
Li_2CO_3 (HF)	7.97	12.78
Na_2CO_3 (PBE)	6.93	11.06
Na_2CO_3 (B3LYP)	7.02	11.03
Na_2CO_3 (HF)	7.07	10.94
K_2CO_3 (PBE)	6.20	10.16
K_2CO_3 (B3LYP)	6.29	10.00
K_2CO_3 (HF)	6.29	9.79
H_2CO_3 (PBE)	14.85	21.22
H_2CO_3 (B3LYP)	14.92	21.31
H_2CO_3 (HF)	15.28	21.68

The ionization energy decreases both for the first and second ionization as the size of the cation increases. This is reasonable, as the bond lengths shown in Table 4.3 between the cation and oxygen also increases, so the cation will be more loosely bound. Another observation is that the second dissociation energy is larger than the first dissociation energy for all cases, meaning that the single cation is more strongly bound, as expected.

In order to investigate the frequency modes and compare them, symmetry labels from the C_{2v} point group were used. The reason for doing this is because many of the modes have coupling between bond stretching and angle bending in the carbonate group, making it difficult to describe them with words alone. The character table for this point group is given in Table 4.8.

Table 4.8: Character table for C_{2v}

C_{2v}	E	C_2	σ_v (xz)	σ'_v(yz)
A_1	1	1	1	1
A_2	1	1	-1	-1
B_1	1	-1	1	-1
B_2	1	-1	-1	1

In Table 4.9, the frequency modes for the alkali carbonates can be seen, comparing the

DFT and force field results as well as comparing the frequency modes for Li_2CO_3, Na_2CO_3 and K_2CO_3 for the PBE functional.

Table 4.9: Vibrational frequencies in cm^{-1}

	Symmetry label	Li_2CO_3 (PBE)	Li_2CO_3 (FF)	Na_2CO_3 (PBE)	K_2CO_3 (PBE)
ν_1	B_2	1569	1688	1489	1473
ν_2	A_1	1264	1608	1243	1248
ν_3	A_1	937	876	942	960
ν_4	B_1	807	864	811	817
ν_5	B_2	770	681	705	675
ν_6	A_1	705	729	672	663
ν_7	B_2	579	626	362	292
ν_8	A_1	579	606	335	259
ν_9	B_2	516	245	359	289
ν_{10}	A_1	407	236	198	127
ν_{11}	B_1	171	176	109	80
ν_{12}	A_2	170	214	108	72

The frequencies from the force field was calculated by diagonalizing the Hessian matrix $\mathbf{H}$, which is a matrix containing the second order derivative of the energy with respect to Cartesian coordinates. This was done by displacing atoms from the ground state geometry by a small distance δ, so that the second order derivative could be calculated numerically according to the following scheme derived from Taylor expansion:

$$\frac{\partial^2 E}{\partial \alpha_i \beta_j} \approx \frac{1}{4\delta^2} \left[E(\alpha_i + \delta, \beta_j + \delta) - E(\alpha_i + \delta, \beta_j - \delta) - E(\alpha_i - \delta, \beta_j + \delta) + E(\alpha_i - \delta, \beta_j - \delta) \right] \tag{4.2.15}$$

where α and β are Cartesian coordinates, i.e. $\alpha, \beta \in \{x, y, z\}$, and i, j are the atoms. This square matrix can then be written in terms of a diagonal matrix $\mathbf{D}$ containing eigenvalues and a matrix of eigenvectors $\mathbf{P}$ such that $\mathbf{H} = \mathbf{PDP}^{-1}$. The eigenvalues given on the diagonal of $\mathbf{D}$ give the frequencies, while the eigenvectors in $\mathbf{P}$ give the modes. As shown in Table 4.9, these frequencies correspond decently with the ones from *ab-initio*, which agree with the ones found for Li_2CO_3 by Ramondo and Bencivenni [69].

Several observations are worth noting. First of all is the large separation between the

largest and second largest frequency in the *ab-initio* computation. As can be seen from Figure 4.7, the two highest frequency modes contains a coupling of bond stretching and angle bending in carbonate.

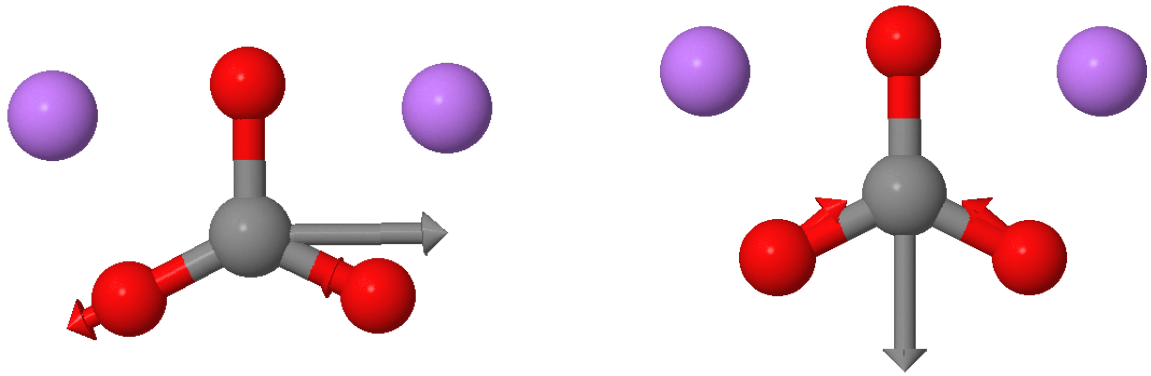

(a) $\nu_1 = 1569$ cm^{-1} (b) $\nu_2 = 1264$cm^{-1}

Figure 4.7: Frequency modes represented by arrows corresponding to the highest (a) and second highest (b) frequency for Li_2CO_3 computed with the PBE functional

Secondly the modes with large frequencies contain little or no vibration with respect to the cation. For example is the vibrational frequency from the *ab-initio* computation for the out-of-plane torsion of CO_3 within 10 cm^{-1} of each other for Li_2CO_3, Na_2CO_3 and K_2CO_3.

An important note: One has to bear in mind that many of the frequency modes has the same symmetry label, and these can be difficult to separate from each other. This means that e.g. ν_3 for Li_2CO_3 might correspond to ν_6 for K_2CO_3.

Non-homogeneous system

In the non-homogeneous system the Lennard-Jones (LJ) potential, given as

$$V_{LJ}(r_{ij}) = 4\epsilon_{ij}\left[\left(\frac{\sigma_{ij}}{r_{ij}}\right)^{12} - \left(\frac{\sigma_{ij}}{r_{ij}}\right)^{6}\right] \tag{4.2.16}$$

was used for the neutral wall particles, in which the parameters were taken from the GolP potential [61], presented in Table 4.10. The interaction between the neutral wall and confined

particles were modelled using the Lennard-Jones potential, with the parameters for Li, K, Na, C and O taken from the OPLS-AA (Optimized Potentials for Liquid Simulations-All Atom) force field [42], which can also be seen in Table 4.10.

Table 4.10: Parameters used to model the neutral wall and its interaction with the alkali carbonates

Atom type	σ [Å]	ϵ [kcal/mol]
Au	2.9	0.3137
C	3.75	0.105
O	2.96	0.21
Li	2.87	0.0005
Na	4.07	0.0005
K	5.17	0.0005

Whenever $i \neq j$, the Lorentz-Berthelot mixing rules were used:

$$\sigma_{ij} = \frac{\sigma_{ii} + \sigma_{jj}}{2} \tag{4.2.17}$$

$$\epsilon_{ij} = \sqrt{\epsilon_{ii}\epsilon_{jj}} \tag{4.2.18}$$

The reason why the LJ potential was chosen over the BMH potential for the interaction between the wall and the fluid was because of the desire to have an attractive and repulsive term in the potential, which is not feasible with the BMH potential since the wall particles are neutral

4.2.3 MD algorithm

The molecular dynamics package LAMMPS [70] (the 10 Aug 2015 version) was used to model the alkali carbonates. This is because of the requirement to have a parallel code, in order to run on multiple processors, speeding up the simulation manyfold. Simulations were done in the isothermal-isobaric (NPT), canonical (NVT) and microcanonical (NVE) ensemble; a description which can be found e.g. in the book by Frenkel and Smit [15]. For all ensembles, Nosé-Hoover style non-Hamiltonian equations of motions were time integrated.

The equations of motions used are those of Shinoda et al. [71], which combine the hydrostatic equations of Martyna et al. [72] with the strain energy proposed by Parrinello and Rahman [73]. The time integration scheme follows the time-reverisble measure-preserving Verlet derived by Tuckerman et al. [74].

In the homogeneous case, the isothermal-isobaric (NPT) ensemble was first used for equilibration. Here the temperature, pressure and number of particles are kept constant. To do this a Nosé-Hoover thermo- and barostat were used, which were achieved by adding dynamic variables which are coupled to the particle velocities and simulation domain dimensions. After finding the equilibrated density, the canonical (NVT) ensemble was used by disconnecting the barostat. Now the number of particles, volume and temperature are kept constant, with the density acquired from the previous step. This was done to get an equilibrated sample at this specific density.

After the equilibration the microcanonical (NVE) ensemble was used for production, where the number of particles, volume and energy were kept constant. From this run, the temperature, pressure and energy was outputted and the observables discussed in section 4.2.4 were computed.

In the non-homogeneous case, both the equilibration and production were done in the NVT ensemble.

4.2.4 Computation of observables

Radial distribution function

The radial distribution function (RDF), $g(r)$, between atom type i and j can be computed using the following equation [12]:

$$g_{ij}(r + \frac{1}{2}\delta r) = \frac{\Delta n_{ij}(r, r + \delta r)V}{4\pi(r + \frac{1}{2}\delta r)^2 \delta r N_i N_j} \tag{4.2.19}$$

where $\Delta n_{ij}(r, r + \delta r)$ is the number of atom pair i, j that can be found in the distance between r and δr. N_i and N_j is the number of atoms of type i and j, respectively, in the

simulation box of volume V. From the RDF, the running coordination numbers n_{ij} can be found [12]:

$$n_{ij}(r) = \frac{N_j}{V} \int_0^r g_{ij}(r') 4\pi r'^2 dr' \tag{4.2.20}$$

The coordination number of interest is usually found from the first coordination shell, where the integration lasts until g_{ij} has its first minima after the first peak, or until the second time g_{ij} reaches unity. In this thesis, the first criteria will be used.

Diffusion coefficient

There is mainly two ways of calculating the diffusion coefficient from a molecular dynamics simulation; from the velocity autocorrelation function (Green-Kubo) or from the mean square displacement (Einstein) of each specie. As discussed by Tuckerman [75], the velocity autocorrelation function has a long-time tail that is slow to converge, and it is also influenced by finite-size effects. Therefore, the latter approach will be used in this thesis. The mean square displacement (MSD) can be calculated from the particle trajectories outputted by the simulation. After an initial startup, the MSD should behave linearly with time as the particles are free to diffuse. For a d-dimensional system, the diffusion coefficient for specie i, D_i, is given by the Einstein relation [75]

$$D_i = \frac{1}{2d} \lim_{t \to \infty} \frac{d}{dt} \langle |\mathbf{r}(t) - \mathbf{r}(0)|^2 \rangle \tag{4.2.21}$$

where $\langle |\mathbf{r}(t) - \mathbf{r}(0)|^2 \rangle$ is the mean square displacement at time t. The brackets represents an ensemble average over the initial state. This can be compared with the literature value, e.g. from Janz and Bansal [76], to see if the system behaves like a liquid.

Electrical conductivity

The electric current density $\mathbf{j}$ is calculated each timestep as

$$\mathbf{j} = \frac{\sum_i^N z_i \mathbf{v}_i}{V} \tag{4.2.22}$$

where z_i is the charge of atom i, $\mathbf{v}_i$ is the velocity vector for atom i and N is the total number of atoms in the system. The electrical conductivity κ is computed using a Green-Kubo relation (see e.g. [15]):

$$\kappa = \frac{V}{3k_BT}\int_0^\infty \langle \mathbf{j}(t)\cdot\mathbf{j}(0)\rangle dt \tag{4.2.23}$$

where the brackets denote that an ensemble average is taken of the autocorrelation of the electric current density. Like diffusion, the electrical conductivity can be computed with an Einstein-like expression. We did not use this route, and for this reason we do not further discuss it. The electrical conductivity can also be estimated from the Nernst-Einstein (NE) relation [77]:

$$\kappa_{NE} = \frac{F^2}{RT}\frac{\rho}{M_w}(\nu_+ z_+^2 D_+ + \nu_- z_-^2 D_-) \tag{4.2.24}$$

where ν_+ and ν_- are the number of cations and anions per formula unit of electrolyte, respectively, z_+ and z_- are the valences of the cation and anion, respectively, and D_+ and D_- are the diffusion coefficients of the cation and anion, respectively. ρ is the simulated density of the salt, and M_w is the molar mass of the salt. F is Faraday's constant and R is the universal gas constant. This simple relation is based on the assumption that each ion diffuses independently from every other ion.

κ_{NE} can be multiplied by a correction factor $(1-\Delta)$ that takes into account the cross-correlation due to Coulomb interaction [29], giving the modified Nernst-Einstein equation:

$$\kappa'_{NE} = \kappa_{NE}(1-\Delta) \tag{4.2.25}$$

Thermal conductivity

The heat flux $\mathbf{J}_q$ is calculated each timestep as

$$\mathbf{J}_q = \frac{1}{V}\left[\sum_{i=1}^{N} e_i\mathbf{v}_i - \sum_{i=1}^{N}\mathbf{S}_i\mathbf{v}_i\right] \tag{4.2.26}$$

where e_i is the per-atom energy (kinetic and potential) and $\mathbf{S}_i$ is the per-atom stress tensor.

The thermal conductivity λ is computed using a Green-Kubo relation:

$$\lambda = \frac{V}{3k_B T^2} \int_0^\infty \langle \mathbf{J}_q(t) \cdot \mathbf{J}_q(0) \rangle dt \tag{4.2.27}$$

where an ensemble average is taken of the autocorrelation function of the heat flux.

Ideally, the thermal conductivity could also be calculated with a method based on non-equilibrium molecular dynamics (NEMD) as well. For example the thermostatting method proposed by Ikeshoji and Hafskjold [78], where two regions are set at different temperatures and the energy added and subtracted are monitored. This should be done in order to compare to the conductivity obtained by the Green-Kubo, since the autocorrelation is quite slow, meaning it has a very long "tail" that is integrated over. This requires that the simulation is run for a long time in order to get good enough statistics.

However, since we use the SHAKE algorithm, degrees-of-freedom are removed from the C−O bonds. LAMMPS correct for this in temperature and pressure computations, but not in the case of thermostatting regions. As a consequence LAMMPS will give wrong values for the energy needed to add and subtract to keep the target temperature. Therefore, it is not suitable for NEMD calculation of the thermal conductivity without modification of LAMMPS, which is why we only use GK in this thesis.

4.3 Results

4.3.1 Homogeneous system

In the homogeneous case, the system consisted of 512 M_2CO_3 molecules, where M is either Li, Na or K. This was deemed to be a large enough number for our simulations, since the boundary condition is of the periodic type. The pressure of the simulation was for all systems $P \approx 15$ kbar, in order to get a density close to the experimental density [79]. As described by Ottochian et al.: "It is worth to notice that the simulation pressure is not necessarily comparable to the real one since its absolute value depends on the chosen cutoffs for the

long- and short-range parts of the potential and if long tail corrections are considered or not. Thus, the only reasonable procedure to closely simulate the experimental system is to find the numerical pressure inducing the experimentally-obtained density." [29]

The initial configuration was run for 10^5 steps in the isothermal-isobaric (NPT) ensemble using a Nosé-Hoover thermo- and barostat with a timestep of 1 fs. The temperature was relaxed in a timespan of 100 time units (fs), while the pressure was relaxed in a timespan of 1000 time units. This was done in order to find the equilibrium density. After 100 ps, the barostat was disconnected and the simulation was run for another 10^5 steps using the same timestep at the canonical (NVT) ensemble, using the density acquired after the previous step, to get an equilibrated sample at this density.

Finally, a 5×10^6 steps production run was done in the microcanonical (NVE) ensemble. From this run, the temperature, pressure and energy were outputted every 100 steps. In addition, the positions and velocity vector of each atom were printed at these timesteps.

For most systems, the simulations were done for the temperatures 1200, 1300, 1400 and 1500 K. The reason for the large temperature was because we wanted to be well above the melting point of each sample, so we do not get any problem with crystallisation. The melting point, T_m, and boiling point, T_b, for each salt can be seen in table 4.11.

Table 4.11: Melting and boiling point for Li_2CO_3, Na_2CO_3 and K_2CO_3.

Molecule	T_m [K]	T_b [K]
Li_2CO_3	996 [80]	1615 [81]
Na_2CO_3	1124 [82]	1873 [83]
K_2CO_3	1164 [84]	Decomposes [84]

Structural properties

A plot of the radial distribution function for M_2CO_3, M being Li, Na or K, at $T = 1200$ K and $P = 15$ kbar can be seen in Figure 4.8, in which the distributions for C-C, C-M, O-M and M-M are plotted.

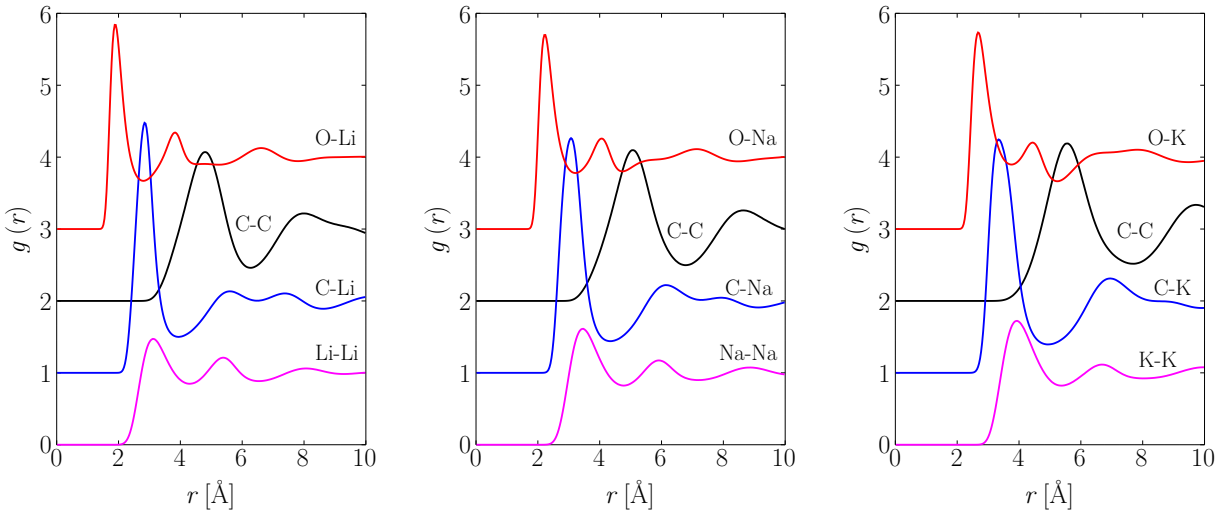

(a) Li_2CO_3 (b) Na_2CO_3 (c) K_2CO_3

Figure 4.8: Radial distribution function for Li_2CO_3 (a), Na_2CO_3 (b) and K_2CO_3 (c) at $T = 1200$ K, $P = 15$ kbar. All the curves, except the bottom one, have been shifted for readability.

The figures are in good agreement with the ones by Tissen and Janssen [12]. In order to see how many oxygen surround the cation, the coordination number of the first shell was found using equation (4.2.20). The result is given in Table 4.12.

Table 4.12: Coordination number between the cation and oxygen at different target temperatures.

Type	$T = 1200$ K	$T = 1300$ K	$T = 1400$ K	$T = 1500$ K
n_{OLi}	4.0	3.9	3.9	3.9
n_{CLi}	3.9	3.9	3.9	3.9
n_{ONa}	5.1	5.1	5.0	5.0
n_{CNa}	4.3	4.3	4.3	4.3
n_{OK}	6.2	6.2	6.1	6.0
n_{CK}	4.5	4.5	4.5	4.5

The coordination number for oxygen is found to be four in Li_2CO_3, meaning that each lithium ion is on average surrounded by four oxygen atoms. In K_2CO_3, however, the coordination number seems to be six. Perhaps more importantly, a four-fold coordination points to a tetrahedral local symmetry, while six points to an octahedral local geometry of oxygen

around the metal ion. The same coordination numbers were also found from simulation by Koishi et al. [41]. In their paper, they present figures showing the coordination number in lithium and potassium carbonate. These figures are presented in Figure 4.9.

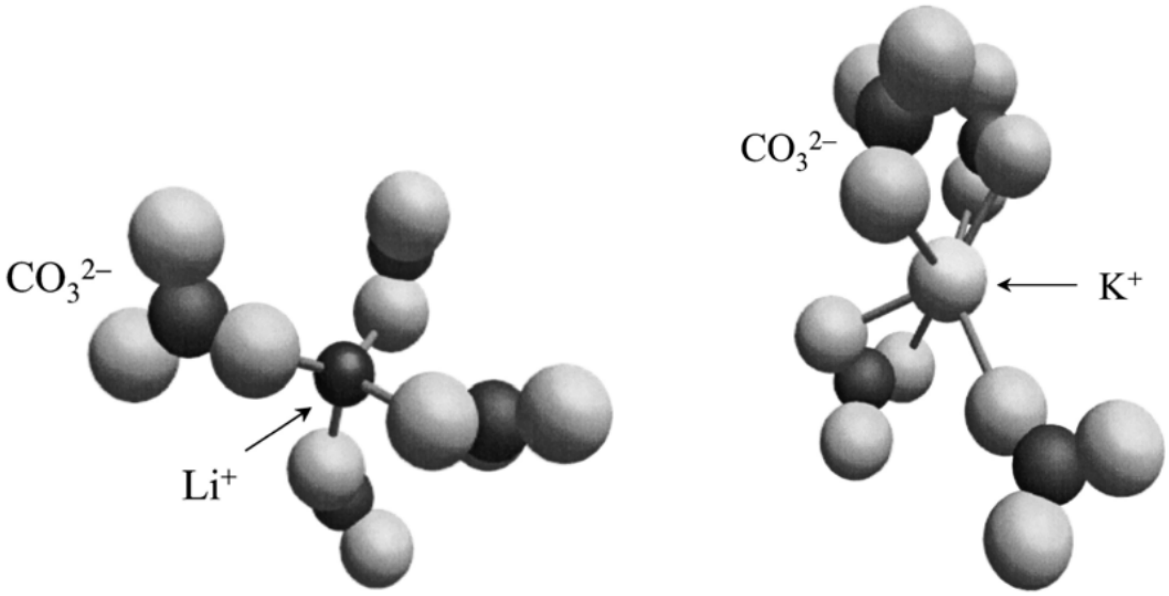

(a) Li_2CO_3 (b) K_2CO_3

Figure 4.9: Typical coordination in Li_2CO_3 (a) and K_2CO_3 (b) taken from Ref. [41].

The coordination number for oxygen in Na_2CO_3 appear to be five, which corresponds with the value from Wilding et al. [43] obtained from simulation at $T = 1750$ K. No simple geometry has five-fold coordination, and we expect that this number is the average of four-fold and six-fold coordinated metal sites.

As can be seen from Table 4.12, the coordination number changes very little with temperature in the temperature range between 1200 and 1500 K. This means that the cation environment with respect to oxygen changes very little over this range. A drastic change could mean that the fluid starts to crystallise, which gives reason to believe that crystallisation does not occur even at the lowest temperature of $T = 1200$ K, at least during the short time covered by our simulations.

From the coordination number there is reason to believe that each metal ion is surrounded

by four carbonate ions for Li_2CO_3. The coordination number for carbon increases a bit for Na_2CO_3 and K_2CO_3, but this increase is less than the increase in coordination number for oxygen. This would mean that around the same number of carbonate ions surround each cation, while for the heavier cations the carbonate ions are oriented so that more oxygens are within the first coordination shell. This can be explained as the heavier cations are larger, giving more surface area and therefore more space for the oxygens around it.

Structure factor

In order to be able to compare with experiments; we calculated from the trajectory the number-number structure factor $S_{NN}(k)$ as a function of wavenumber k. The result for Li_2CO_3 and Na_2CO_3 can be seen in Figure 4.10.

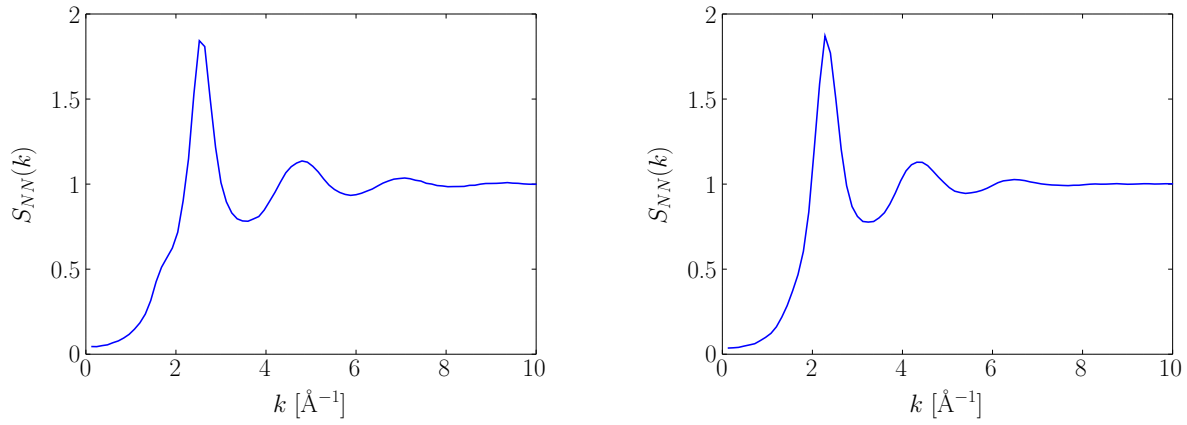

(a) Li_2CO_3 (b) Na_2CO_3

Figure 4.10: Number structure factor as a function of wavenumber for Li_2CO_3 (a) and Na_2CO_3 (b) at $T = 1200$ K, $P = 15$ kbar.

Several observations are worth noting. As shown by Hansen and McDonald [13], the isothermal compressibility χ_T is proportional to the value of the number-number structure factor as k goes to 0, i.e.

$$\lim_{k \to 0} S_{NN}(k) = \rho k_B T \chi_T \tag{4.3.1}$$

where k_B is Boltzmann's constant and ρ is the density. In our case, it can be seen that the compressibility is close to zero. This agrees with the fact that we are close to the triple point in our simulations.

The shoulder at $k \sim 1.8$ Å^{-1} apparent in the lithium S_{NN} and absent in the Na_2CO_3 case is an important feature.

If one is to compare with the literature, e.g. the neutron scattering experiments by Kohara et al. [45], one would find the highest peak for Li_2CO_3 at 1013 K to be ~ 3 and located around $k = 2$ Å^{-1}, while in our case the peak is below 2 and located around $k = 2.5$ Å^{-1}. The difference is likely to be due to the different temperatures of the samples. Still, as explained in section 4.1, getting accurate results from neutron scattering on other elements than hydrogen is difficult, so these values have sizeable error bars.

Ohata et al. [85] calculates the structure factors from denstiy functional theory (DFT) computation for a Li_2CO_3 tetramer. The values from this paper are very similar to the ones by Kohara et al. However, calculating the structure factor from the periodic replication of as little as four molecules is not very accurate, so this result is to be taken with some skepticism.

The charge structure factor $S_{ZZ}(k)$ was also calculated as a function of k for the same systems, and can be seen in Figure 4.11.

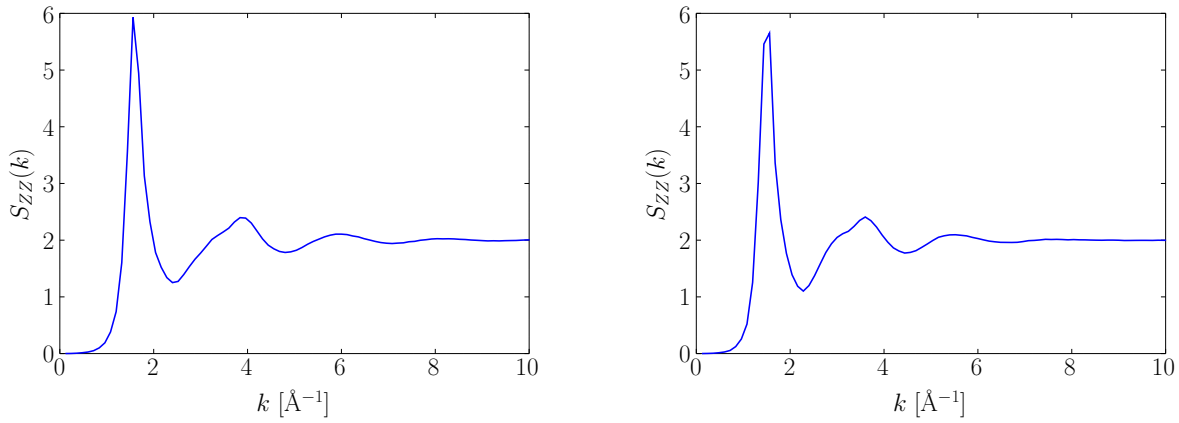

(a) Li_2CO_3 (b) Na_2CO_3

Figure 4.11: Charge structure factor as a function of wavenumber for Li_2CO_3 (a) and Na_2CO_3 (b) at $T = 1200$ K, $P = 15$ kbar.

Comparing this figure to Figure 4.10, one can observe that the peak for S_{ZZ} is higher than for S_{NN}. It is worth noting that in ionic liquids, charges are more ordered than density [13].

Transport properties

In Figure 4.12, the mean square displacement for Li_2CO_3 at $T = 1200$ K and $P = 15$ kbar is shown for up to 1 ns.

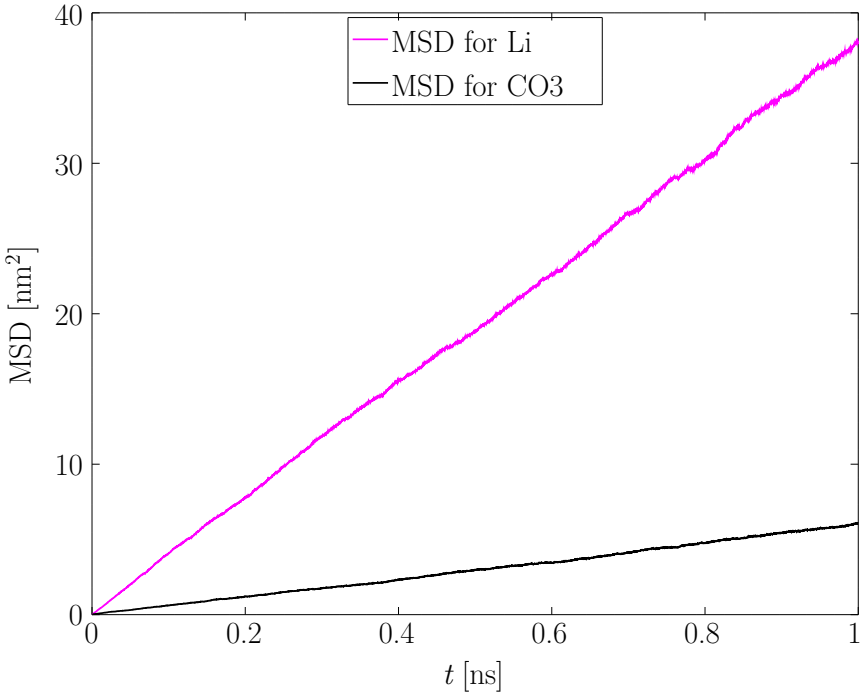

Figure 4.12: Mean square displacement for Li_2CO_3 at $T = 1200$ K, $P = 15$ kbar.

As can be seen, the MSD is quite linear for both the cation and anion, giving reason to believe that the system is in a liquid state and has not crystallised. If this had been the case, the MSD would have reached a plateau as the ions would be confined to their lattice positions.

In Table 4.13, the computed transport properties for Li_2CO_3 can be seen.

Table 4.13: Transport properties for Li_2CO_3.

T [K]	ρ [g/cm^3]	λ [W m^{-1}K^{-1}]	κ [S/cm]	κ_{NE} [S/cm]	D_{Li} [cm^2/s]	D_{CO_3} [cm^2/s]
1207	1.609	3.74 ± 0.10	4.17 ± 0.13	3.31	6.3×10^{-5}	9.4×10^{-6}
1295	1.577	3.58 ± 0.15	4.64 ± 0.17	3.91	8.0×10^{-5}	1.3×10^{-5}
1406	1.572	3.69 ± 0.10	5.6 ± 0.2	4.43	9.8×10^{-5}	1.7×10^{-5}
1492	1.540	3.73 ± 0.14	5.6 ± 0.2	5.16	1.2×10^{-4}	2.3×10^{-5}

From Janz and Lorenz [79], the electrical conductivity at $T = 1118$ K is $\kappa = 4.959$ S/cm. This is the highest temperature where they did the measurements for Li_2CO_3. Since κ has

a positive correlation with respect to temperature, both in my simulations and in the measurements by Janz and Lorenz, κ at $T \approx 1200$ K should be higher than the value Janz and Lorenz found at $T = 1118$ K. Ottochian et al., which also uses the force field by Janssen and Tissen [37], uses a scaling factor of ~ 1.7 on the electrical conductivity to better reproduce the experimental values. In the model made by Janssen and Tissen, the Hartree-Fock (HF) method was used, which does not reproduce the interaction energy correctly, due to an unprecise description of the electronic correlation [29]. Ottochian et al. also comment on that a transfer from a quantum mechanical model to a classical model often produces a greater activation energy E_a, and also that a steeper energy profile can explain the need of this scaling factor.

The literature values for the thermal conductivity λ are scarce and with large error, due to the difficulty of measuring this property accurately at temperatures exceeding 10^3 K, as discussed by Nunes et al. [86]. This makes simulation particularly useful. Gillis et al. [87] presents the thermal conductivity of molten Li_2CO_3 measured using forced Rayleigh scattering with a CO_2 laser. In the temperature region 1070-1355 K, λ is more or less constant ≈ 1 W m^{-1} K^{-1}. However, the accuracy of these measurements are $\sim 20\%$. If there is a temperature dependence, it is smaller than this error bar. The lack of temperature dependence can also be seen with my results, but my values are larger by a factor $\sim$ 3-4.

However, in Ref. [87] the work by Egorov and Revyakin is presented, where the steady state concentric cylinder method was used to find the thermal conductivity for molten Li_2CO_3. Here, $\lambda \approx 2$ W m^{-1} K^{-1} at 1000 K and $\lambda \approx 3$ W m^{-1} K^{-1} at 1300 K. However, Gills et al. believes that the Rayleigh scattering technique is superior when it comes to measurement of thermal diffusivity of high temperature molten salts, so the values from that method can be believed to be most accurate.

Table 4.14: Transport properties for Na_2CO_3.

T [K]	ρ [g/cm^3]	λ [W m^{-1}K^{-1}]	κ [S/cm]	κ_{NE} [S/cm]	D_{Na} [cm^2/s]	D_{CO_3} [cm^2/s]
1192	1.937	0.94 ± 0.03	2.24 ± 0.08	2.03	4.0×10^{-5}	9.8×10^{-6}
1320	1.916	0.93 ± 0.03	2.85 ± 0.11	2.35	5.1×10^{-5}	1.3×10^{-5}
1390	1.884	0.95 ± 0.03	2.90 ± 0.16	2.66	5.9×10^{-5}	1.7×10^{-5}
1494	1.866	0.93 ± 0.03	3.31 ± 0.13	2.99	7.2×10^{-5}	2.1×10^{-5}

The diffusion coefficient for the cation is fairly similar to the values obtained by simulation from Ottochian et al. However, this is not the case when compared to experiments. The diffusion coefficients found from our simulations are the same order of magnitude, but smaller than diffusion coefficients obtained from tracer-diffusion by Spedding and Mills [88].

Tissen and Janssen [12] suggest that the lack of polarisability is one of the reasons for the slower diffusion. However, Wilding et al. [43] uses the JT model with a harmonic spring instead of a rigid bond between carbon and oxygen for Na_2CO_3. They show that a stiffening of the intramolecular bonds results in a systematically smaller diffusion coefficient for the sodium ion. Since in our case the bonds are forced to be at the equilibrium length, that might explain the smaller diffusion coefficient observed for the cation.

Numes et al. estimate that at 1173 K, $\lambda = 0.822$ W m^{-1} K^{-1} for Na_2CO_3, but discuss that the difference between different authors can be as large as 50%. Therefore, the values I get for the thermal conductivity might very well be correct for Na_2CO_3.

Table 4.15: Transport properties K_2CO_3.

T [K]	ρ [g/cm^3]	λ [W m^{-1} K^{-1}]	κ [S/cm]	κ_{NE} [S/cm]	D_K [cm^2/s]	D_{CO_3} [cm^2/s]
1191	1.836	0.98 ± 0.04	1.24 ± 0.07	1.06	2.7×10^{-5}	7.9×10^{-6}
1302	1.835	0.84 ± 0.04	1.35 ± 0.06	1.29	3.5×10^{-5}	1.1×10^{-5}
1397	1.808	0.91 ± 0.04	1.61 ± 0.06	1.49	4.3×10^{-5}	1.4×10^{-5}
1494	1.766	0.94 ± 0.03	2.17 ± 0.06	1.77	5.4×10^{-5}	1.9×10^{-5}

The electrical conductivity can be seen to decrease as the cation goes down the period

of the alkali metals. This can also be seen in the measurements by Janz and Lorenz [79].

Thermal conductivity for pure molten K_2CO_3 is, as of this time, lacking. However, Zhang and Fujii [89] reports thermal conductivity for a 70/30 mol% mixture of molten Li_2CO_3−K_2CO_3. At $T = 922$ K, $\lambda = 0.829$ W m^{-1}K^{-1}. Therefore, it is reasonable that the values I get for the thermal conductivity of pure molten K_2CO_3 are within the correct order of magnitude.

It is worth noting that the electrical conductivity we estimated by the Nernst-Einstein equation, eq. (4.2.24), is lower than the one computed with the Green-Kubo relation, eq. (4.2.23), for all systems at all temperatures. In order to get the GK values by the modified Nernst-Einstein relation, eq. (4.2.25), Δ would have to be around -0.2. However, Δ is expected to be positive, and in alkali halides it has a value of ~ 0.26 [29]. As Hansen and McDonald explain [13]: "The positive value of Δ corresponds physically to the fact that motion in the same direction by a pair of oppositely charged ions contributes to self-diffusion but not to electrical conduction." However, it is not required that Δ has to be positive. Armstrong and Ballone [90] have shown by simulation that for simple 2:1 ionic liquids, Δ can be negative. As they also mention, negative values for Δ has been previously reported for molten salts close to their triple point [91, 92, 93]. The explanation could be due to "out of phase" correlation, similar to backflow in many-electronic systems [94].

Still, if one is to calculate Δ from the experimental data for Na_2CO_3 (taking the values for diffusion coefficient by Spedding and Mills [88] and the density and electrical conductivity by Janz and Lorenz [79]), one would find that $\Delta \sim 0.3$. The explanation why in our case we found that Δ is negative could be because of the underestimation of the diffusion coefficients, especially D_{CO3}. $z_- = -2$ for the carbonate ion, meaning that a small change in D_{CO3} will have a large impact on κ_{NE}, since the valences are squared in equation (4.2.24).

4.3.2 Non-homogeneous system

For the non-homogeneous system, most of the simulations were done using 2048 M_2CO_3 molecules. The reason for this "large" number of molecules is because of the need to have a bulk phase in the fluid that is far enough away from the wall, so that a clear distinction between the interface and the bulk can be made. One could instead decrease the cross-sectional area in order to get a longer box, but then edge-effects becomes more prominent, which is undesirable. The area of each wall in the case of 2048 molecules was 36.047 $\times$ 36.7038 Å^2. Test simulations were also done for Li_2CO_3 at $T = 1300$ K in which the system size were doubled and quadrupled by increasing the number of particles and periodicity in y-direction, hence 4096 molecules in a box with cross-sectional area of 36.047 $\times$ 73.41 Å^2 and 8192 molecules when the cross-sectional area of the wall were 36.047 $\times$ 146.82 Å^2, to see how the results would be affected by this. In theory, increasing the system size should not affect the results.

The length of the box in z-direction, L_z, was chosen so that the pressure on the particles confined between the walls would be close to the pressure in the homogeneous case. The spring constant used in the tethering of the wall atoms was set to $K_{spring} = 50$ kcal mol^{-1} Å^{-2}. The anchor position in z-direction for each wall was 8 Å away from the end of the simulation box. The reason for this number is because at lower values the walls becomes closer to each other due to periodicity, and it is desirable to have them far enough apart so that the particles do not interact with those on the other side of the wall. However, an anchor point too far from the end of the box would result in much empty space, which we "pay" for in computational time due to the computation of the long-range interactions (partly) in reciprocal space. Therefore, 8 Å was chosen as a good tradeoff between not having too much empty space and having a large enough distance between the walls.

The simulation was done with a timestep of 1 fs in the NVT-ensemble with a Nosé-Hoover thermostat. The relaxation time for the temperature was the same as in the homogeneous case, i.e. 100 time units (fs). For each system, the simulation was done in 10 stages, each

consisting of 10^5 steps, resulting in 10^6 steps in total (1 ns). Some of these stages were used for equilibration. When the system appeared to be equilibrated, the rest of the stages were used for production. In Figure 4.13, the density profile for anions, cations and neutral particles can be seen for Li_2CO_3 at 1300 K.

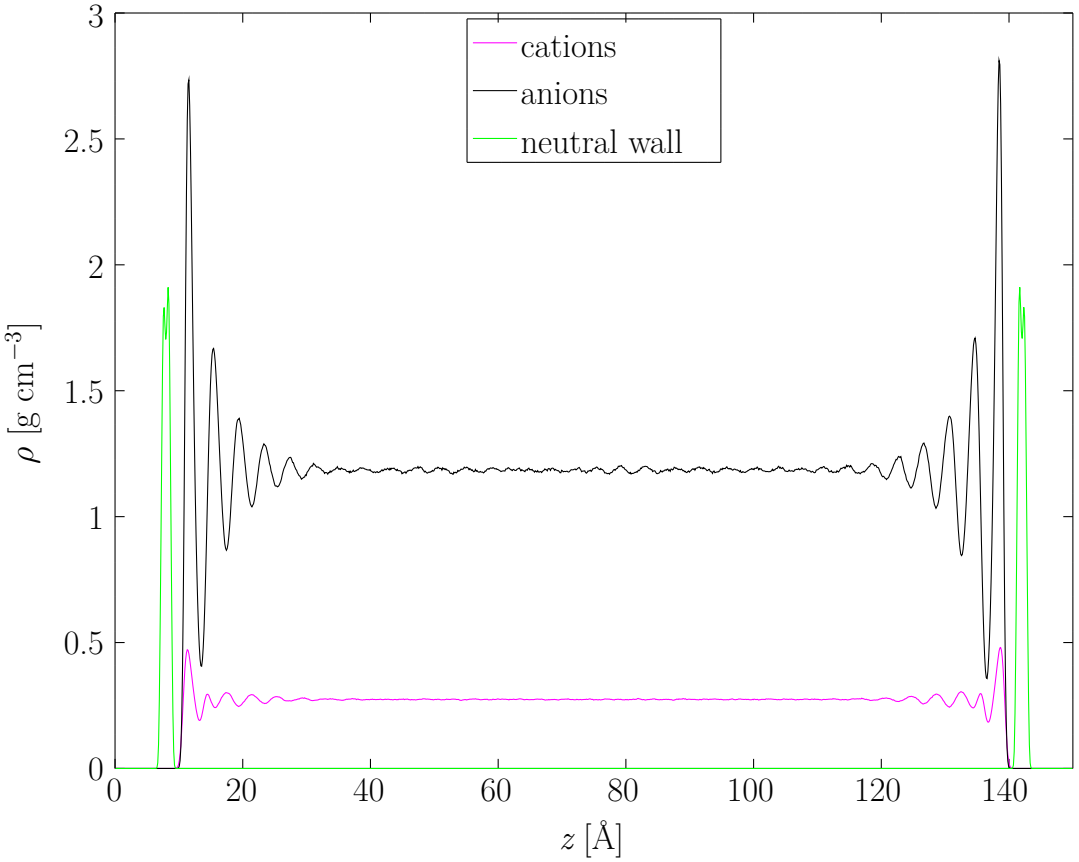

Figure 4.13: Density profile for anions, cations and neutral particles from the simulation of Li_2CO_3 confined between two planar neutral walls at 1300 K.

One of the goals of the simulations is to investigate the electrostatic double layer (EDL). From the charge density profile of Li_2CO_3 in Figure 4.14, a positive peak can be seen close to each wall.

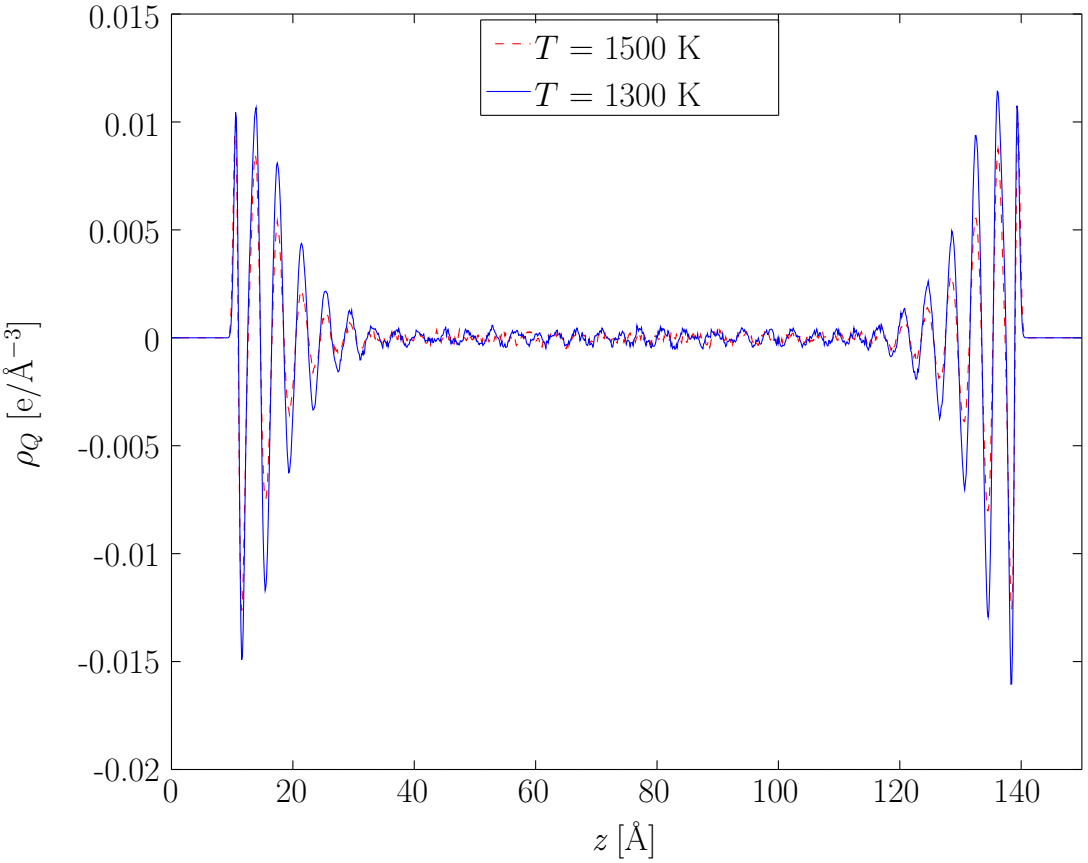

Figure 4.14: Charge density profile for Li_2CO_3 confined between two planar neutral walls. Full line, blue: $T = 1300$ K. Dashed line, red: $T = 1500$ K.

Since the lithium ion is smaller than the carbonate ion, it makes sense that these ions will dominate the region closest to the wall. The next layer is negative, implying a layer of anions. However, this layering continues for several more layers, which is different from what is seen in the idealised model. Also, the charge density oscillates a bit in the bulk, while for rigid ion particles it was more or less constant equal to zero. One could think this might be due to crystallisation. The system might be liquid-like in the homogeneous case, but with the introduction of a wall, crystallisation is a possibility. As the melting point of the model has not been found in this or previous studies, it is difficult to dismiss that the system might be in a metastable phase. Therefore, an analysis of the mean square displacement in the direction parallel to the wall was carried out. It was found that the MSD still increases

linearly with time in x- and y-direction, meaning that it behaves like a liquid and has not crystallised.

As can be seen from Figure 4.14, the oscillations are smaller for the high temperature case than for the low. This is in agreement with Figure 3.4 from the idealised model. However, in the non-homogeneous simulations of Li_2CO_3, the distance between the wall does not change when the temperature changes, meaning that the pressure will be higher at 1500 K compared to 1300 K, as shown in Table 4.16. Nevertheless, as shown later in Figure 4.16, a decrease in pressure while keeping the temperature constant (i.e. by expanding the distance between the walls) will cause a decrease of the amplitude of the charge density profile. This means that if the simulation at 1500 K were done at the same pressure as the simulation at 1300 K, the charge density profile in the high temperature case would have even less oscillation than shown in Figure 4.14.

A short simulation was also done with $LiNaCO_3$, to see how the lithium ions position themselves relatively to the sodium ions. The simulation started from an uniformly distributed sample. As can be seen from the difference in number density in Figure 4.15, the lithium ions are closer to the wall than the sodium ions. This is to be expected, as the lithium ions are smaller. Apart from this adsorbed layer the figure shows a wide-amplitude, long wavelength fluctuation of the Li^+ and Na^+ relative composition, hinting at an incipient segregation of Li_2CO_3 and Na_2CO_3 phases.

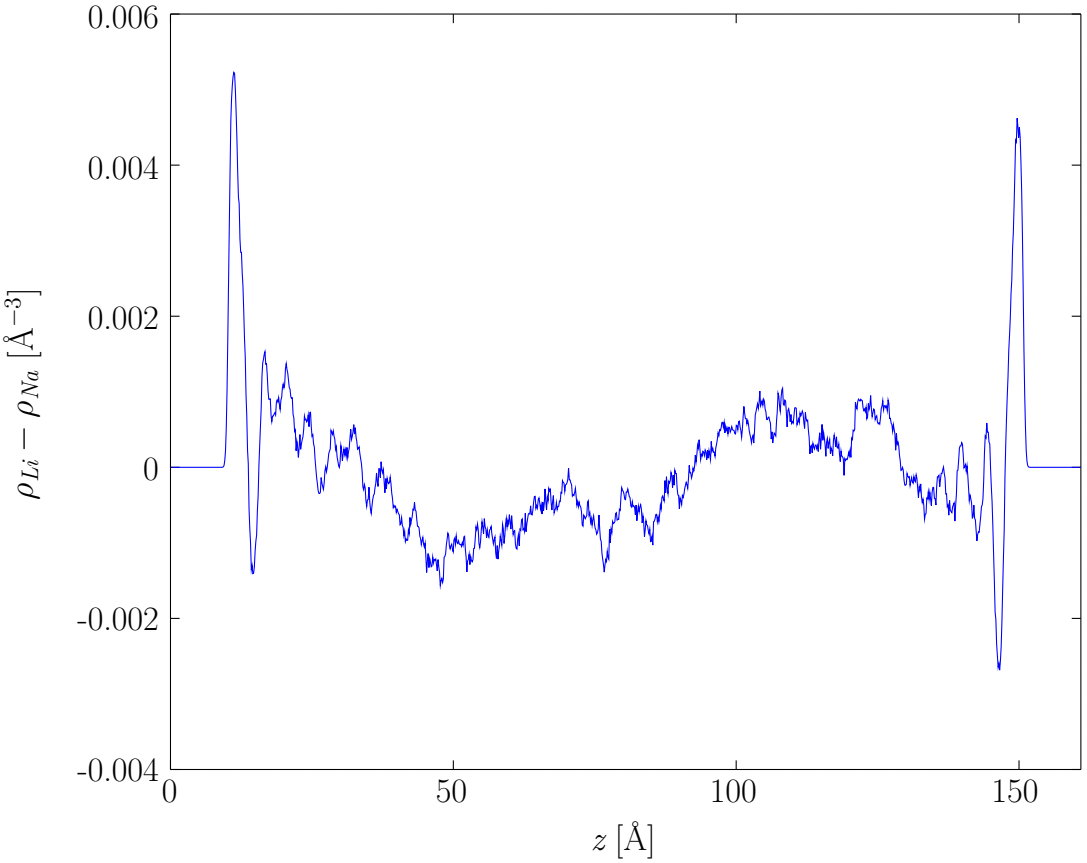

Figure 4.15: Difference in number density for lithium and sodium in $LiNaCO_3$.

An investigation was also done regarding the pressure dependence of the charge density profile, since the simulations were done at quite large pressures (order of 10^4 bar). In addition, the simulations of the non-homogeneous systems were not done at the same pressure, but at pressures shown in Table 4.16. This is due to the inaccessibility of the NPT ensemble in our simulations, since we have a wall fixed to specific anchor points given in the beginning of the simulation.

Table 4.16: Average of the simulated pressure.

System	P (1300 K) [kbar]	P (1400 K) [kbar]	P (1500 K) [kbar]
Li_2CO_3	11.0	13.7	16.3
Li_2CO_3 (area $\times$ 2)	11.0	-	-
Li_2CO_3 (area $\times$ 4)	11.0	-	-
$LiNaCO_3$	13.0	-	-
Na_2CO_3	18.2	18.6	-
K_2CO_3	17.9	14.2	-

In Figure 4.16, the comparison for the charge density profile of Li_2CO_3 at $T = 1300$ K at two different pressures can be seen. The high pressure is around 11 kbar and the low pressure is approximately 7 kbar. As can be seen, the profiles have the same shape, but the oscillations are a bit larger in the high pressure case compared to the lower, as can be expected.

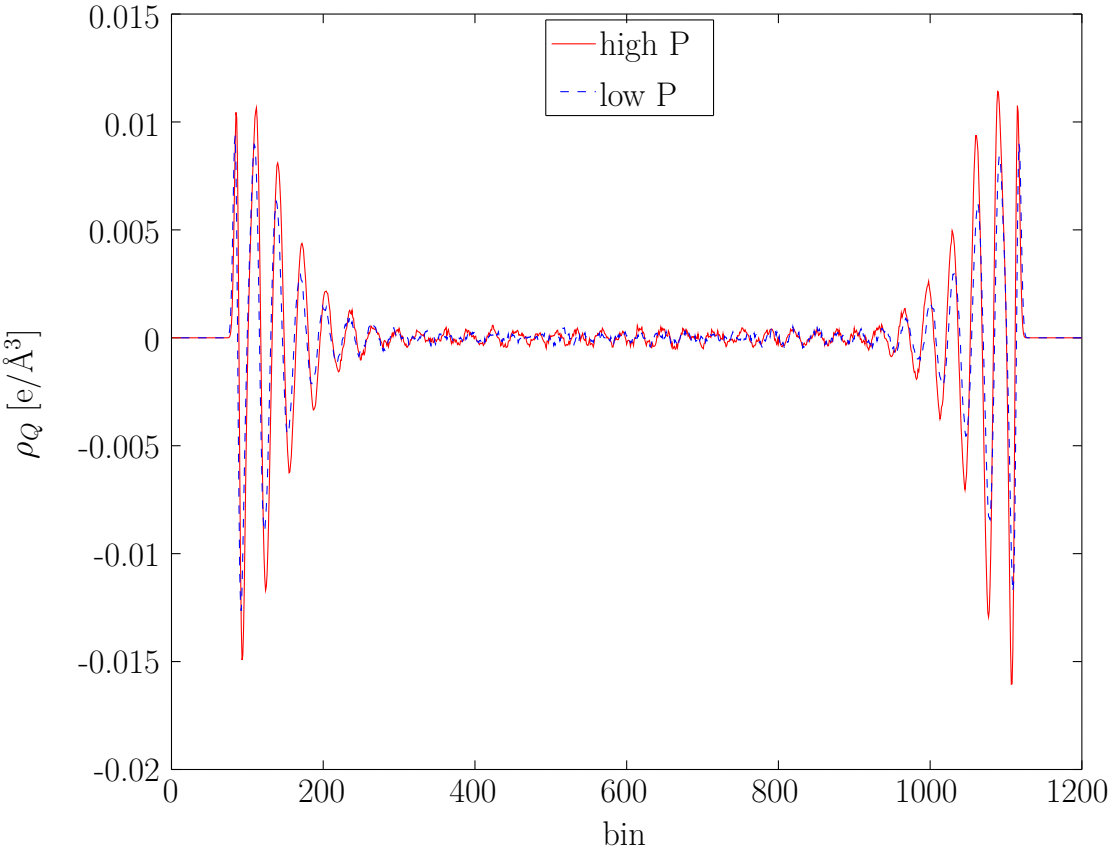

Figure 4.16: Charge density profile for Li_2CO_3 at $T = 1300$ K for $P \approx 7$ kbar (dashed line, blue) and $P \approx 11$ kbar (full line, red).

The dipole of each interface, D_{left} and D_{right}, were calculated from the charge density, ρ_Q, by the use of the following equations:

$$D_{left} = \int_{-L_z/2}^{0} z\rho_Q(z)dz \tag{4.3.2}$$

$$D_{right} = \int_{0}^{L_z/2} z\rho_Q(z)dz \tag{4.3.3}$$

Given that the system is at equilibrium, these two values should be equal to each other. Small deviations due to statistical errors, however, might occur.

As described previously, the simulation was done in stages. Each stage consisted of 10^5 steps, i.e. 0.1 ns. The first two stages were used for equilibration. The remaining 8 stages

was divided into 4 blocks, e.g. stage 3 and 4 becomes one block, 5 and 6 another one and so on. The density profile was averaged for each block.

To get the dipole, for each block an average was taken of $|D_{left}|$ and $|D_{right}|$. Thus for each system, four values was acquired for the dipole. These were averaged to give the values seen in Table 4.17. The error bar was computed as 2 times the standard deviation of the four values and then divided by $\sqrt{N}$, where N is the number of blocks.

The simulation of Li_2CO_3 at 1300 K and 1500 K where run up to 1.4 ns, meaning six blocks were used for production instead of four.

Table 4.17: Interfacial dipole at different temepratures for different systems.

System	D (1300 K) [D/nm^2]	D (1400 K) [D/nm^2]	D (1500 K) [D/nm^2]
Li_2CO_3	2.56 ± 0.07	2.66 ± 0.08	2.73 ± 0.08
Li_2CO_3 (area × 2)	2.69 ± 0.06	-	-
Li_2CO_3 (area × 4)	2.72 ± 0.05	-	-
$LiNaCO_3$	2.56 ± 0.09	-	-
Na_2CO_3	2.39 ± 0.12	2.42 ± 0.06	-
K_2CO_3	1.77 ± 0.06	1.84 ± 0.06	-

The trend seems to be that the dipole increases with increasing size asymmetry, as predicted by the idealised model. However, this is not conclusive in all cases, e.g. from Li to Na at 1300 K, due to the error bar. Still, at 1400 K, the error bar is sufficiently low that there is a noticeably change in the dipole from Li_2CO_3 to Na_2CO_3. One can therefore conclude that in general, the dipole becomes smaller as the size of the cation becomes more similar to the size of the anion.

It also seems that the dipole increases with temperature, but this is not conclusive for all systems due to the fact that the error bar is larger than this increase. However, in the case of the dipole for Li_2CO_3 at 1300 K vs. 1500 K, the error bar is sufficiently low that there is strong reason to believe the dipole increases with temperature. This was also predicted by the idealised model in Figure 3.5, giving credibility to this observation.

The information from this simulation is valuable in order to give an estimate of the simulation time required to get a signal beyond the error bar of the Seebeck coefficient when

doing non-equilibrium simulations in which the two walls are at different temperatures. In the experiments by Børset et al. [26], the temperature difference between the electrodes were smaller than 20 K in order to avoid temperature corrections in the Seebeck coefficient. Assuming the blocks of 2×10^5 steps are independent enough from each other to neglect the correction due to autocorrelation time, the error bar decreases by a factor $1/\sqrt{N}$. This means that quadrupling the simulation time will only halve the error bar. This would mean that in general, longer simulation times are required if the temperature gradient is low compared to when it is high. Still, with a longer simulation, e.g. close to 1 ms, which is feasible with today's technology, the error bar could be small enough to give a reasonable estimate of the Seebeck coefficient even with a relatively low temperature gradient.

4.4 Summary and outlook concerning alkali carbonates

Equilibrium molecular dynamics simulations have been carried out for an alkali carbonate model. The simulations were done of homogeneous samples of the alkali carbonates Li_2CO_3, Na_2CO_3 or K_2CO_3. Simulations were also done of these molecules confined between two parallel walls made of neutral particles, whose interaction with the fluid ions is the same for the two walls. All particles follow Newton's equations of motion.

From the homogeneous systems, structural properties like the structure factor and radial distribution function were computed, in addition to transport properties like diffusion coefficient, thermal and electrical conductivity.

The simulations of the heterogeneous systems provides a microscopic view of electrification at a solid/liquid interface. We explore, in particular, the dependence of the dipole at each interface for the different alkali carbonates. The temperature dependence $D(T)$ of the interfacial dipole was computed. There is reason to believe that this property increases with temperature, but because of the large errorbar our results are not conclusive. Longer simulations would be required to run in order for this to be said with more certainty. Or the

three carbonates tested, Li_2CO_3 was found to have the highest interfacial dipole. This was also the salt with the highest anion/cation size-asymmtry tested.

It is clear that while the model by Janssen and Tissen is able to predict structural characteristics and give a reasonable estimate of transport properties, there is still room for improvement. From our *ab-initio* computation, a new force field can be designed which is based on more accurate quantum chemical methods.

Our preliminary computations of alkali carbonates between planar walls shows the possibility to get an estimate of the Seebeck effect using simulation times feasible with today's technology. Before extensive and expensive computations are to be done, however, a better model for the wall should be developed. This is currenctly underway, mainly in the form of including image charges, using a many-body potential for the metal electrode [95] and using Monte Carlo to account for the non-Hamiltonian dynamic of the atomic charges.

Chapter 5

Conclusion

My thesis is devoted to the computational investigation of the microscopic mechanisms underlying the so-called Seebeck effect in ionic, and thus electrically conducting, classical fluids. These fluids usually consists of inorganic and organic molten salts, or of electrolyte solutions.

The Seebeck effect, in turn, consists of the onset of an electrostatic potential difference across a conducting sample joining two regions at different temperatures, T_L and T_R (L and R for left and right, respectively), and thus subject to a temperature gradient. The electrostatic potential difference $\Delta\phi$ is proportional to the temperature gradient and to the length of the sample, or, equivalently, to the temperature difference $T_L - T_R$. The ratio:

$$\alpha_S = \frac{\Delta\phi}{T_L - T_R}$$

at zero electric current is the so-called Seebeck coefficient, and summarises all the material-specific and microscopic properties of the sample.

Thermodynamics and statistical mechanics considerations show that the Seebeck effect is intimately related to entropy and its transformations in the sample. For this reason, of all conducting materials, including metals and doped semiconductors, we focus our analysis on ionic fluids, since we expect entropy to be large for these systems, possibly leading to large Seebeck coefficients. This expectation is borne out by the results of recent experiments, showing particularly high Seebeck coefficients for inorganic molten salts [26], and especially for organic ionic compounds that are liquid at room temperature [6]. The applied interest of these observations are apparent, because efficient devices based on the Seebeck effect could

contribute a significant amount of electric power exploiting waste heat made available at relatively low temperature by natural sources (geothermic, for instance) and by industrial processes.

In my thesis I used molecular dynamics simulation based on idealised or empirical force fields to estimate the Seebeck coefficient of classical fluids, considering both a very idealised model of isotropic rigid ions, as well as chemically detailed models of molecular ionic liquids. In these simulations, confining electrodes are described in terms of a few layers of isotropic neutral particles, tethered to fixed positions on a regular hexagonal lattice by harmonic springs whose spring constant is meant to reproduce the elastic properties of a solid surface.

In the case of the idealised model, the results of our simulations are apparently able to predict the value of the Seebeck coefficient, despite the challenge of large thermal fluctuations of this quantity. To the best of our knowledge, this is the first time the Seebeck effect is reproduced by direct simulation of an ionic conductor under non-equilibrium, steady state conditions.

The detailed analysis of simulation trajectories shows that the onset of an electrostatic potential difference under a thermal gradient is accompanied by the formation of a small net charge at each interface, whose sign is such to ensure the overall charge neutrality of the entire sample comprising the two interfaces. Their presence violates a well known theorem valid for interfaces of Coulomb fluids at equilibrium [17] but fully comply with statistical mechanics results and conjectures on systems at steady state conditions [14, 96]. The net charges of opposite sign at the two opposite interfaces are also required to provide an "internal" electric field needed to prevent the flow of charge accompanying the flow of heat, as required by Onsager's reciprocal relations.

The extensive set of simulations for the idealised model shows a wealth of details on the properties of fluids at interfaces, both at equilibrium, and especially at steady state conditions, that have been very seldom investigated by direct non-equilibrium simulations. We find, for instance, that the surface dipole at electrified interfaces grows with increasing temperatures, reflecting the decreased ability of the fluid to screen perturbations, in this

case represented by the solid-like wall. The results also emphasise the role of ion size and (absolute) charge asymmetry between anion and cation in the determination of the interfacial dipole.

The investigation of equilibrium and steady state properties of the idealised ionic fluid model has been complemented by extensive simulations of a molecular ionic fluid meant to reproduce the properties of molten alkali carbonates, which are the system investigated by Prof. S. Kjelstrup using experimental approaches. This relatively simple molecular ionic system represents a step towards the computational investigation of even more complex fluids, consisting of organic ionic compounds that are liquid at ambient conditions. Because of time and computer resource considerations, we limited our exploration of liquid carbonates to equilibrium conditions, but we analysed both homogeneous and inhomogeneous samples. The simulations for the homogeneous systems were carried out to obtain thermodynamic properties, and to estimate linear transport coefficients such as ionic diffusion, electrical and heat conductivities, that are needed to analyse the Seebeck process. Simulations of inhomogeneous samples provided a large amount of information on electrified interfaces described at near-chemical accuracy by empirical force fields. Thus, we computed the number and charge density distribution perpendicular to the solid/fluid interface, the associated dipole and electrostatic potential drop, as well as simple dynamical properties such as the ionic diffusion parallel and perpendicular to the interface.

In summary, my Master Thesis work expands significantly the quantitative information made available by simulation on electrified interfaces at equilibrium and especially steady state non-equilibrium conditions. Nevertheless, it represents only a first preliminary state in the investigation of realistic models of electrified interfaces at non-equilibrium conditions, a subject that certainly has many surprises in store. The first obvious extension of my work will be the investigation of room temperature organic ionic liquids. A second direction for further work is the systematic enhancement of our computational capability, concerning both better implementations of our programs to simulate ionic systems as well as better force field models. A third line of development could concern the development and validation of semi-analytical

models able to predict the Seebeck coefficient for broad classes of homologous materials. The most likely candidates for this role is the square gradient model, already applied in Ref. [97] (see also Ref. [98]) to model transport in fluids at steady state conditions.

Side investigations carried out or started during my project included the *ab-initio* characterisation of molecular systems of interest for my study, and the modelling of image charges at the fluid/metal interface. The development and results of these additional studies are briefly described in this thesis.

Appendix A: Density functional theory

In my project I used density functional theory (DFT) in the Kohn-Sham (KS) formulation [99] to compute the ground state energy and geometry for alkali-carbonate ions and molecules, as well as vibrational frequencies and atomic charges. For this reason, I collect here a few definitions and considerations on the theoretical basis of this approach.

Density functional theory is a fundamental approach to compute the ground state energy of an inhomogeneous many-electron system. It relies on two theorems by Hohenberg and Kohn, and by Kohn and Sham. It provides, in turn, a formal basis for the determination of the potential energy surface of many-electron systems in the adiabatic approximation.

Let us consider N electrons in an external potential $V(\mathbf{r})$, which in most cases will represent the interaction the electrons have with the atomic cores in the system.

The Hohenberg and Kohn theorem [100] concerns the existence and uniqueness of a functional $E[\rho]$ of the electron density $\{\rho(\mathbf{r})\}$, whose minimum value is the ground state energy E_0 of the electron system. The Kohn and Sham theorem [101] has a constructive character, showing how to build such a functional. More precisely, it shows how to make approximations to the exact functional, which is unknown.

The true functional, however, has to contain the kinetic energy $T(N)$ of the electrons, their interaction $U_{ext} = \int V(\mathbf{r})\rho(\mathbf{r})d\mathbf{r}$ with the external field, and the mean field electron-electron interaction (Hartree energy) given by:

$$U_{Hartree} = \frac{1}{2}\int \frac{\rho(\mathbf{r})\rho(\mathbf{r}')}{\mid \mathbf{r} - \mathbf{r}' \mid} d\mathbf{r}d\mathbf{r}' \tag{A.1}$$

More subtle contributions, arising from the Fermi statistics (exchange energy) and from the collective motion of electrons in the ground state (correlation energy) are collected into a further term, named exchange and correlation energy. This term is left unspecified, apart from stating that it is a functional of the electron density.

The external potential and Hartree energies are also obvious and explicit functionals of the density, and the crucial step is now to provide a viable approximation for the kinetic energy. Such approximations have been proposed already in the early stages of quantum mechanics (Thomas and Fermi), but have never been successful, despite several refinements, for instance by Dirac. The crucial contributions by Kohn and Sham has been to introduce auxiliary functions $\{\psi_i(\mathbf{r}), i = 1, ..., N\}$ (Kohn-Sham orbitals), playing the role of single electron orbitals, entering the computation of the electron density according to:

$$\rho(\mathbf{r}) = \sum_{i=1}^{N} \mid \psi(\mathbf{r}) \mid^2 \tag{A.2}$$

The kinetic energy T_s of these orbitals:

$$T_s[\{\psi_i(\mathbf{r})\}] = -\frac{1}{2} \int \left\{ \sum_{i=1}^{N} \psi_i^*(\mathbf{r}) \nabla^2 \psi_i(\mathbf{r}) \right\} d\mathbf{r} \tag{A.3}$$

provides an approximation to the true kinetic energy far better than any previous recipe. Nevertheless, T_s should never be identified with the true kinetic energy, and a (hopefully small) kinetic energy term $T - T_s$ is now included into the exchange-correlation terms.

The Kohn-Sham functional therefore reads:

$$E_{KS}[\rho] = -\frac{1}{2} \int \left\{ \sum_{i=1}^{N} \psi_i^*(\mathbf{r}) \nabla^2 \psi_i(\mathbf{r}) \right\} d\mathbf{r} + \int V(\mathbf{r}) \rho(\mathbf{r}) d\mathbf{r} + \frac{1}{2} \int \frac{\rho(\mathbf{r}) \rho(\mathbf{r}')}{\mid \mathbf{r} - \mathbf{r}' \mid} d\mathbf{r} d\mathbf{r}' + U_{XC}[\rho] \tag{A.4}$$

Only the last term, i.e. U_{XC}, needs to be approximated. To simplify the task, this term is usually expressed as the integral of an exchange-correlation energy per particle ϵ_{XC}:

$$U_{XC} = \int \rho(\mathbf{r}) \epsilon_{XC}[\rho, \mathbf{r}] d\mathbf{r} \tag{A.5}$$

where the XC-energy density $\rho(\mathbf{r})\epsilon[\rho, \mathbf{r}]$ is a functional of the density over the entire system.

Fair approximations for the exchange energy as a function of the density have been known for a long time (Slater), and are exemplified by the simple (and rather inaccurate)

local expression:

$$\epsilon_X[\rho(\mathbf{r})] \propto \rho(\mathbf{r})^{(1/3)} \tag{A.6}$$

leaving the correlation energy $U_C[\rho]$ to be approximated.

At this point, given a suitable approximation for the exchange-correlation energy density, the determination of the ground state energy of the electron system requires the minimisation of the Kohn-Sham functional with respect to the electron density. Since, however, the density itself is written in terms of Kohn-Sham orbitals (see eq. (A.2)), the variational principle is applied to the individual Kohn-Sham orbitals, whose orthogonality and normalisation will be imposed by a set of Lagrange multipliers λ_{ij}. In full analogy with the Hartree-Fock case, the set of $N \times N$ Lagrange multipliers λ_{ij} can be diagonalised into a set of N multipliers, as specified below.

The functional derivative is:

$$\frac{1}{2}\frac{\delta E_{KS}[\rho]}{\delta \psi_i(\mathbf{r})} = -\frac{1}{2}\nabla^2\psi(\mathbf{r}) + \left[V_{ext}(\mathbf{r}) + \int \frac{\rho(\mathbf{r}')}{\mid \mathbf{r} - \mathbf{r}' \mid} d\mathbf{r}' + \frac{\delta U_{XC}[\rho]}{\delta \rho(\mathbf{r})}\right]\psi_i(\mathbf{r}) \tag{A.7}$$

and the minimum conditions are given by the well known set of Kohn-Sham equations:

$$-\frac{1}{2}\nabla^2\psi(\mathbf{r}) + \left[V_{ext}(\mathbf{r}) + \int \frac{\rho(\mathbf{r}')}{\mid \mathbf{r} - \mathbf{r}' \mid} d\mathbf{r}' + \frac{\delta U_{XC}[\rho]}{\delta \rho(\mathbf{r})}\right]\psi_i(\mathbf{r}) = \lambda_i\psi_i(\mathbf{r}) \tag{A.8}$$

where the diagonal Lagrange multipliers have the physical dimensions of an energy, and are known as Kohn-Sham eigenvalues. The operator applied to the orbitals (Kohn-Sham Hamiltonian) depends on the solution (i.e. the ground state density), and therefore these equations need to be solved self-consistently.

The explicit solution of these equations requires the detailed specification of an exhange-correlation approximation, and a practical way to solve the Kohn-Sham equations.

Many approximations for U_{XC} are available [99]. From the simple local density approximation, to gradient corrected functionals and hybrid functionals. Most of our computations relied on the PBE approximation, that represents an accepted standard for this type of computations. Test computations, however, have been done also with other approaches, from

Hartree-Fock to a standard hybrid functional (B3LYP).

The solution of the Kohn-Sham equations requires the expansion of the orbitals on a finite basis, represented by plane waves or by localised atomic-like functions (Gaussian functions, in our case). Once this is done, the set of coupled equations can be expressed in a finite matrix form, and diagonalised by a standard routine such as those available in LAPACK. The basis sets of practical interest, however, are very large (up to many million coefficients). This prevents the full diagonalisation of the KS matrix, not even to say the full solution of the problem involving the iterative part.

An alternative and far more efficient way, still relying on a finite expansion of orbitals on a basis, relies on the explicit inclusion of this expansion into the KS functional. This replacement transforms the functional into a function of the multitude of expansion coefficient. Focusing now on the minimum property of the KS orbitals, we determine the electronic ground state at fixed geometry of the nuclei by direct minimisation of the functional. Several methods are available to carry out the task of minimising a function of many independent variables, and we selected a conjugate gradient method as implemented in the CPMD package.

The state of the art in this type of computational approaches is described in Ref. [102].

Appendix B: Dimensionless variables

Following the standard practice in computations and in theory (as opposed to experiments), in presenting my results I will introduce dimensionless quantities, dividing the quantities that are computed by a natural scale of the same physical dimensions. This will make the results suitable to fit a wide variety of different systems. The conversion to standard units can be carried out afterwards, multiplying each quantity again by a scale of the same dimensionality, this time measured in fixed units.

The following reduced units, denoted by superscript *, will be used in this thesis:

$$T^* = T\frac{k_B}{\epsilon} \tag{B.1}$$

$$\rho^* = \rho\sigma^3 \tag{B.2}$$

$$P^* = P\frac{\sigma^3}{\epsilon} \tag{B.3}$$

$$x^* = x/\sigma \tag{B.4}$$

$$t^* = t\left(\frac{\epsilon}{m\sigma^2}\right)^{1/2} \tag{B.5}$$

$$q^* = \frac{q}{\sqrt{4\pi\epsilon_0\sigma\epsilon}} \tag{B.6}$$

$$E^* = E\sqrt{4\pi\epsilon_0\sigma\epsilon} \tag{B.7}$$

$$D^* = \frac{D}{\sqrt{4\pi\epsilon_0\sigma^3\epsilon}} \tag{B.8}$$

These dimensionless units will be used in Chapter 3, but the superscript * will be dropped. In places where σ is used in equation for the reduced variables, σ_{++} will be used.

Bibliography

[1] L. I. Anatychuk, *Journal of Thermoelectricity* (2), 5 (2004).

[2] G. Pastorino, *J. Thermoelectricity N* **1**, 7 (2009).

[3] P. Ballone, private communication.

[4] S. Kjelstrup, D. Bedeaux, *Non-equilibrium thermodynamics of heterogeneous systems*. World Scientific (2008).

[5] T. Welton, *Chemical reviews* **99**(8), 2071 (1999).

[6] T. J. Abraham, D. R. MacFarlane, J. M. Pringle, *Energy & Environmental Science* **6**(9), 2639 (2013).

[7] S. K. Schnell, et al., *The Journal of Physical Chemistry B* **115**(37), 10911 (2011).

[8] N. M. Eriksen, 'A thermodynamic study of the hydrogen dissociation by the small system method and the reactive force field reaxff', Master's thesis, Norwegian University of Science and Technology, Department of Chemistry (2016).

[9] M. Zebarjadi, K. Esfarjani, M. S. Dresselhaus, Z. F. Ren, G. Chen, *Energy & Environmental Science* **5**(1), 5147 (2012).

[10] M. Takla, O. Burheim, L. Kolbeinsen, S. Kjelstrup, in *Energy Technology 2012: Carbon Dioxide Management and Other Technologies*, pp. 101–108. John Wiley & Sons, Inc. (2012).

[11] A. R. Leach, *Molecular Modelling: Principles and Applications*. Pearson education, 2nd edn. (2001).

[12] J. T. W. M. Tissen, G. J. M. Janssen, *Molecular Physics* **71**(2), 413 (1990).

[13] J.-P. Hansen, I. R. McDonald, *Theory of Simple Liquids*. Elsevier Science (2006).

[14] J. R. Dorfman, T. R. Kirkpatrick, J. V. Sengers, *Annual Review of Physical Chemistry* **45**(1), 213 (1994).

[15] D. Frenkel, B. Smit, *Understanding Molecular Simulation*. Academic Press, Inc., Orlando, FL, USA, 2nd edn. (2001).

[16] M. Bockris, N. Reddy, *Modern Electrochemistry, 2nd ed.* Kluwer Academic (2000).

[17] F. H. Stillinger Jr., R. Lovett, *The Journal of Chemical Physics* **49**(5), 1991 (1968).

[18] G. Gouy, *J. phys* **9**(4), 457 (1910).

[19] D. L. Chapman, *The London, Edinburgh, and Dublin philosophical magazine and journal of science* **25**(148), 475 (1913).

[20] P. Debye, E. Hückel, *Physikalische Zeitschrift* **24**(9), 185 (1923).

[21] D. Henderson, F. F. Abraham, J. A. Barker, *Molecular Physics* **31**(4), 1291 (1976).

[22] G. M. Torrie, J. P. Valleau, *The Journal of Chemical Physics* **73**(11), 5807 (1980).

[23] D. Henderson, D. Boda, *Physical Chemistry Chemical Physics* **11**(20), 3822 (2009).

[24] N. Grønbech-Jensen, O. Farago, *Molecular Physics* **111**(8), 983 (2013).

[25] J.-L. Barrat, F. Chiaruttini, *Molecular Physics* **101**(11), 1605 (2003).

[26] M. T. Børset, et al., *Electrochimica Acta* **182**, 699 (2015).

[27] A. L. Dicks, *Current Opinion in Solid State and Materials Science* **8**(5), 379 (2004).

[28] H. Morita, et al., *Journal of Power Sources* **112**(2), 509 (2002).

[29] A. Ottochian, C. Ricca, F. Labat, C. Adamo, *Journal of Molecular Modeling* **22**(3), 1 (2016).

[30] Y. Ein-Eli, S. R. Thomas, R. Chadha, T. J. Blakley, V. R. Koch, *Journal of The Electrochemical Society* **144**(3), 823 (1997).

[31] R. F. Prien, et al., *Archives of General psychiatry* **41**(11), 1096 (1984).

[32] B. Müller-Oerlinghausen, A. Berghöfer, B. Ahrens, *Canadian journal of psychiatry* **48**, 433 (2003).

[33] M. A. Fuller, *Annals of clinical psychiatry* pp. 23–48 (2011).

[34] A. Zaheer, 'Uses of soda ash', `https://www.scribd.com/doc/75140612/Uses-of-Na2CO3`, Accessed: 2016-06-08.

[35] E. P. Corp., 'About potash', `http://encantopotash.com/english/aboutpotash/default.aspx`, Accessed: 2016-06-08.

[36] P. Raiteri, J. D. Gale, D. Quigley, P. M. Rodger, *The Journal of Physical Chemistry C* **114**(13), 5997 (2010).

[37] G. J. M. Janssen, J. T. W. M. Tissen, *Molecular Simulation* **5**(1-2), 83 (1990).

[38] F. G. Fumi, M. P. Tosi, *Journal of Physics and Chemistry of Solids* **25**(1), 31 (1964).

[39] T. Katō, K. Machida, M. Oobatake, S. Hayashi, *The Journal of chemical physics* **89**(5), 3211 (1988).

[40] T. Yamaguchi, I. Okada, H. Ohtaki, M. Mikami, K. Kawamura, *Molecular Physics* **58**(2), 349 (1986).

[41] T. Koishi, S. Kawase, S. Tamaki, T. Ebisuzaki, *Journal of the Physical Society of Japan* **69**(10), 3291 (2000).

[42] W. L. Jorgensen, J. Tirado-Rives, *Journal of the American Chemical Society* **110**(6), 1657 (1988).

[43] M. C. Wilding, et al., *Scientific reports* **6** (2016).

[44] N. Koura, et al., *Journal of molecular structure* **382**(3), 163 (1996).

[45] S. Kohara, et al., *Journal of Physics: Condensed Matter* **10**(15), 3301 (1998).

[46] ISIS, 'Neutron diffraction', `http://www.isis.stfc.ac.uk/instruments/neutron-diffraction2593.html`, Accessed: 2016-06-08.

[47] J. Habasaki, *Molecular Physics* **69**(1), 115 (1990).

[48] R. A. Jackson, G. D. Price, *Molecular simulation* **9**(2), 175 (1992).

[49] M. Masia, M. Probst, R. Rey, *The Journal of Physical Chemistry B* **108**(6), 2016 (2004).

[50] R. Jorn, R. Kumar, D. P. Abraham, G. A. Voth, *The Journal of Physical Chemistry C* **117**(8), 3747 (2013).

[51] O. Borodin, G. D. Smith, *The Journal of Physical Chemistry B* **113**(6), 1763 (2009).

[52] 'Homogeneous and heterogeneous thermodynamic systems', `http://twt.mpei.ac.ru/TTHB/2/KiSyShe/eng/Chapter5/5-1-Homogeneous-and-heterogeneous-thermodynamic-systems.html`, Accessed: 2016-06-09.

[53] L. Martínez, R. Andrade, E. G. Birgin, J. M. Martínez, *J. Comput. Chem.* **30**(13), 2157 (2009).

[54] J. W. Eastwood, R. W. Hockney, *Journal of Computational Physics* **16**(4), 342 (1974).

[55] E. L. Pollock, J. Glosli, *Computer Physics Communications* **95**(2), 93 (1996).

[56] A. Arnold, C. Holm, *The Journal of chemical physics* **123**(14), 144103 (2005).

[57] A. Arnold, C. Holm, *Computer Physics Communications* **148**(3), 327 (2002).

[58] A. Arnold, J. de Joannis, C. Holm, *The Journal of chemical physics* **117**(6), 2496 (2002).

[59] 'Jmol: an open-source java viewer for chemical structures in 3D.', http://www.jmol.org/.

[60] J. C. Shelley, G. N. Patey, D. R. Bérard, G. M. Torrie, *The Journal of chemical physics* **107**(6), 2122 (1997).

[61] F. Iori, S. Corni, *Journal of Computational Chemistry* **29**(10), 1656 (2008).

[62] M. S. Daw, M. I. Baskes, *Physical review letters* **50**(17), 1285 (1983).

[63] M. I. Baskes, *Physical review letters* **59**(23), 2666 (1987).

[64] J. P. Perdew, K. Burke, M. Ernzerhof, *Physical review letters* **77**(18), 3865 (1996).

[65] 'CPMD', http://www.cpmd.org/, Copyright IBM Corp 1990-2015, Copyright MPI für Festkörperforschung Stuttgart 1997-2001.

[66] M. J. Frisch, et al., 'Gaussian∼09 Revision E.01', Gaussian Inc. Wallingford CT 2009.

[67] U. C. Singh, P. A. Kollman, *Journal of Computational Chemistry* **5**(2), 129 (1984).

[68] J.-P. Ryckaert, G. Ciccotti, H. J. C. Berendsen, *Journal of Computational Physics* **23**(3), 327 (1977).

[69] F. Ramondo, L. Bencivenni, *Journal of Molecular Structure* **221**, 169 (1990).

[70] S. Plimpton, *Journal of computational physics* **117**(1), 1 (1995. http://lammps.sandia.gov).

[71] W. Shinoda, M. Shiga, M. Mikami, *Physical Review B* **69**(13), 134103 (2004).

[72] G. J. Martyna, D. J. Tobias, M. L. Klein, *The Journal of Chemical Physics* **101**(5), 4177 (1994).

[73] M. Parrinello, A. Rahman, *Journal of Applied physics* **52**(12), 7182 (1981).

[74] M. E. Tuckerman, J. Alejandre, R. López-Rendón, A. L. Jochim, G. J. Martyna, *Journal of Physics A: Mathematical and General* **39**(19), 5629 (2006).

[75] M. Tuckerman, *Statistical mechanics: theory and molecular simulation*. Oxford University Press (2010).

[76] G. J. Janz, N. P. Bansal, *Journal of Physical and Chemical Reference Data* **11**(3), 505 (1982).

[77] J. Daintith, *Dictionary of Chemistry (6th Edition)*. Oxford University Press (2008).

[78] T. Ikeshoji, B. Hafskjold, *Molecular Physics* **81**(2), 251 (1994).

[79] G. J. Janz, M. R. Lorenz, *Journal of The Electrochemical Society* **108**(11), 1052 (1961).

[80] N. C. for Biotechnology Information, 'Pubchem compound database, CID=11125', `https://pubchem.ncbi.nlm.nih.gov/compound/11125`, Accessed: 2016-06-09.

[81] Guidechem, 'Lithium carbonate', `http://www.guidechem.com/dictionary/en/554-13-2.html`, Accessed: 2016-06-09.

[82] N. C. for Biotechnology Information, 'Pubchem compound database, CID=10340', `https://pubchem.ncbi.nlm.nih.gov/compound/10340`, Accessed: 2016-06-09.

[83] C. Book, 'Sodium carbonate', `http://www.chemicalbook.com/ProductMSDSDetailCB9853672_EN.htm`, Accessed: 2016-06-09.

[84] N. C. for Biotechnology Information, 'Pubchem compound database, cid=11430', `https://pubchem.ncbi.nlm.nih.gov/compound/11430`, Accessed: 2016-06-09.

[85] H. Ohata, K. Takeuchi, K. Ui, N. Koura, *ECS Transactions* **6**(14), 57 (2007).

[86] V. M. B. Nunes, M. J. V. Lourenço, F. J. V. Santos, C. A. N. de Castro, *Journal of Chemical & Engineering Data* **48**(3), 446 (2003).

[87] K. A. Gillis, et al., *Experimental Thermodynamics: Advances in Transport Properties of Fluids*, vol. 9. Royal society of Chemistry (2014).

[88] P. L. Spedding, R. Mills, *Journal of The Electrochemical Society* **112**(6), 594 (1965).

[89] X. Zhang, M. Fujii, *International Journal of Thermophysics* **21**(1), 71 (2000).

[90] J. A. Armstrong, P. Ballone, *The Journal of Physical Chemistry B* **115**(17), 4927 (2011).

[91] J. Trullas, J. A. Padró, *Physical Review B* **55**(18), 12210 (1997).

[92] Ç. Tasseven, J. Trullas, O. Alcaraz, M. Silbert, A. Giró, *The Journal of chemical physics* **106**(17), 7286 (1997).

[93] T. Yamaguchi, A. Nagao, T. Matsuoka, S. Koda, *The Journal of chemical physics* **119**(21), 11306 (2003).

[94] D. Pines, P. Nozieres, *Theory of Quantum Liquids: Normal Fermi liquids, Advanced Book Classics*. Addison-Wesley Publishing Company, Advanced Book Program (1989).

[95] M. S. Daw, M. I. Baskes, *Phys. Rev. B* **29**, 6443 (1984).

[96] L. Bertini, A. De Sole, D. Gabrielli, G. Jona-Lasinio, C. Landim, *arXiv preprint arXiv:0705.2996* (2007).

[97] E. Magnanelli, Ø. Wilhelmsen, D. Bedeaux, S. Kjelstrup, *Physical Review E* **90**(3), 032402 (2014).

[98] A. Albano, D. Bedeaux, *Physica A: Statistical Mechanics and its Applications* **147**(1), 407 (1987).

[99] R. M. Martin, *Electronic Structure, Basic Theory and Practical Methods*. Cambridge University Press, 2004.

[100] P. Hohenberg, W. Kohn, *Physical review* **136**(3B), B864 (1964).

[101] W. Kohn, L. J. Sham, *Physical review* **140**(4A), A1133 (1965).

[102] D. Marx, J. Hutter, in J. Grotendorst (ed.), *Modern Methods and Algorithms of Quantum Chemistry*, vol. 3 of *NIC Series*, pp. 301–449. John von Neumann Institute for Computing, Jülich, NIC-Directors (2000).